Wide Field X-ray Spectral Imaging Using Bent Laue Monochromators

A Dissertation Submitted to the
College of Graduate and Postdoctoral Studies
in Partial Fulfillment of the Requirements
for the Degree of Doctor of Philosophy
in the Division of Biomedical Engineering
University of Saskatchewan
Saskatoon

By
Peng Qi

Permission to Use

In presenting this dissertation in partial fulfillment of the requirements for a Postgraduate degree from the University of Saskatchewan, I agree that the Libraries of this University may make it freely available for inspection. I further agree that permission for copying of this dissertation in any manner, in whole or in part, for scholarly purposes may be granted by the professor or professors who supervised my dissertation work or, in their absence, by the Head of the Department or the Dean of the College in which my dissertation work was done. It is understood that any copying or publication or use of this dissertation or parts thereof for financial gain shall not be allowed without my written permission. It is also understood that due recognition shall be given to me and to the University of Saskatchewan in any scholarly use which may be made of any material in my dissertation.

Disclaimer

Reference in this dissertation to any specific commercial products, process, or service by trade name, trademark, manufacturer, or otherwise, does not constitute or imply its endorsement, recommendation, or favoring by the University of Saskatchewan. The views and opinions of the author expressed herein do not state or reflect those of the University of Saskatchewan, and shall not be used for advertising or product endorsement purposes.

Requests for permission to copy or to make other uses of materials in this dissertation in whole or part should be addressed to:

Head of the Division of Biomedical Engineering
2B60 Engineering Building, 57 Campus Drive
University of Saskatchewan
Saskatoon, Saskatchewan S7N 5A9 Canada

OR

Dean
College of Graduate and Postdoctoral Studies
University of Saskatchewan
116 Thorvaldson Building, 110 Science Place
Saskatoon, Saskatchewan S7N 5C9 Canada

Abstract

X-ray Absorption Spectroscopy (XAS) is a widely used method for determining the local environment and/or speciation of elements. Conventionally, synchrotron based XAS requires mechanically scanning through the desired energy range using a flat double-crystal monochromator. Energy Dispersive XAS (EDXAS) is a variant of the XAS technique, which typically uses a bent crystal monochromator to provide a focused x-ray beam that contains all the energies required to make an XAS measurement. An obvious advantage of EDXAS over conventional XAS is the high efficiency and stability, because mechanical energy scanning is not needed. With a high brilliance x-ray source and high speed detection system, EDXAS enables XAS studies associated with extreme conditions, femtosecond time resolution and atomic level precision.

The thesis describes the development of a Wide Field EDXAS imaging system, employing a specially designed bent Laue crystal monochromator that matches the so-called 'magic condition' which was previously described for spectral K-edge subtraction imaging. Compared to a classic EDXAS system, the Wide Field EDXAS system has the following advantages. (i) The diffracted beam from a bend magnet synchrotron source is focused in the vertical dimension and unaltered in the horizontal dimension. This focused line beam takes advantage of the width of a bend magnet x-ray beam and records spatial information across the beam. Combining the information from the energy dispersion dimension and the spatial dimension, the Wide Field EDXAS system can acquire several thousand spectra per exposure. (ii) A bent crystal that matches the 'magic condition' provides a good energy resolution in addition to the optimized focal size. The improved energy resolution enables the system to investigate the fine structure of x-ray absorption spectra with good spatial resolution using a single x-ray optic.

To make the use of the Wide Field EDXAS system more accessible, user-friendly software has been developed to process and extract concentration information from images acquired in either projection (2D) or computed tomography (3D) mode of operation. This software is made available at the Canadian Light Source BMIT-BM beamline and is compatible with another contrast element imaging method - spectral K-edge subtraction imaging.

The energy resolution of a bent crystal at the 'magic condition' is still not as good as that of a flat double-crystal monochromator. To pursue the ultimate energy resolution of a bent Laue crystal, a new approach has been developed for describing the general behavior of bent Laue crystals from a ray-tracing point of view. The so-called quasi-mono beam approach provides an intuitive view of bent crystal diffraction and leads to deeper insights. It explains the energy and spatial properties of common and special cases of bent Laue optics, predicts phenomena that can improve energy dispersion related x-ray imaging techniques and provides a theory framework that makes ray-tracing simulation easier to realize.

Acknowledgements

First and foremost, I would like to express my deepest gratitude to my supervisor, Professor Dean Chapman. His vast knowledge, patient guidance and generous encouragement helped me immensely during my PhD. His curiosity about the world and his passion for scientific research have always inspired me. In this sense, he is not only my mentor, but also the best companion in the game of exploring nature's puzzles.

I would also like to extend my gratitude to my co-supervisors, Professor Ingrid Pickering and Professor Graham George, for their great support and help on all fronts. Special thanks to them for proposing and facilitating my transition from Master's to PhD. The positive impact this has had on me is immeasurable.

I am also very grateful to Dr. Chithra Karunakaran for her recognition and support of my skills and the collaborative opportunities she has brought to me. Thanks should also go to Professor Joyce McBeth, Professor Daniel Chen and Professor Derek Peak who, as my thesis committee members, have been very understanding and supportive of me.

Great thanks to my colleagues and co-workers for their assistance and suggestions. Nazanin Samadi, in particular, helped me the most with experiments and shared with valuable experiences and knowledge, as did Xianbo Shi, Bassey Bassey, Mercedes Martinson, Olena Ponomarenko and many others.

I wish to thank George Belev, Adam Webb, Arash Panahifar at the BMIT-BM beamline for their help in preparing and assisting with the beamline experiments. Thanks should also go to Ning Zhu and Ning Chen for their advice and help.

I would like to acknowledge the financial support of Canadian Institutes of Health Research Training grant in Health Research Using Synchrotron Techniques (CIHR-THRUST), Natural Sciences and Engineering Research Council of Canada (NSERC) and Canada Research Chair program (CRC). Research described in this dissertation was performed at the Canadian Light Source, which is funded by the Canada Foundation for Innovation, NSERC, the National Research Council Canada, the CIHR, the Government of Saskatchewan, Western Economic Diversification Canada, and the University of Saskatchewan.

The people I cannot thank enough are my parents. Their unconditional support and trust in me is my greatest strength. The completion of my PhD would not have been possible without their encouragement and nurturing.

Dedication

To my beloved father and mother for landing me down on the Earth.

To my beloved Xiaoyi for making my time on the Earth tolerable.

Table of Contents

PERMISSION TO USE i

ABSTRACT ii

ACKNOWLEDGEMENTS iii

DEDICATION iv

TABLE OF CONTENTS v

LIST OF TABLES x

LIST OF FIGURES xi

LIST OF ABBREVIATIONS xiii

LIST OF SYMBOLS xiv

CHAPTER 1
INTRODUCTION 1

1.1 Introduction . . . 1
1.1.1 X-ray absorption spectroscopy . . . 1
1.1.2 Energy dispersive x-ray absorption spectroscopy . . . 1
1.2 History and Present . . . 2
1.3 Principles . . . 3
1.3.1 Bragg's law . . . 3
1.3.2 Bragg diffraction and Laue diffraction . . . 4
1.4 The EDXAS System . . . 5
1.4.1 X-ray source . . . 6
1.4.2 Bent crystal spectrometer . . . 7
1.4.3 Detection . . . 14
1.4.4 Mirrors . . . 15
1.5 Applications . . . 15
1.5.1 Time resolved applications . . . 15
1.5.2 Differential EXAFS . . . 16
1.5.3 2D/3D XAS mapping . . . 16

1.5.4 Extreme conditions . . . 16
1.6 Discussion . . . 16
1.7 Project Objectives and Thesis Outline . . . 17
1.7.1 Project motivation . . . 17
1.7.2 Project objectives . . . 17
1.7.3 Thesis outline . . . 18

CHAPTER 2
FOCUSING AND ENERGY DISPERSION PROPERTIES OF A CYLINDRICALLY BENT ASYMMETRIC LAUE CRYSTAL **20**

2.1 Introduction . . . 22
2.2 Conceptual View of the Magic Condition . . . 24
2.3 Mathematical View of the Magic Condition . . . 25
2.3.1 Thickness of a deformed crystal . . . 25
2.3.2 The change in the angle between the diffraction plane and the surface normal, $\Delta\chi$ . . . 27
2.3.3 The change in the angle between the x-ray diffraction direction and the crystal surface normal, $\Delta\phi$ . . . 27
2.3.4 Calculation for the condition: $\Delta\chi_T + \Delta\phi_T = 0$ . . . 29
2.4 Energy Spread of the Single Exit Ray . . . 29
2.5 Conclusions . . . 30

CHAPTER 3
X-RAY SPECTRAL IMAGING PROGRAM: XSIP **31**

3.1 Introduction . . . 33
3.2 Theory . . . 34
3.3 Program Workflow . . . 35
3.3.1 System settings and data loading . . . 35
3.3.2 Preprocessing . . . 35
3.3.3 X-ray absorption near edge curve fitting . . . 38
3.4 Features . . . 39
3.4.1 Main task . . . 39
3.4.2 Result storage . . . 40
3.4.3 Utilities . . . 40
3.4.4 A graphic user interface . . . 41
3.5 Summary . . . 42

CHAPTER 4

WIDE FIELD IMAGING ENERGY DISPERSIVE X-RAY ABSORPTION SPECTROSCOPY **43**

4.1 Introduction . . . 44
4.2 Results . . . 47
4.2.1 Feasibility test . . . 47
4.2.2 Concentration sensitivity test . . . 50
4.2.3 Energy resolution . . . 51
4.3 Discussion . . . 52
4.4 Methods . . . 54
4.4.1 Imaging system . . . 54
4.4.2 Bent Laue energy dispersion geometry (magic condition) . . . 55
4.4.3 Analysis method . . . 60
4.4.4 Sample preparation . . . 61
4.4.5 Data collection . . . 61

CHAPTER 5

NEW INSIGHTS INTO THE FOCUSING AND ENERGY DISPERSION PROPERTIES OF BENT LAUE CRYSTALS **64**

5.1 Introduction . . . 66
5.2 Background . . . 67
5.3 Magic Condition . . . 68
5.3.1 Concept . . . 68
5.3.2 Magic condition with infinite source distance . . . 68
5.3.3 Magic condition with finite source distance . . . 69
5.3.4 Equivalency to the other magic condition apporach . . . 71
5.4 Energy Resolution of a Magic Condition Monochromator . . . 71
5.4.1 Contributions to the energy resolution . . . 72
5.4.2 Integration of all contributions . . . 72
5.4.3 The ultimate energy resolution magic condition . . . 73
5.5 Quasi-Monochromatic Beam for Off-Magic Condition . . . 74
5.5.1 Concept . . . 74
5.5.2 Focal size . . . 76
5.5.3 Energy spread . . . 77
5.5.4 Optimal detector distance . . . 78
5.5.5 Monochromatic focus . . . 80

5.6 Discussion 81

CHAPTER 6

CONCLUSION AND FUTURE WORK **83**

6.1 Conclusion 83

6.2 Future Work 84

6.2.1 Future upgrades 84

6.2.2 Future applications 84

6.2.3 Experimental proof of the predicted monochromatic focus 85

REFERENCES **86**

APPENDIX A

WIDE FIELD EDXAS IMAGING EXPERIMENT PROCEDURES **94**

A.1 Beamline 94

A.2 Stages 94

A.3 Monochromator 95

A.4 Contrast Agent 97

A.5 Find the K-edge 97

A.6 Sample 98

A.7 Data Collection 99

APPENDIX B

MAGIC CONDITION RELATED CALCULATIONS **102**

B.1 $\Delta\chi$ and $\Delta\phi$ 102

B.1.1 $\Delta\chi$ 102

B.1.2 $\Delta\phi$ 103

B.2 Feature Angles in General Bent Laue Diffraction with Finite Source Distance 104

B.2.1 ψ 105

B.2.2 Θ 105

B.2.3 $\Delta\phi$ 106

B.2.4 $\Delta\theta_{B_{01}}$ 106

B.3 Integration of Energy Resolution Contributions from $\frac{\Delta E}{E}_1$ and $\frac{\Delta E}{E}_2$ 106

B.4 Focal Size Calculation with Two Types of Foci 107

B.5 Directional Energy Spread in the Quasi-Monochromatic Beam 107

B.5.1 $\Delta\theta_{Q1}$ 107

B.5.2 $\Delta\theta_{Q2}$ 107

B.6 Calculation for the Optimal Detector Distance 108

B.7 Precise Calculations for Feature Angles at Feature Locations on the Crystal 109
B.7.1 χ_1 and χ_2 109
B.7.2 θ_{B1} 109
B.7.3 θ_{B2} 109
B.8 Summary of Variables in Chapter 5 109
B.8.1 Source distance, p 110
B.8.2 Crystal bending radius, R 110
B.8.3 Crystal thickness, T_0 and T 110
B.8.4 Bragg angle, θ_B 110
B.8.5 Asymmetry angle, χ 110
B.8.6 Poisson ratio, ν 110
B.8.7 $\Delta\chi$ 111
B.8.8 $\Delta\phi$ and $\Delta\phi_\infty$ 111
B.8.9 Quasi-Monochromatic Beam Width (QMBW), W 111
B.8.10 Quasi-monochromatic beam footprint length, L 111

List of Tables

1.1 Existing or planned EDXAS beamlines worldwide 3

B.1 Real focus or virtual focus 110

List of Figures

1.1 Bragg diffraction . . . 3
1.2 Optics of Bragg type and Laue type diffraction . . . 4
1.3 Reflectivity profile of 0.3 mm thick Si(111) Laue crystal at 12 keV. . . . 5
1.4 Energy dispersive XAS system in Bragg geometry . . . 5
1.5 Bragg type EDXAS system layout . . . 8
1.6 Laue type EDXAS system layout . . . 9
1.7 Reflectivity profiles of bent crystals . . . 10
1.8 Elliptically bent Bragg type EDXAS system layout . . . 13

2.1 Crystal plate diffraction geometries . . . 23
2.2 Bent asymmetric Laue focusing . . . 24
2.3 Energy dispersion of a bent Laue crystal at the 'magic condition' . . . 25
2.4 Schematic to estimate the change in bent crystal thickness and asymmetric angle χ . . . 26
2.5 Schematic to estimate the change in ϕ. . . . 28

3.1 An example Edge image . . . 36
3.2 The geometry for relating the diffraction angles and the pixel positions on the detector . . . 37
3.3 An example of spectra curve fitting . . . 38
3.4 Density distributions of reference materials in sinograms and CT reconstruction images . . . 39
3.5 Screenshots of the XSIP GUI . . . 41

4.1 Schematic of the bent Laue energy dispersive system for speciation imaging application . . . 46
4.2 Single projection by wide-field EDXAS imaging . . . 47
4.3 Spectrum comparison for experiment data and traditional XAS measurements . . . 48
4.4 CT reconstruction of Se compound solutions . . . 49
4.5 Measured concentrations and prepared concentrations of Se species . . . 50
4.6 CT concentration sensitivity for selenate, selenite and selenomethionine . . . 51
4.7 Measured and ray-tracing simulated peak at the detector from a 10 µm diameter pinhole . . . 52
4.8 Bent Laue monochromator . . . 56
4.9 Bent Laue geometry crystal that meets the 'magic condition' has overlapped geometrical focus (f_g) and polychromatic focus (f_p) . . . 57
4.10 Ray tracing results for a 10 µm pinhole in front of the crystal showing the energy resolution and the vertical size (sizes are shown in cm) . . . 59

4.11 The energy vs vertical beam location dependence and the energy resolution at each detector pixel . . . 60
4.12 Samples and sample holders . . . 62

5.1 Bent asymmetric Laue focusing . . . 67
5.2 Magic condition exterior concept view . . . 68
5.3 Magic condition interior concept view . . . 69
5.4 Magic condition with finite source distance . . . 70
5.5 Energy resolution of a magic condition monochromator in a range of focal distance . . . 73
5.6 Geometry for quasi-mono beam width calculation . . . 75
5.7 Focal size calculation . . . 77
5.8 Quasi-mono beam geometry . . . 78
5.9 Detector distance . . . 80

A.1 System setup overview . . . 94
A.2 Contrast agent stage . . . 95
A.3 Sample stage . . . 95
A.4 Detector stage . . . 96
A.5 The WF-EDXAS monochromator . . . 96
A.6 Water cooling machine. . . . 97
A.7 Se film on the contrast agent stage. . . . 97
A.8 Image of the beam at Se K-edge going through a Se film. . . . 98
A.9 Use a pin on the sample stage to locate the focus of the beam . . . 99
A.10 Sample stage control programs . . . 100
A.11 CT scan motion setup . . . 100
A.12 CT scan data collection setup . . . 101

B.1 $\Delta\chi$ . . . 102
B.2 $\Delta\phi$ . . . 103
B.3 Feature angles in general bent Laue diffraction . . . 105
B.4 Focal size in relation to the single-ray focus and the geometric focus geometry . . . 107

List of Abbreviations

BM	Bend Magnet
BMIT	Biomedical Imaging and Therapy Facility
CCD	Charge Coupled Device
CLS	Canadian Light Source
CT	Computed Tomography
EDXAS	Energy Dispersive X-ray Absorption Spectroscopy
ESRF	European Synchrotron Radiation Facility
EXAFS	Extended X-ray Absorption Fine Structure
FWHM	Full Width Half Maximum
GUI	Graphic User Interface
IDL	Interactive Data Language
KES	K-Edge Subtraction
KB mirror	Kirkpatrick-Baez mirror
LURE	Laboratoire pour l'Utilisation du Rayonnement Electromagnétique
PDA	Photodiode Array
PF-AR	Photon Factory Advanced Ring
QMBW	Quasi-Monochromatic Beam Width
SeMet	Selenomethionine
sKES	spectral K-Edge Subtraction
XAS	X-ray Absorption Spectroscopy
XAFS	X-ray Absorption Fine Structure
XANES	X-ray Absorption Near Edge Structure
XSIP	X-ray Spectral Imaging Program

List of Symbols

A, B, C, D	Critical locations on a bent Laue crystal 5.8
$\overrightarrow{AA'}$	Diffracted reference ray
$\overrightarrow{CC'}$	The farthest parallel x-ray to the diffracted reference x-ray
c	The speed of light in vacuum
D	Source to crystal distance
d	Distance from the geometric focus to the monochromatic focus
d_∞	Distance from the geometric focus to the monochromatic focus when the source distance is infinite
d_∞^{sym}	Distance from the geometric focus to the monochromatic focus when the source distance is infinite and the crystal Bragg planes are symmetric
d, d_{hkl}	Crystal lattice spacing of Bragg planes
d_{fd}	Distance from the crystal focus to the detector
d_0	Lattice spacing of a flat crystal
d'	Lattice spacing on the compression side of the crystal
E	Photon energy
e	Euler's number or the base of the natural logarithm
f_1, f_s	Source to crystal distance
f_{2g}, f_g	Crystal to geometric focus distance
f_{2s}, f_p	Crystal to single-ray focus distance
h	Planck's constant
h	Crystal unit cell height
h_0	Crystal unit cell height at the neutral plane
h, k, l	Miller indices
N	Number of photons
$\hat{n}$	Crystal surface normal
L	The length of the crystal that is irradiated by the incident beam
L	The length of the footprint of the quasi-monochromatic beam
L_∞	The length of the footprint of the quasi-monochromatic beam when the source distance is infinite
L_∞^{sym}	The length of the footprint of the quasi-monochromatic beam when the source distance is infinite and the crystal Bragg planes are symmetric
p	Source to crystal distance
q	Crystal to focus distance

q_E	Crystal to monochromatic focus distance
$q_{E\infty}^{\text{sym}}$	Crystal to monochromatic focus distance when the source distance is infinite and the crystal Bragg planes are symmetric
q_G	Crystal to geometric focus distance
q_{G0}	Geometric focal distance corresponding to the upstream surface of the crystal
q_{G1}	Geometric focal distance corresponding to the downstream surface of the crystal
$q_{G\infty}$	Geometric focal distance when source distance is infinite
q_S	Crystal to single-ray focus distance
R	Crystal bending radius
S	Size of the source transverse to the central ray in the diffraction plane
S_f	Size of the focus transverse to the central x-ray
T	Crystal thickness
T_0	Crystal thickness in absence of bending
T_{bent}	Bent crystal thickness
t	Projected thickness of a material
t	Crystal unit cell thickness
t_0	Crystal unit cell thickness at the neutral plane
W	Quasi-monochromatic beam width
W_∞	Quasi-monochromatic beam width when the source distance is infinite
W_∞^{sym}	Quasi-monochromatic beam width when the source distance is infinite and the crystal Bragg planes are symmetric
w_D	Darwin width
ΔE	Energy resolution
$\Delta E/E$	Relative energy resolution
$\Delta E/E$	Relative bandwidth
$\Delta\theta_{B_{01}}$	Change of θ_B angle from point A to B
$\Delta\theta_Q$	The total energy spread in the quasi-monochromatic beam
$\Delta\theta_Q$	The energy spread in the quasi-monochromatic beam caused by the lattice spacing variation across the crystal
$\Delta\theta_Q$	The total energy spread in the quasi-monochromatic beam caused by the finite source distance
$\Delta\phi$	Change of ϕ angle from point A to B
$\Delta\phi$	Change of ϕ angle from point A to B when the source distance is infinite
$\Delta\chi$	Change of χ angle from point A to B

Θ	Deviation angle of x-rays exit at point B
θ, θ_B	Bragg angle
θ'_B	Effective Bragg angle where the diffracted reference x-ray exits the crystal
$\theta_{B_{\text{mis}}}$	Bragg angle misalignment from the magic condition
θ_K	Bragg diffraction angle of the x-rays at the K-edge energy
λ	Wavelength
μ/ρ	Mass attenuation coefficient
ν	Poisson's ratio
ρ	Crystal bending radius
ρ	Mass density
τ	Thickness of a bent crystal
τ_+	Thickness of a bent crystal from the neutral plane to the concave surface of the crystal
τ_-	Thickness of a bent crystal from the neutral plane to the convex surface of the crystal
ϕ, ϕ_0	Directional angle from the x-ray incident direction to the crystal surface normal at the location where the reference x-ray enters the crystal
ϕ_1	Directional angle from the x-ray incident direction to the crystal surface normal at the location where the reference x-ray exits the crystal
χ, χ_0	Asymmetry angle or the directional angle from the diffraction lattice to the surface normal at the location where the reference x-ray enters the crystal.
χ_1	Asymmetry angle or the directional angle from the diffraction lattice to the surface normal at the location where the reference x-ray exits the crystal.
χ'	Asymmetry angle on the compressed side of a bent crystal
ψ	Angle formed by x-rays from a point source
ω	Angle formed between the crystal surface normals at the locations where the reference x-ray enters and exits the crystal

Chapter 1

Introduction

1.1 Introduction

1.1.1 X-ray absorption spectroscopy

X-ray Absorption Spectroscopy (XAS) is one of the methods used for speciation and imaging of trace elements in biological samples [1]. It involves the collection of absorption spectra at energies near and above the absorption edge (e.g., K-edge) of an element [2]. XAS is often divided into two distinct regions: X-ray Absorption Near Edge Structure (XANES)-region from 50 eV below to 50 eV above the absorption edge and Extended X-ray Absorption Fine Structure (EXAFS)-region from 50 to approximately 1,000 eV above the absorption edge [1, 2]. Conventional x-ray and synchrotron radiation sources have been used for XAS; the advantages of using synchrotron sources over conventional x-ray sources include availability of high x-ray flux and brightness (intensity), continuous spectrum, small beam divergence, and collection of absorption spectra within few minutes.

The classical method of performing XAS, which is still mostly used, is to mechanically scan through the required energy range using flat double-crystal monochromators. It is a very important research tool with more than 10,000 publications in the primary peer reviewed scientific literature employing XAS in the past 10 years. The prevalence of using fluorescence for increased sensitivity to lower concentrations requires an energy scanning method so that the excitation energy and fluorescence can be correlated.

1.1.2 Energy dispersive x-ray absorption spectroscopy

In Energy Dispersive XAS (EDXAS), a bent crystal monochromator is typically used to provide a focused x-ray beam that contains all the energies required to make an XAS measurement. Bent crystal monochromators in either the Bragg (reflection) or Laue (transmission) geometry have been developed for EDXAS with the former being the first type to be developed, and the more frequently used [3, 4, 5]. The Laue geometry may require a thin crystal to avoid significant photon loss through the crystal depending on the x-ray energy chosen. High stability during measurements allowing atomic level precision, acquisition of the spectral data in a very short time, and the simultaneous collection of the whole x-ray absorption spectrum are the reported advantages of EDXAS compared to the traditional method [6]. With the use of a high brilliance x-ray

source and high speed detection systems, XAS studies associated with extreme conditions, femtosecond time resolution and high efficiency become possible or more practical.

However, unlike transmission XAS, the rapid measurement allowed by EDXAS in the transmission mode cannot be coupled with the high sensitivity fluorescence approach. This is because all of the excitation x-ray energies are present and cannot be directly correlated with fluorescence energies. Hence, EDXAS is used for higher concentration applications, rapid data acquisition and/or screening of samples.

1.2 History and Present

Since Cauchois [7] and co-workers pioneered the idea of using dispersive optics to collect x-ray absorption spectra, not much work had been done until transmission type flat crystals were applied at laboratory x-ray sources at the beginning of 1980's [8, 9].

The bent crystal dispersive spectrometer design applied on a synchrotron x-ray source was initiated by Matsushita [10]. It was a more practical design than using a flat crystal with a synchrotron source because of the much larger source distance allowed by the highly collimated nature of the synchrotron light distribution. This original design included a cylindrically bent Bragg type crystal with the diffraction planes parallel to the crystal surface and an x-ray film as a position sensitive detector. An energy range of about 1 keV was covered, which contained the Ni and Cu K-edge energies. An energy resolution of 2.01 eV was estimated. The horizontal (focusing plane) width of the focus was measured to be 0.6 mm. Required exposure time ranged from 0.1 to 15 seconds depending on the storage ring current and the sample (Cu foil or Ni foil).

After that, synchrotron based EDXAS systems were further studied and developed at many facilities for its potential application to many scientific research fields [3, 11, 12, 13, 14, 15, 16]. Tolentino 1989, 1990 (LURE) [17, 18] presented an elliptical curved spectrometer which realized an aberration-free focus overcoming an intrinsic shortfall of cylindrically curved spectrometer optics. Hagelstein 1995 (ESRF) [19] reported the design of the first Laue type EDXAS spectrometer, which covered applications at higher x-ray energies (i.e., 10 – 28 keV), where crystal absorption and crystal length is less of an issue than the Bragg geometry. This spectrometer also introduced the asymmetry angle to the design of the bent Laue type crystal for wider reflection energy band.

As an example of a modern EDXAS beamline, the ID24 at ESRF has both Bragg type and Laue type spectrometers using an undulator source in operation at separate branches of the beamline in complementary energy ranges. For a Si(111) Bragg spectrometer at 7 keV , the focal spot size is 4 µm by 4 µm FWHM, the full spectral range is roughly 800 eV, $\delta E/E$ is 1.2×10^{-4}, and the flux on sample is 1×10^{14} photons/s . The most advanced XSTRIP detector [20, 21] features a readout time of 2.8 µs and is pushing the time resolution of EDXAS system to MHz level.

Nowadays, EDXAS beamlines are in operation or construction at synchrotron facilities all over the world. A brief overview of the reported beamlines is listed in Table 1.1 [22].

Table 1.1: Existing or planned EDXAS beamlines worldwide [22].

Beamline	Synchrotron	Source	Energy (keV)	PLC.	H. Spot size (µm)	Min. Exposure time/rep rate	Ref.	Status
D06A	LNLS-Brasil	BM	4-14	B	250	1/120 ms	[23]	Oper.
D-line	SSRF-CHINA	U	5-20	B-L				Construct.
BL08	Indus II-India	BM	4-24	B	200	10/300 ms	[24]	Oper.
ID24	ESRF-France	U	5-28	B-L	3-20	0.15 µs/2.8 µs	[21]	Oper.
ODE	SOLEIL-France	BM	3.5-25	B	25	10 µs/50 µs	[4]	Oper.
NW2A	PF-AR-Japan	U	5-40	B-L	500	0.5 µs/23 µs	[25]	Oper.
BL14B1	Spring8-Japan	BM	7-40	B-L	90-160	6 ms	[26]	Oper.
BL28B2	Spring8-Japan	BM	8-80	B-L	100	6 ms	[27]	Oper.
BL2.2	SLRI-Thailand	BM	2.4-8	B	1000	1 ms/25 ms	[28]	Oper.
I20	DLS-UK	W	6-26	B	50	0.5 µs/10 µs	[29]	Comm.

Notes: BM: bending magnet, U: undulator, W: wiggler. PLC: polychromator, B: Bragg geometry, L: Laue geometry.

1.3 Principles

1.3.1 Bragg's law

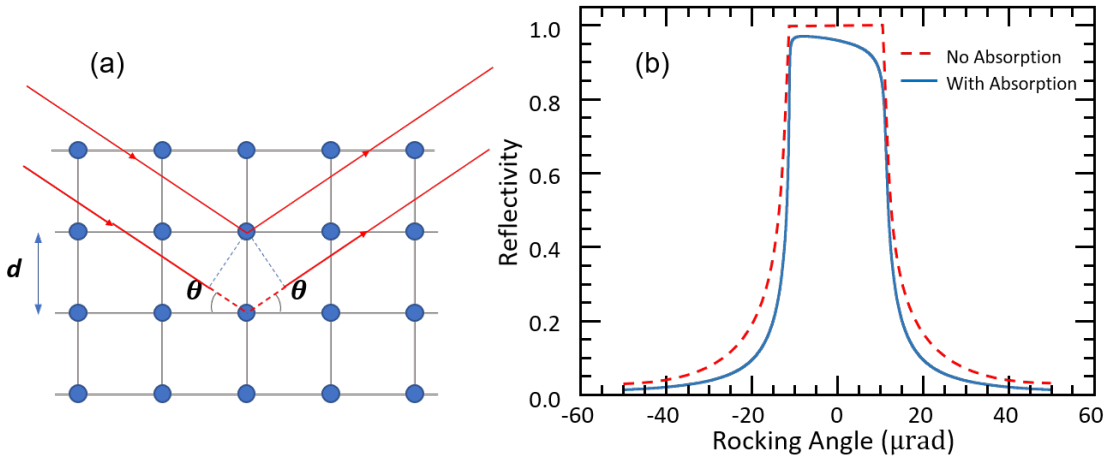

Figure 1.1: Bragg diffraction. (a) X-ray diffraction at Bragg angle. (b) Reflectivity curve of a Bragg type Si(111) crystal at 12 keV with and without considering the absorption of the crystal.

According to Bragg's law,

$$n\lambda = 2d\sin\theta, \tag{1.1}$$

the reflected x-rays with the wavelength $n\lambda = 2d\sin\theta$ get the maximum constructive interference, where d is the interplanar distance in the crystal, θ is the angle between the incident x-ray and the reflection planes,

which is called the Bragg angle (Figure 1.1(a)). This is the basic principle of how a classic double-crystal monochromator prepares the x-ray beam with a certain energy. In reality, there is always a finite energy band of x-rays diffracted by the crystal even with perfect planes. The diffraction profile for symmetric Bragg in a highly perfect crystal neglecting the absorption effect is shown as red dashed line in Figure 1.1(b). Note that the profile is flat topped at unit reflectivity over an angular range [30, 31]. This is a consequence of having a perfect crystal whose orientation and lattice spacing match that of the x-ray beam creating a resonance condition in which the beam cannot exist in the crystal over a narrow angular range and, therefore, must be reflected out.

1.3.2 Bragg diffraction and Laue diffraction

Depending on whether the diffracted x-ray is on the same side of the crystal as the incident ray, there are Bragg (reflection) type diffraction and Laue (transmission) type diffraction, as shown in Figure 1.2 [32]. The crystal is asymmetric when the reflection lattice planes are not parallel to the crystal surface in the Bragg case (or not parallel to the normal of the crystal surface in the Laue case), and the asymmetric angle χ refers to the angle between the two. χ equals 0 when the crystal is symmetric.

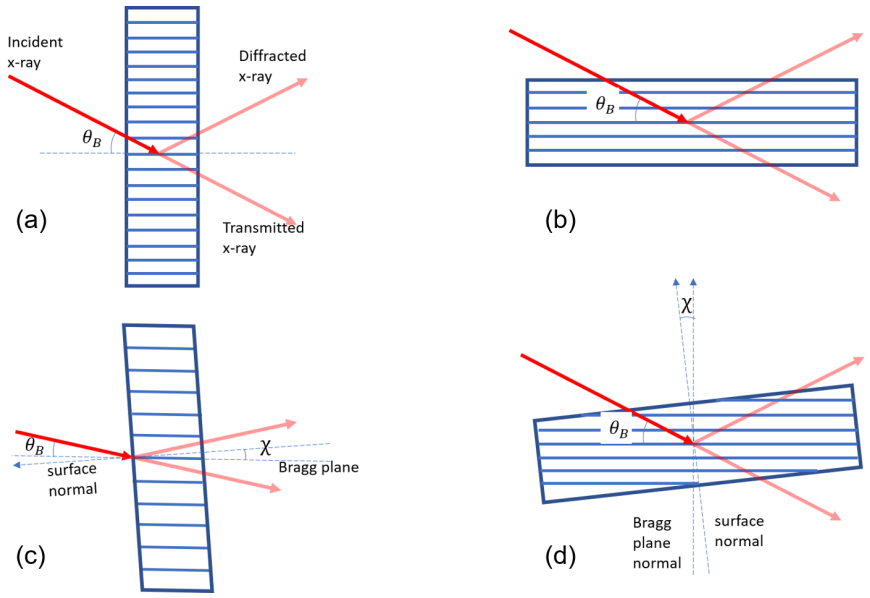

Figure 1.2: Optics of Bragg type and Laue type diffraction. (a) Symmetric Laue diffraction. (b) Symmetric Bragg diffraction. (c) Asymmetric Laue diffraction. (d) Asymmetric Bragg diffraction.

Flat Bragg crystal

For a flat perfect Bragg crystal, the reflectivity can be calculated with dynamical theory [30]. When the absorption is taken into account, the reflectivity profile is always asymmetric due to the absorption of the x-ray penetrating the crystal, as shown in Figure 1.1(b) [30, 33]. The absorption effect is diminished when

the photon energy increases. The energy band width of the reflectivity profile decreases when the photon energy increases or when the reflection index increases.

Flat Laue crystal

The reflectivity of a flat Laue crystal can also be calculated with dynamical theory. With or without considering the x-ray absorption in the crystal, the reflectivity profile is symmetric (Figure 1.3).

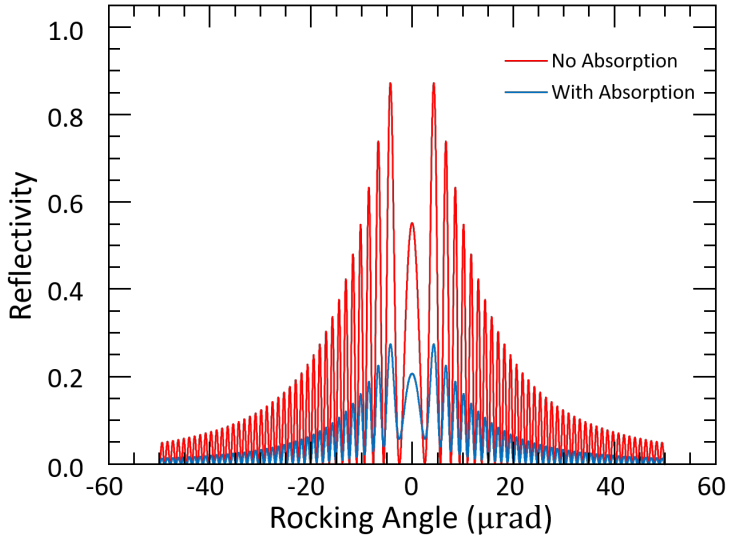

Figure 1.3: Reflectivity profile of 0.3 mm thick Si(111) Laue crystal at 12 keV.

1.4 The EDXAS System

The principle components of an EDXAS system include an x-ray source, a curved crystal polychromator and a position sensitive detector. The first version of the EDXAS system is shown in Figure 1.4 [10].

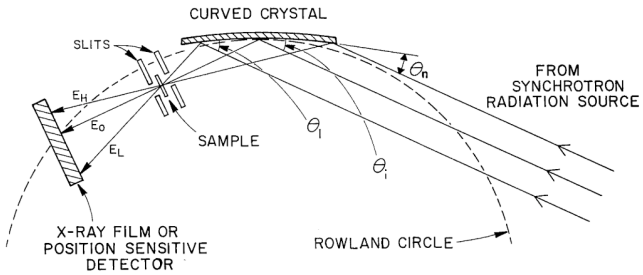

Figure 1.4: Energy dispersive XAS system in Bragg geometry [10]. Copyright (1981) The Physical Society of Japan and The Japan Society of Applied Physics.

With a curved crystal and collimated incident x-ray beam, the angle between the incident beam and the crystal diffraction plane changes following the bending curvature of the crystal. As a result, x-ray photons

with the energies corresponding to the continuously changing Bragg angles, θ_B, are reflected by $2\theta_B$ in the diffraction plane defined by the incident beam direction and the normal to the lattice plane of the crystal. In the focusing geometry, as is the case in Figure 1.4, the beam focuses at the sample location then diverges and arrives at a position sensitive detector, which correlates the energy information of the x-ray to the position of detector pixels.

The full energy range of x-ray photons diffracted by the bent crystal, ΔE, is given by [10]:

$$\Delta E = E_0 \cot \theta_0 \Delta\theta, \tag{1.2}$$

where E_0 and θ corresponds to the central x-ray on the polychromator crystal. When the central x-ray is fixed, ΔE is proportional to the variation of Bragg angle $\Delta\theta$, which is affected mainly by the bending radius of the crystal and the length of the footprint of the incident beam on the crystal. Smaller bending radius or larger footprint results in a larger energy range in the diffracted focusing beam. At the same distance from the source to the polychromator, a large diverging angle naturally provides large footprint on the polychromator crystal.

1.4.1 X-ray source

A synchrotron source has many advantages for scientific research compared to laboratory x-ray sources including, but not limited to, high brightness, small angular spread of the beam, and a large range of photon energies. The basic principle for generating synchrotron light is that the acceleration of high-speed electrons which generates radiation perpendicular to the direction of the acceleration. In the case of relativistic elections transversely accelerated by a magnetic field, relativity compresses the radiation sharply towards the original direction of election movement. Typically the magnetic force is applied by bending magnets and insertion devices (i.e., wigglers and undulators). Wiggler sources are not commonly used because of the high power radiated [34].

Bending magnet

Bending magnets are the most common synchrotron light sources used for EDXAS for the relatively large natural divergence of the beam in the horizontal direction providing the large footprint on the polychromator crystal. This wide beam can provide enough energy dispersion in the focused beam that covers the whole XANES or EXAFS spectrum, given a polychromator with reasonable bending radius, choice of reflection and source-to-crystal distance. However, when applied to time resolved experiments, most energy dispersive spectrometers with a bending magnet source may have insufficient flux. According to Hagelstein 1997 , for an EDXAS spectrum collection of a few hundred eV bandwidth at 1 kHz frequency, a total flux of 10^{12} photon/s is required [34].

Undulator

Undulator is a type of device inserted in the straight section of the storage ring, with a periodic magnetic field produced by an array of magnets which forces the electrons to oscillate and thus generates x-ray radiation. The advantage of the undulator source over the bending magnet source for EDXAS is the high intrinsic brilliance, which can easily exceed 10,000 times the radiation of a bending magnet [31]. However, due to the small diverging angle of undulator radiation, a smaller beam footprint on the crystal is expected compared to bending magnet radiation if the beam comes directly from the source to the polychromator. Kirkpatrick-Baez mirrors are usually used to increase the beam diverging angle [34]. Gap tuning and tapering the undulators are also frequently used tools to widen the undulator energy range [35]. As an example, the branch EDXAS_S of ID 24 at ESRF can cover a full spectral range of 600 eV to 3000 eV depending on the central energy [21]. With a source of high brilliance and large energy dispersion, time-resolved energy dispersive XAS experiments can be performed. Reported operational EDXAS beamlines using undulator sources are ID24 at ESRF [34] and NW2A at PF-AR [36].

1.4.2 Bent crystal spectrometer

The spectrometer is the core component in an EDXAS system. The spectrometer crystal is typically bent to a cylindrical or elliptical shape, resulting in the rotation of the diffraction planes in the crystal. As noted earlier, when the white x-ray beam hits the crystal, the energies of the reflected x-rays change correspondingly because of the continuous changing of the Bragg angle along the crystal. In the meantime, these x-rays are reflected to different directions and will focus at the so-called geometric focus. Therefore, an energy dispersive focusing x-ray beam is formed.

Bent crystal spectrometers can be categorized according to (i) the shape of the curvature, such as, cylindrically or elliptically bent crystals, (ii) how the diffraction happens (reflection or transmission in relation to the crystal), such as, Bragg type or Laue type crystals, (iii) whether the diffraction lattice plane is parallel to the crystal surface normal, such as, symmetric or asymmetric crystals, (iv) the focused dimension of the x-ray beam, such as, horizontally or vertically focusing spectrometers.

Bent Bragg crystal and bent Laue crystal

For a focusing geometry, the source will be located in a distance p from the crystal which will then focus at a distance q downstream of the crystal. All rays from the source will be diffracted according to Bragg's law from lattice planes within the crystal. The central ray from the source will intercept lattice planes at an angle of θ_0, and will be diffracted through an angle of $2\theta_0$ in the diffraction plane. The diffracted spectral range is given by Equation (1.2), where E_0 is the central energy, θ_0 is the Bragg angle corresponding to E_0, and $\Delta\theta$ is the difference of the Bragg angle between the two ends of the beam footprint of length, L, on the crystal.

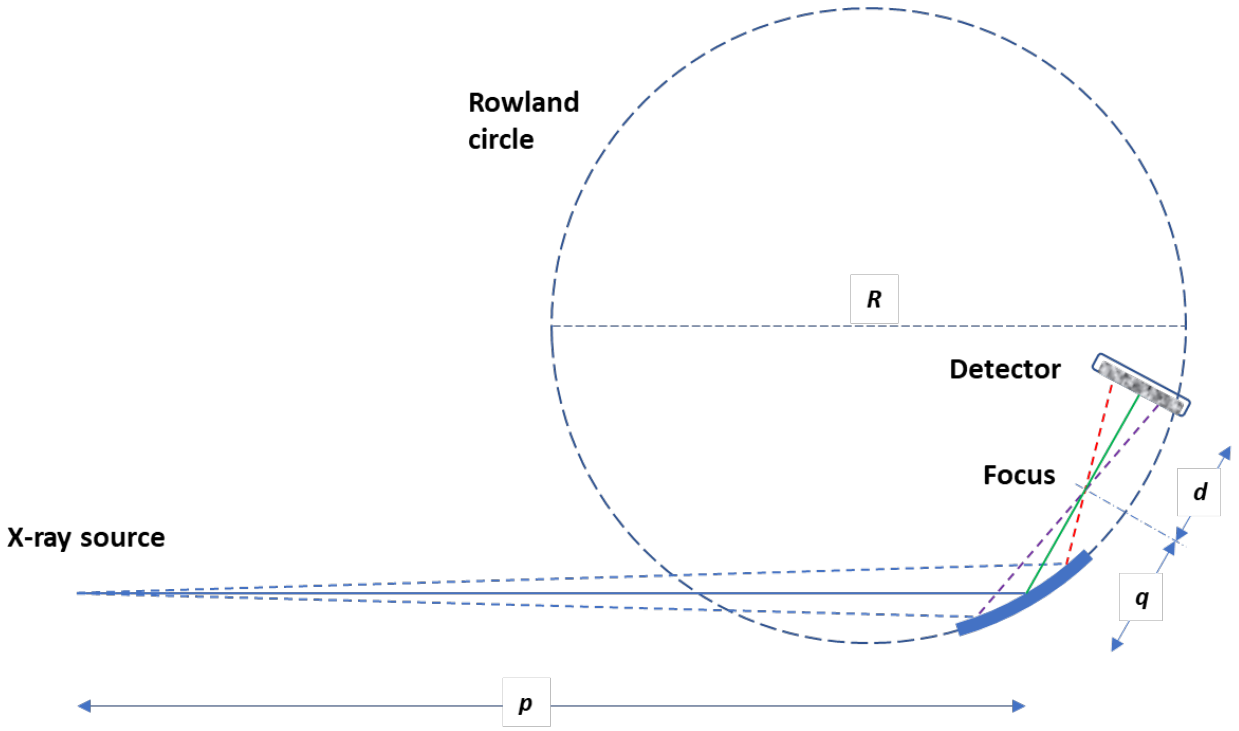

Figure 1.5: Bragg type EDXAS system layout

For a fixed central energy, the energy bandwidth is proportional to the change of Bragg angle, $\Delta\theta$, which can be calculated with [10]

$$\Delta\theta = \frac{L}{2\sin\theta_0}\left(\frac{1}{q} - \frac{1}{p}\right). \tag{1.3}$$

When the incident beam angle and the source to crystal distance is fixed, the $\Delta\theta$ is determined by the bending of the crystal. The smaller the bending radius, which makes q smaller, the larger $\Delta\theta$ is. Determining q will be addressed in section 1.4.2.

Bent Bragg crystal The typical focusing geometry of a bent Bragg spectrometer is shown in Figure 1.5. It shows the Rowland circle [37] as part of the geometry. The Rowland circle is useful when discussing point to point focusing of monochromatic beam, in which the source and focus will lie on the Rowland circle and the crystal is bent to a radius of the diameter of the Rowland circle. In the case where a focused energy dispersed beam is required, i.e., EDXAS, the source and focal point will no longer lie on the circle. This is clearly shown in Figure 1.5. In the energy dispersive situation, the source and the focus lie at the foci and the bent crystal will lie on the surface on the ellipse. This aspect is shown in Figure 1.8.

Bent Laue crystal The typical focusing geometry of a bent Laue spectrometer is shown in Figure 1.6. Again, as discussed earlier, the Rowland circle is shown for reference.

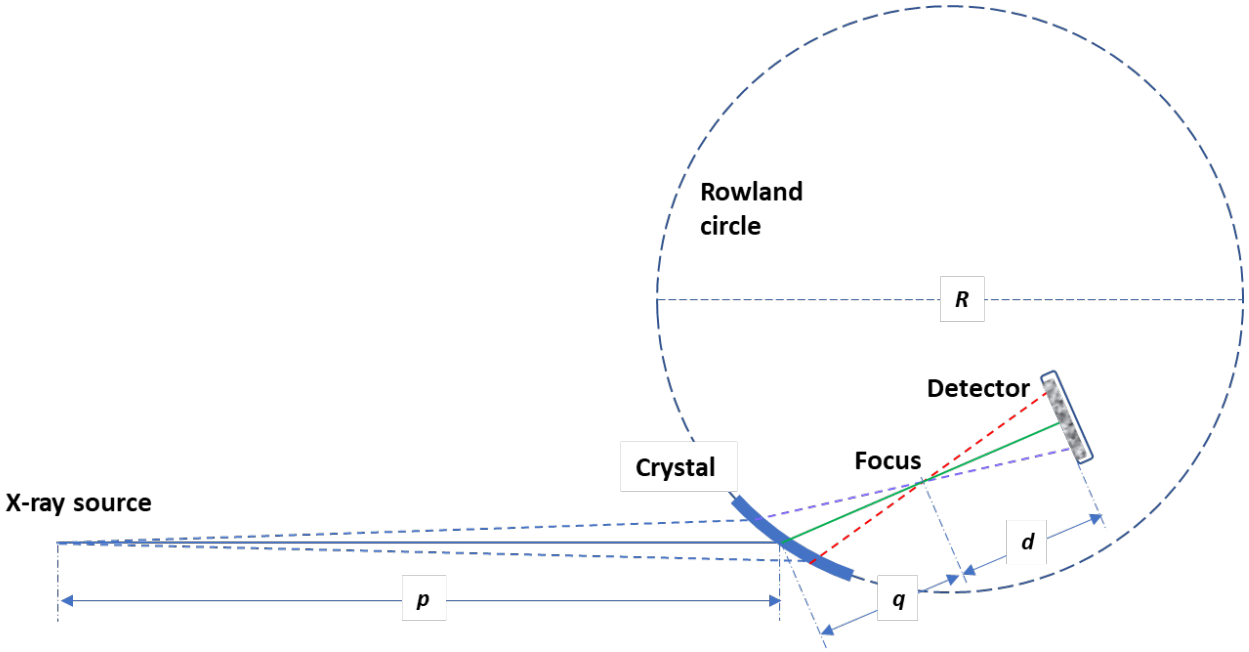

Figure 1.6: Laue type EDXAS system layout

Reflectivity of bent crystals

Reflectivity of bent Bragg crystals The reflectivity of elastically bent perfect crystals in Bragg geometry can be calculated following a model based on the dynamical theory [38]. As an example, the simulated reflectivity curve of a bent Si(111) crystal with a 3 m radius of curvature at 15 keV is shown in Figure 1.7(a) [21]. The asymmetric broadening of the reflectivity curve is caused by the change of orientation of the Bragg planes and the absorption to the x-rays as they propagate into and diffract from the crystal. The left (low angle side) of the curve corresponds to the 15 keV beam penetrating into the crystal until planes are found to diffract from. These diffracted rays then need to escape after traversing more crystal thickness. This leads to significant absorption. As the incidence angle increases the effective beam path decreases as the correct Bragg angle for diffraction occurs at a shallower depth. Ultimately, the diffracting region is at the crystal surface and the reflectivity is very high. The end result is a very asymmetric reflectivity curve.

The asymmetric broadening of the reflectivity profile of a bent crystal increases with energy and with crystal curvature. It is small at relatively low energies (e.g. 7 keV), but significant at higher energies (e.g. 18 keV). This fundamentally limits the use of a bent Bragg spectrometer to the range of 5 – 13 keV [21].

Reflectivity of bent Laue crystals For the symmetric bent Laue geometry, the reflectivity profile can be calculated in the same way as for a plane parallel perfect crystal with the dynamical theory [30, 19]. The deformation of the crystal induced by the bending is perpendicular to the diffraction plane, and the result is that the reflectivity curve is not influenced by the bending. The reflectivity profile of a symmetric bent Laue Si(111) crystal at 12 keV would look the same as Figure 1.3. Although the travel path of lower energy

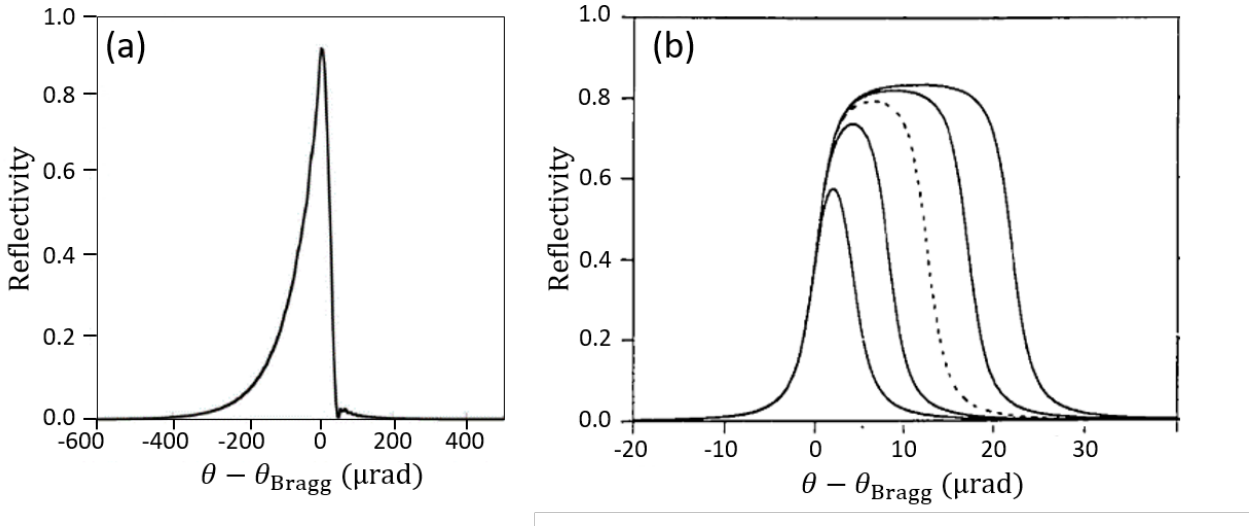

Figure 1.7: Reflectivity profiles of bent crystals. (a) Si(111) bent Bragg crystal at 15 keV [21]. (Reproduced with permission of the International Union of Crystallography. https://journals.iucr.org/) (b) 0.15 mm thick Laue type Si(400) crystal with various asymmetry angle. Larger asymmetric angle corresponds to wider reflectivity width [39]. (Reproduced with permission of the International Union of Crystallography. https://journals.iucr.org/)

photons in the crystal is a little longer than the path of higher energy photons, the asymmetric distortion of the reflectivity curve is negligible for the very thin bent Laue crystals.

Asymmetric bent Laue crystals For an asymmetric bent Laue crystal, the reflectivity profile can be calculated using the Penning & Polder model [40] for treating deformed crystals. Other approaches are (i) the multi-lamella model in which the crystal is broken into small blocks, each treated as a perfect crystal with small Darwin-width scale angular variations between the blocks, and whose intensities are summed to predict the overall reflectivity [38, 41]; (ii) Takagi-Taupin model which is a dynamical or wave theory approach for deformed crystals [42]. The change in crystal orientation due to bending is considered to be very slowly varying spatially and allows local regions of distorted crystal to be described by dynamical theory. Small deviations from the symmetric condition broadens the effective width of the reflectivity profile (Figure 1.7(b) [39]).

With a bent Laue crystal, the incident beam is focused by the corresponding Bragg planes at the crystal surface as if the crystal had no thickness and forms the so-called geometric focus. In the meantime because of the crystal's thickness, every single x-ray trajectory intercepts lattice planes inside the crystal with continuously changing Bragg angle and is focused to the so-called single-ray focus. By proper choice of the asymmetric angle along with some other parameters [43, 44], the geometric focus and single-ray focus can be brought together for a given energy which will minimize the focal size of bent Laue crystal [45, 46, 47] and, in addition, optimize the energy dispersion by eliminating the Borrmann fan effect for the central beam energy [44, 48, 49]. The energy resolution of a spectrometer optimized with proper asymmetry angle for a

specific central energy is only limited by the x-ray source size, the detector spatial resolution and the intrinsic Darwin width of the crystal. The limitation is that the proper asymmetry angle is energy dependent, thus different crystals need to be prepared for the energies of interest if one is pursuing the ultimate resolution.

Energy resolution The spread in wavelength or energy from a spectrometer crystal can be easily calculated using Bragg's law. The equation clearly shows that the changes in wavelength can occur because of angle or d-spacing changes. In terms of energy bandwidth, it can be shown that $\Delta E/E_d = \Delta d/d$ for d-spacing changes, and $\Delta E/E_\theta = \cot\theta\Delta\theta$ for diffraction angle changes. Both of these affects need to be considered in determining the overall energy resolution of a spectrometer system. Typically angle effects dominate the energy resolution of a system, however, the role of d-spacing changes cannot be ignored due to the strain arising from the elastic bending of crystals used in the system. These factors will be described in detail in subsequent sections.

Neglecting the crystal d-spacing variation resulting from the bending strain, the energy resolution of the Bragg geometry is proportional to the angular spread $\delta\theta$, which includes three contributions: (i) the size of the x-ray source, (ii) the spatial resolution of the detector, (iii) the Darwin width of the curved crystal [21].

For a bent Laue crystal, the energy resolution is also defined by the $(\delta E/E)$ equation. The difference from the Bragg geometry is that the $\delta\theta$ includes five contributions: (i) the size of the x-ray source, $\delta\theta_1$, (ii) the angle subtended by a detector resolution element from the focus, $\delta\theta_2$, (iii) the intrinsic Darwin width of the crystal, $\delta\theta_3$, and (iv) the spread of angles within the crystal that gives rise to a single exit x-ray trajectory due to the continuous changing of Bragg plane orientation caused by the bending, $\delta\theta_4$. The dominant contributions are $\delta\theta_3$ and $\delta\theta_4$ for lower energies, and $\delta\theta_1$ for higher energies [21]. Note that there is a fifth contribution defined by the Bragg plane lattice spacing variation, $\delta d/d$, which is explained in detail in Chapter 5.

For an isotropic bent Laue crystal of thickness T or Bragg crystal at a depth of T from the surface plane, using the lamellar model, the diffraction angular spread along the x-ray trajectory can be described as [45]:

$$\Delta\theta_B(T) = (T/\rho)\left[\tan(\chi \pm \theta_B) + \frac{1}{2}(1+\nu)\sin 2\chi \mp \tan\theta_B\left(\cos^2\chi - \nu\sin^2\chi\right)\right], \tag{1.4}$$

where ν is the Poisson ratio, χ the angle between the diffraction plane and the crystal surface normal and θ_B the Bragg angle corresponding to the central x-ray. It should be noted that χ equals 0 in the symmetric Laue case. The upper and lower sign corresponds to the incident ray in terms of the relative position of the incident ray and the crystal surface normal.

Because the absorption effect increases at lower energies, the Laue type bent crystal is usually designed to be very thin (tens or hundreds of micrometers), and the use for energies lower than 12 keV is not advised. As the energy gets lower, the manufacture of such thin crystal is challenging and working with the crystal is impractical. More importantly, the reflectivity value is limited by the small thickness.

Summary Generally, the Bragg type spectrometer is used at energies from 5 to 12 keV and the Laue type at energies above 12 keV [39].

To calculate the crystal reflectivity, dynamical theory [30] is the basis and is extended for treating different crystal types. This theory describes perfect, unbent crystals and its use for bent crystals is limited to estimating the diffraction from small regions of a crystal where bending can be ignored.

The Caciuffo model [38] suits for the calculation for symmetric Bragg geometry. It allows a faster evaluation than the Kato model [50] and the Takagi-Taupin model [42, 51].

The Penning & Polder model [40] treats the propagation of x-rays as changing direction gradually, and locally described with dynamical theory. This model and its extension to the case of strongly distorted crystals [52] is well suited for bent Laue geometry. It has been applied successfully in many synchrotron beamlines.

The multilamellar method assumes the crystal is composed of several layers of perfect crystals with suitable thickness and applies dynamical theory for each of these crystals. It has been generalized as a suitable model for two-moment bending Laue or Bragg anisotropic crystals [53].

Cylindrical bending and elliptical bending

For cylindrical bent crystals, the focusing geometries are shown in Figure 1.5 for the Bragg type and Figure 1.6 for the Laue type. The focal distance is defined by the well know relationship

$$\frac{\cos(\chi - \theta_B)}{q} - \frac{\cos(\chi + \theta_B)}{p} = \frac{2}{R}, \tag{1.5}$$

where p is the source-to-crystal distance, q the crystal-to-focus distance, R the crystal bending radius, χ the asymmetry angle (from the Bragg plane to the surface normal), θ_B the Bragg angle corresponding to the central x-ray (from the incident x-ray to the Bragg plane). p is positive when there is a real source, q and R are positive when there is a real image. χ and θ_B are positive when the directions are counter-clockwise. This will be discussed in detail in Chapter 5.

Equation (1.5) works for both Bragg type and Laue type crystals. It can be also written as

$$\frac{\sin(\theta_B + \alpha)}{q} + \frac{\sin(\theta_B - \alpha)}{p} = \frac{2}{R}, \tag{1.6}$$

if the asymmetry angle α is defined as the angle from the diffraction plane to the surface of the crystal. This definition is usually used for the Bragg type diffraction.

However, the cylindrical bent crystal gives broadened focus size with aberration proportional to the square of the illuminated length on the crystal [54]. To achieve an aberration-free focus point, the curvature of the crystal should fit an arc of an ellipse. When one of the foci of that ellipse is the x-ray source, the other focus becomes the focus of the crystal. The geometry is shown in Figure 1.8.

Crystal benders There are two major methods to bend the crystal to the designated curvature.

The first method uses an isosceles triangle crystal. By applying a force to the apex of the triangular crystal while having its base fixed, a triangular perfect crystal will form a cylindrical shaped curvature. As was pointed out in previous text, the ideal geometry to for dispersive XAS or XAFS is elliptical rather than

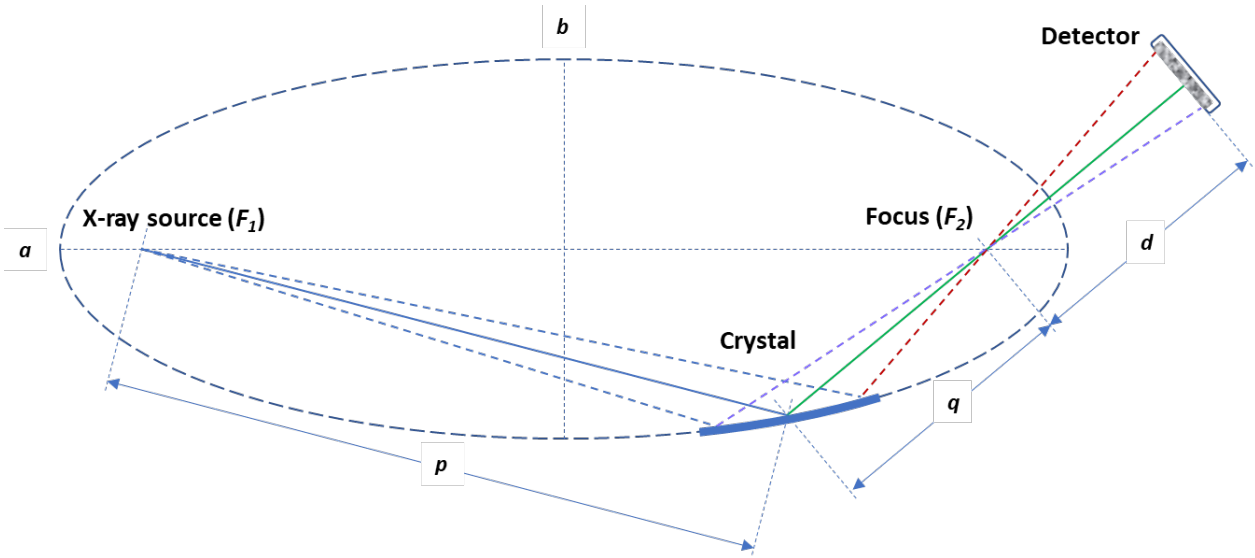

Figure 1.8: Elliptically bent Bragg type EDXAS system layout

cylindrical [18]. To achieve the elliptical shape, either the thickness or the width of the triangular crystal needs to be profiled in a specific non-linear way [18]. This is the common way of bending a crystal for the energy dispersive purpose in the early stage of EDXAS before 1990's [14, 55, 39, 18]. Disadvantages of this method include one end of the crystal must remain fixed which makes it impossible to form a consistent elliptical shape over the entire crystal length, and it requires that a different contour be used for each energy range of interest [56], which is expensive and inconvenient. In addition to these intrinsic drawbacks, the cusp form caused by imperfect clamping, heating effects, not being able to push at the point brings more uncertainty to the crystal bending properties [57].

The second method uses a rectangular crystal and a four-point bender [58], which had been a widely applied technique for bending mirrors by Underwood (1977) [59] before it was adopted by Allen (1993) [56] for crystal bending for dispersive XAFS. The general design includes two opposite end couples. Each one of them contains one fixed inner bar and one movable outer bar controlled by a high resolution stepper motor. With proper choice of different bending moments applied to the two ends of the rectangular crystal, an elliptical bend can be approximated [56, 16]. In addition, when the crystal is profiled with a small contour, an exact bend can be achieved over the entire length of the crystal [56, 60]. The mathematical form of the ideal contour is defined by Underwood [59]. With a 5 mm source size, the theoretical FWHM focal size achieved by Allen was 150 µm and the experimental FWHM focal size is 175 µm for all of the tested energy range (9 – 20 keV) [56]. Synchrotron facilities with smaller source size and longer source-to-crystal distances have been used and achieved smaller focal size (theoretical 40 µm, experimental 90 µm by Dent [57] in Daresbury; theoretical 6.5 - 11 µm, experimental 10 – 17 µm by Pellicer-Porres et al [60] in ESRF). The small focal size and great consistency between theory and experiment achieved in ESRF is also benefited by the optimized profiled rectangular crystal for x-ray in energy range of 4 – 13 keV [60, 61]. An elliptical

horizontal focusing mirror further brings down the focal spot size to the order of 5. It was stated by Pascarelli (2006) [62] that the surface and thickness homogeneity of the polychromator crystal was the limiting factor for the focal spot size. For x-ray energies higher than 15 keV where the Laue geometry is a better choice, the best focal spot size is reportedly 40 µm [35].

Other improvements in the design of the bender for solving minor issues, such as that the position of the crystal changes during the bending process due to various reasons, has been reported [63, 64, 65, 66].

While the four-point bender is the most-widely adopted method, other bender designs exist for specific needs. An example is the bender with a fixed-radius, which is machined to have the desired curvature of the crystal on one side of the bender frame, and when the crystal is attached onto the bender by forces perpendicular to the surface, it will form the curvature that is the same as the bender [49, 67, 68]. The limitation of this design is the fixed bending radius once it is produced, while the advantages are the convenience of manufacturing the bender and engaging the crystal onto the bender and the guaranteed curvature of interest, which makes it a good candidate for spectrometer prototyping.

Horizontal focusing and vertical focusing

The energy dispersive dimension of the x-ray beam prepared by the spectrometers in most of the existing EDXAS beamlines is the horizontal dimension. One of the advantages of this choice is the naturally wide shape of the bending magnet synchrotron x-ray beam, providing a long footprint on the curved crystal and, as a consequence, a large angular divergence, which usually gives large enough energy range for XANES and EXAFS. Also, for the purpose of achieving small focal size for good spatial resolution, the small vertical size of source beam is also an advantage while focusing mirrors are still used to further bring down the vertical focal size.

Vertically focusing EDXAS system with a bending magnet synchrotron x-ray source covers a smaller energy range due to the small original vertical size of the incident x-ray beam. However, the magnitude of a few hundred eV energy range from the vertically focusing system is usually more than enough for XANES study. The original horizontal beam size is preserved for fast spectroscopy scanning for large samples and 3D computed tomography can also be carried out with higher efficiency than a horizontally focusing system.

With an undulator x-ray source, a balanced system can be designed with reflection mirrors in both dimensions, while one of the two dimensions can be used to prepare the energy dispersive focusing beam and the other dimension is reserved for size expansion to cover the object. The choice of undulator source over the bending magnet source in this system has the advantage of high intensity as discussed in previous text.

1.4.3 Detection

Position sensitive detectors transforms the energy-angle relation as prepared by the spectrometer to energy-position at the detector location. Thus, the signal captured by the detector is the x-ray transmission spectra after the absorption of everything between the x-ray source and the detector.

In the early EDXAS studies, the detectors were mostly Photodiode Arrays (PDA) [69, 3]. More recently work on ID24 at ESRF has been directed at developing a scintillator-based Energy Dispersive EXAFS (EDE) detector. Scintillators that convert x-ray photons to visible light are optically coupled to Charge Coupled Device (CCD) cameras. The achievable detection rate commonly gets to about 10 kHz, and fulfills the need of many time-resolved applications [70]. In recent years, the XSTRIP detector system has been developed based on [20], pushing the detection rate to MHz level, and been successfully applied in Photon Factory [25] and ESRF [21].

Energy calibration can be carried out in several ways. One way is to match spectral features of known samples measured at standard XAS beamlines. Hundreds of eV is normally used depending on the energy separation of clear absorption features away from the edge energy. The second way is to measure the spectra of two elements simultaneously when the energy dispersion in the beam is large enough to cover the K-edge energy of both elements. Another way is to measure a single standard element and use the clear K-edge jump energy and some system dimension parameters (detector pixel size, spectrometer-to-sample and sample-to-detector distances, crystal parameters) to determine the energy distribution on the detector.

1.4.4 Mirrors

Kirkpatrick-Baez (KB) mirrors are used in EDXAS systems for different purposes. One is to bring down the beam size nearly independent of x-ray energy. For the EDXAS systems with undulator source, a KB mirror that focuses the beam before the spectrometer is necessary to bring more beam divergence from the highly collimated original beam to improve the energy range covered [71]. Mirrors with metal coating are also common tools to preserve or reduce high energy components by utilizing the energy dependent critical angle of the coating which is Z or atomic number dependent.

1.5 Applications

1.5.1 Time resolved applications

Time resolution for chemical transformation observation is one of the initial motivations for the development of the EDXAS system.

An example is the study of photo-chemical and photo-physical properties of $[Cu^{I}(NN)_2]^+$ diamine coordination complexes for its potential as a photosensitizer. Scanning monochromators have served as a powerful tool in the past decade providing good signal-to-noise ratio typically with 1 kHz laser pulses and acquisition time of up to 40 h. The EDXAS system in this application achieved better than 100 kHz repetition rate in total experimental time of about 2 h. The disadvantage of the EDXAS in this kind of application is the restriction to a transmission geometry and thus is only suitable for high concentration samples [72].

1.5.2 Differential EXAFS

A Differential EXAFS spectrum is a technique that employs the subtle changes in EXAFS signals resulting from atomic level displacements in a molecular environment. The accuracy of interatomic distance measurements requires high statistical accuracy and high stability during the experiment. With flux of more than 1×10^{13} photons/eV, relative errors of 1×10^{-6} can be produced in a few hours. High stability is also very important. A 0.01 eV energy shift would give rise to false signal. With an energy dispersive XAS spectrometer, measurements of interatomic distance at the order of femtometers and below can be made with confidence [73].

1.5.3 2D/3D XAS mapping

Benefited from the short acquisition time per spectrum per spatial position, 2D and 3D micro-XAS mapping is practically possible. For example, a 100 pixel by 100 pixel (10,000) spectra image can be acquired in a few hours [74].

A recent study spatially identified the oxidation state of Fe compounds encrusting a 1.9 billion-year-old microfossil from the Gunflint Formation in Canada with the μEDXAS technique. A 3D computed tomography by μEDXAS was carried out with 2 degree angular step size, 2 µm spatial step size for 5 slices spaced by 2 µm. Each slice takes about one to two hours [53].

1.5.4 Extreme conditions

Studies at extreme conditions (i.e., high pressure [75], high temperature [76], extreme magnetic fields [77]) are another major application scenario of EDXAS for its advantages of high time resolution, high stability, etc. An in-situ laser heating system coupled with diamond anvil cells has been equipped in ID24 at ESRF for these applications.

1.6 Discussion

One limitation of EDXAS comes with its advantage – the simultaneous data collection for the full spectral range. The application of EDXAS is almost exclusively used for transmission measurements. The use of fluorescence techniques is not easily implemented as the fluorescence signal from the target atoms triggered by the incident photons is always present and is not correlated with an incident energy. A compromise option, turbo-XAS, employs a fast scanning slit between the spectrometer and the sample and thus allows the coupling of energy and fluorescence signal, with bearable sacrifice of the time efficiency. Nevertheless, the high stability of the beam in terms of both energy and position is still a great advantage [62]. Turbo-XAS is now a routinely used technique for dilute catalysts [78].

All EDXAS beamlines worldwide are dedicated to micro focus applications, pursuing the highest possible

flux and sensitivity, which is great for what the beamlines are usually designed for. However, in many research scenarios, the ability of the beamlines is more than required for the experiment.

With this in mind, focusing the beam in one dimension for the dispersive energy band and preserving the beam size in the other dimension is a suitable design for applications where spatial information matters. This will result in a line beam. The energy dispersive wide beam can then be used for 2D and 3D XAS mapping where the width of the beam can be as wide as the object, thus, increasing the throughput and reducing the need to raster scan a spot focused beam across the object. This can speed up imaging of objects on the order of a hundred or thousand times depending on the detector and source properties. Such a system has been developed and implemented at the BMIT beamline at the CLS and is the topic of this thesis. This system operates around the Se K-edge and has high spatial resolution (about 10 µm) for EDXAS CT imaging experiments with acquisition times of about 12 minutes per slice without pushing the limits of the detector.

Improvements of energy resolution and focal spot size are expected by further implementation of asymmetry angle optimized crystals. Simulations and experiments have proved that properly choosing asymmetry angle optimizes the focal spot size [46] and energy resolution [49] at the same time. The drawback of this kind of spectrometer is that the optimization is energy specific, therefore, a set of spectrometers may need to be prepared for every element of interest and beamline setting (diffracted beam direction) need to be changed accordingly.

1.7 Project Objectives and Thesis Outline

1.7.1 Project motivation

Previous studies [49, 79] on spectral K-Edge Subtraction (spectral KES) imaging have taken advantage of the so-called 'magic condition' and achieved small focus size and good energy resolution with asymmetric bent Laue crystals. While the good energy resolution ensures the entire beam is useful for the KES imaging, the least square fit algorithm is used for solving a 'subtraction' type problem. The advantage of the good energy resolution is not fully utilized.

An obviously suitable scenario for the energy dispersive beam prepared by a magic condition monochromator could be x-ray absorption spectroscopy study. Plus, the dimension of the beam that is not altered by the monochromator provides spatial information, which is lacked by most of the existing EDXAS beamlines. With the combined information from the energy dispersion dimension and the spatial dimension of the diffracted beam, the magic condition monochromator can make the fastest (per spectrum) x-ray absorption spectroscopy technique where suitable.

1.7.2 Project objectives

The primary objective of this work was to

(I) demonstrate a properly designed energy dispersive bent Laue monochromator can achieve an energy resolution sufficient to perform wide field of view x-ray absorption spectroscopy imaging studies.

The sub-objectives in support of the primary objective were to

(II) develop an understanding of why the magic condition results in good energy dispersive properties,

(III) develop user-friendly software for data analysis including that for a similar method - spectral KES, and

(IV) lay the groundwork for a deeper understanding of the energy properties to support possible future improvements in systems of this type.

1.7.3 Thesis outline

In brief, the thesis describes the development of a novel imaging technique - Wide Field EDXAS imaging. It starts with explaining the mechanism of a magic condition monochromator with the emphasis on its energy property, continues with the data analysis software developed for the imaging technique, followed by a detailed description of the system and experiment results demonstrating its feasibility and performance, ends with a theory development that brings opportunities for the improvement of the technique and, more importantly, new insights into bent crystal optics.

Chapter 2 The 'magic condition' is the principle concept in several previously developed imaging techniques. The energy dispersion property is almost a bonus when an asymmetric bent Laue monochromator is carefully designed for minimized focal size by matching the magic condition. However, the mechanism used to achieve the magic condition does not describe the energy property of such a crystal. To understand the energy aspect of the magic condition, a new approach is developed. It describes this special condition from the angle point-of-view and explains the energy property by looking inside of the crystal. This chapter addresses Objective II.

Chapter 3 Developing a new imaging technique means there is no existing standard program for analysing the experiment data for this project. And because of the complexity of the data acquired, analysis cannot be completed in a few simple steps. Therefore, developing an automated data analysis tool is essential for the study in this project. This chapter addresses Objective III.

The development of the program has been started with simulated data before the beamtime experiments. IDL procedures and functions have been written and used for analysing data in the early stage of the project. Later, the Python based program (XSIP) that fully automates the entire data analysis workflow was developed for the following considerations.

To help the newly developed imaging technique being acknowledged and employed by potentially interested researchers worldwide, an all-in-one user friendly data analysis program is essential. Plus, the software

built for the presented Wide Field EDXAS imaging system can be easily adapted for another imaging technique - the spectral K-edge subtraction imaging, because the two techniques share the same principles and data analysis algorithms. The software is developed with Python instead of continuing with IDL for several of its advantages: (i) it is easy to learn and easy to use, which is one of the reason that (ii) it is the most popular scientific programming language for general purpose, (iii) it works better at memory management when handling large volume dataset and (iv) it is free.

Chapter 4 This paper reported the development and performance of imaging system in detail. The principles and the design of the system were explained. The result of the feasibility test demonstrated that the concept of the project was valid. Further tests for evaluating the ability and limitation of the system were reported. It has shown the ability of the technique for potential applications in biology or industry field. The work reported in this chapter also motivated us to pursue better understanding of bent Laue optics and to develop the theory reported in the next chapter. This chapter addresses the Primary Objective I.

Chapter 5 For energy dispersive x-ray imaging techniques, the energy resolution of the system is a critical factor in analyzing the fine structures of x-ray absorption spectra. The magic condition provides energy resolution that is good enough to accomplish x-ray absorption spectroscopy studies but not as good as typical double flat crystal monochromators. To investigate the mechanism for energy resolution improvement, efforts have been made to better understand bent Laue crystal optics.

The present work in this chapter describes a new approach for interpreting bent Laue diffraction from a ray-tracing point of view. This new quasi-mono beam approach explains energy and spatial properties of bent Laue optics, predicts phenomena that can improve energy dispersion related x-ray imaging techniques and provides a powerful tool for easier realization of ray-tracing simulations for bent Laue monochromators. It suggests ways to improve the developed imaging system of the thesis project and also brings insights for the improvement and design of synchrotron x-ray beamlines. This chapter addresses Objective IV.

Chapter 2

Focusing and Energy Dispersion Properties of a Cylindrically Bent Asymmetric Laue Crystal

Publication status The content of this chapter was published as a conference proceeding on SPIE Digital Library on 9 September 2019.

Citation Qi, P., Shi, X., Samadi, N., and Chapman, D. Focusing and energy dispersion properties of a cylindrically bent asymmetric Laue crystal. Proc. SPIE 11108, Advances in X-Ray/EUV Optics and Components XIV, 111080E (9 September 2019); https://doi.org/10.1117/12.2525449

Author contribution The author of the thesis proposed and developed the concept of this paper, derived the equations and wrote the major part of the paper with the advice and guidance of Prof. Chapman. All co-authors helped in revision of the math derivations and text content. Inspiration from discussions among all co-authors is unquantifiable contribution and should be acknowledged.

Preface The 'magic condition' is the principle concept in several previously developed imaging techniques. The energy dispersion property is almost a bonus when an asymmetric bent Laue monochromator is carefully designed for minimized focal size by matching the magic condition. However, the mechanism used to achieve the magic condition does not describe the energy property of such a crystal. To understand the energy aspect of the magic condition, a new approach is developed. It describes this special condition from the angle point-of-view and explains the energy property by looking inside of the crystal.

This paper addresses Objective II to develop an understanding of why the magic condition results in good energy dispersive properties.

Note The work presented in Chapter 2 is the basis of the theory developed in Chapter 5. However, due to the extension of the theory, some symbols and variables in Chapter 5 have to be defined differently from Chapter 2. These symbols and variables are listed below.

- X-ray source distance: f_1 in Chapter 2; p in Chapter 5.
- Geometric focus: f_{2g} in Chapter 2; q_G in Chapter 5.
- Single-ray focus: f_{2s} in Chapter 2; q_S in Chapter 5.
- Angle ϕ: The angle between the x-ray diffraction direction and the crystal surface normal in Chapter 2; the directional angle from the x-ray incident direction to the crystal surface normal in Chapter 5.

Focusing and Energy Dispersion Properties of a Cylindrically Bent Asymmetric Laue Crystal

Peng Qi,[1] Xianbo Shi,[2] Nazanin Samadi,[3,4] and L. Dean Chapman[4,5]

[1]Division of Biomedical Engineering, University of Saskatchewan, Saskatoon, Canada

[2]Advanced Photon Source, Argonne National Laboratory, Lemont, Illinois, USA

[3]Department of Physics and Engineering Physics, University of Saskatchewan, Saskatoon, Canada

[4]Canadian Light Source, Saskatoon, Canada

[5]Anatomy, Physiology & Pharmacology, University of Saskatchewan, Saskatoon, Canada

Abstract

Elastically bent single crystal Laue case diffraction crystals provide interesting new opportunities for imaging and spectroscopy applications. The diffraction properties are well understood, however, the ability to easily model the diffracted beams hinders assessment of the focal, phase and energy dispersive properties needed for many applications. This work begins to collect the elements needed to ray trace diffracted beams within bent Laue crystals for the purpose of incorporation into other powerful ray tracing applications such as SHADOW. Specifically, we address the condition in a bent Laue crystal where a cylindrically bent Laue crystal will focus all the polychromatic diffracted beams at a single location when a specific asymmetry angle condition is met for a target x-ray energy – the so-called 'magic condition'. The focal size of the beam can be minimized, but this condition also results in excellent energy dispersive properties. The conceptual and mathematical aspects of this interesting focusing and energy dispersive phenomenon is discussed.

Keywords: x-ray diffraction, Laue diffraction, x-ray energy dispersion, focusing x-ray optics

2.1 Introduction

X-ray Laue or transmission type monochromators have been used for many types of applications. Their use has typically been limited due to reduced efficiency compared to Bragg or reflection type monochromators. However, in high x-ray energy applications, the small Bragg angle of the incident x-rays to the crystal surface in the Bragg geometry severely limit the acceptance of the monochromator in the diffraction plane. Also, the Laue geometry is better at handling high incident powers that are generated by synchrotron or other high-power x-ray sources.

An example of the Laue and Bragg geometries is shown in Figure 2.1. Note in the figures that the lattice planes can be inclined relative to the crystal surfaces and the angle forms what is called the asymmetry angle.

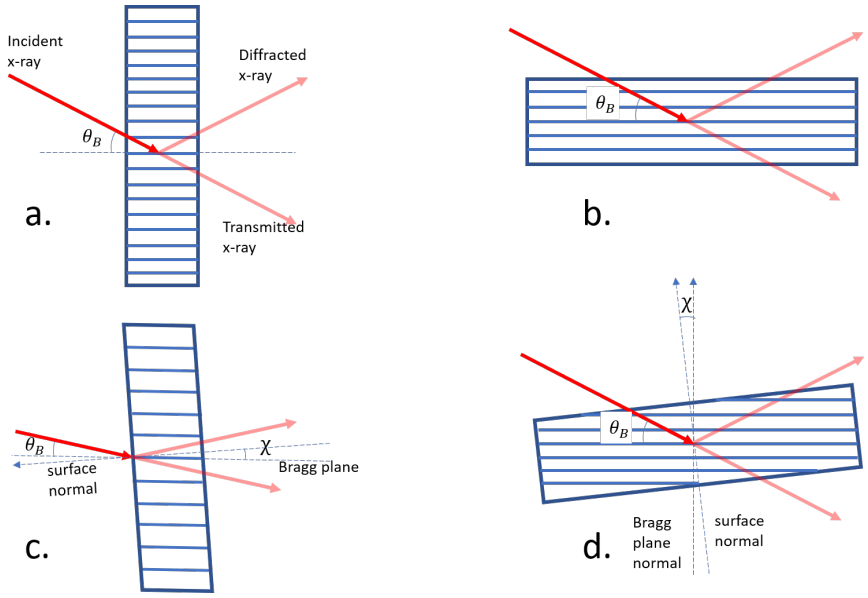

Figure 2.1: Crystal plate diffraction geometries. (a) Symmetric Laue geometry. (b) Symmetric Bragg geometry. (c) Asymmetric Laue geometry. (d) Asymmetric Bragg geometry.

This angle can expand or compress the diffracted beam size relative to the incoming size. This angle also can alter the diffraction properties of the crystal and has an impact on the Laue geometry and discussion of this angle is a significant part of this manuscript.

The properties of single crystals in both geometries are well understood [80, 45, 44]. Often, there is a need to focus or increase the energy dispersion so elastic bending of crystals is often desired. The diffraction properties of elastically bent Laue crystals can be described by wave theories [81, 51, 40] and lamella models [82]. For the discussion that follows, the crystals will be elastically bent single crystals such as silicon. Suppose, for simplicity, that a focusing bent Laue crystal is considered with a polychromatic incident x-ray beam. Similar arguments will apply for a defocusing or virtual focus system. The focal properties of such a crystal is complicated by two effects. One, there is a geometric focus arising from the overall curvature of the lattice in the diffraction plane. Also, each ray that intercepts the crystal will generate a bundle of diffracted rays that will focus (either a real or virtual focus). An example of the geometric focusing arrangement is shown in Figure 2.2(a) and the effect of diffraction on each ray in Figure 2.2(b).

Normally, the two foci do not coincide with each other. A carefully chosen asymmetry angle is critical for matching the two. It has been previously reported [83] that coinciding the geometric focus and single-ray focus optimizes the focal size. Lately, it has been also reported that when the coincidence condition is met, the energy resolution of the focused beam is optimized as well [49, 44]. This condition has been referred to as the 'magic condition' [49], and it has enabled several novel imaging techniques, e.g. spectral K-edge subtraction imaging [49, 67], wide field energy dispersive x-ray absorption speciation imaging [68], and phase preserving beam expander [44]. Principle terms needed for designing a bent Laue crystal that match the magic condition are asymmetry angle χ, Bragg angle for the center energy of interest, θ_B, crystal bending

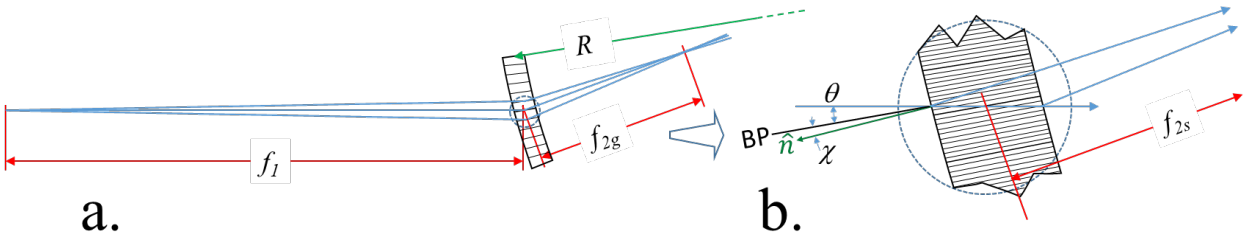

Figure 2.2: Bent asymmetric Laue focusing. Figure a shows the geometric focusing with the source at a distance f_1, the bent Laue crystal with radius R, asymmetry angle χ, Bragg angle θ and focal distance f_{2g}. Figure b shows a chosen relationship between the incident ray in relation to the Bragg planes (BP), the crystal surface normal ($\hat{n}$) and the asymmetry angle χ. The geometry shown results in rays diffracted at the entrance and exit of the crystal converging and focusing at f_{2s}.

radius, R, Poisson's ratio, ν, and source to crystal distance f_1.

The presented work explains conceptually and mathematically how the 'magic condition' is met for a bent Laue crystal.

2.2 Conceptual View of the Magic Condition

The magic condition ($f_{2g} = f_{2s}$) is illustrated in Figure 2.3, where the x-ray beams diffracted at point A, B and C go in the same direction. Point A is in the neutral plane of the crystal which is defined as the reference plane that separates the unbent crystal thickness into equal halves. The central plane is neither compressed nor expanded. Points B and C are the exit and entrance points on the crystal surface located on the concave and convex side of the crystal, respectively. As shown in Figure 2.3(a), the concave side of the crystal is compressed while the convex side is expanded.

Figure 2.3(b) gives a detailed view of the compressed half of the crystal. The magic condition $f_{2g} = f_{2s}$ implies that the diffraction angle at points A and B are the same, or $\theta_B = \theta'_B$. According to Bragg's law, when $\theta_B = \theta'_B$, the energy of the x-ray diffracted at the right end of lattice plane α is the same as the energy of the one diffracted at the left end of lattice plane β. Since the effective Bragg angle on lattice plane α and lattice plane β is increasing along the horizontal direction and θ_B equals θ'_B, lattice plane β then acts like an extension of lattice plane α at point B. And from Equation (2.28) (in section 2.3.4), we know that when this dispersive condition is met, the thickness of the crystal, T, is not part of the equation. This means at every point in the crystal along the way of the diffracted x-ray, the lattice has the same diffraction angle as the exit point B. Every diffracted x-ray on the left side of this path has lower energy, and every diffracted x-ray on the right side of this path has higher energy as indicated by the colors in Figure 2.3(a). So that lattice planes α and β are appearing as a single lattice plane where point A and B are stitched together. When this condition is met, not only the lattice planes α and β, but all lattice planes in the bent Laue crystal, act like bigger Bragg reflection planes overlapping everyone else with their Bragg angles perfectly aligned.

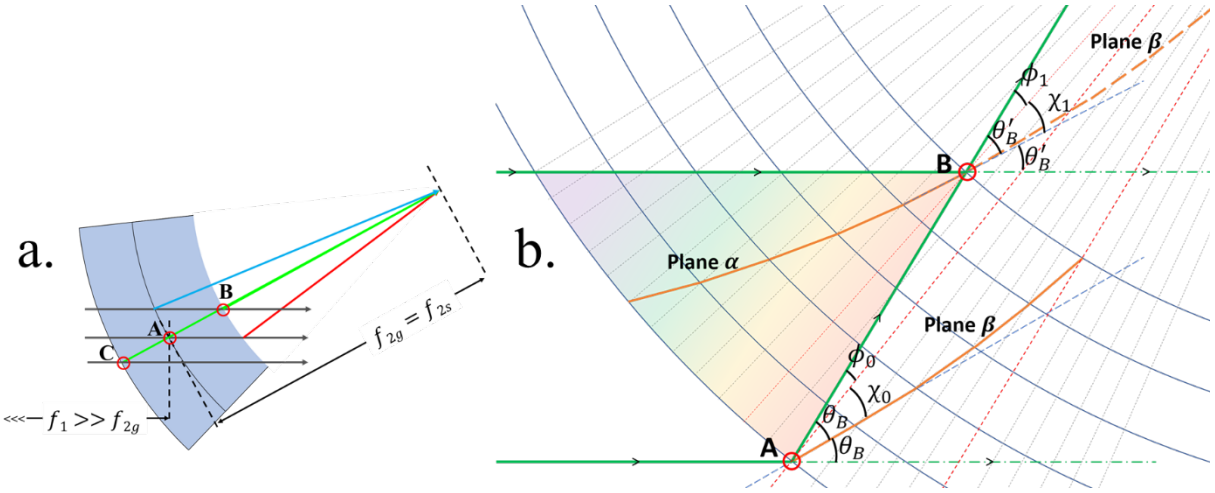

Figure 2.3: Energy dispersion of a bent Laue crystal at the 'magic condition'. Figure a shows the condition where the geometric and single-ray focus match. Figure b shows the detailed view of the relationship between bending of lattice planes α and β, local Bragg and asymmetry angles at the two locations A and B.

2.3 Mathematical View of the Magic Condition

To simplify the discussion, we take the concave compressed half of the crystal as an example. From the crystal geometry shown in Figure 2.3, one can easily tell θ_B equals the sum of χ and ϕ, where χ is the angle between the diffraction plane and the surface normal (the asymmetry angle) and ϕ is the angle between the x-ray diffraction direction and the crystal surface normal. The condition that $\theta_B = \theta'_B$ can be described as the sum of the changes of χ and ϕ equaling zero.

$$\Delta\chi + \Delta\phi = (\chi_1 - \chi_0) + (\phi_1 - \phi_0) = 0. \tag{2.1}$$

The change of χ angle is caused by the deformation of the crystal which is, for example, on the concave side of the crystal, the compression of the crystal in one dimension and the resulting elastic expansion in the two transverse dimensions. The change of ϕ angle can be determined with the magic condition geometry. Details will be discussed in section 2.3.3.

2.3.1 Thickness of a deformed crystal

Due to the bending force, the crystal is compressed on the concave side and expanded on the convex side in the direction of axis Y as shown in Figure 2.4. The compression or expansion causes an opposite deformation in the direction of axis X and Z. Axis Z (not shown in the figure) is orthogonal to the plane of XY, and not considered in the discussion here.

The thickness of the crystal (along axis X) is changed by bending considering the elastic property of the

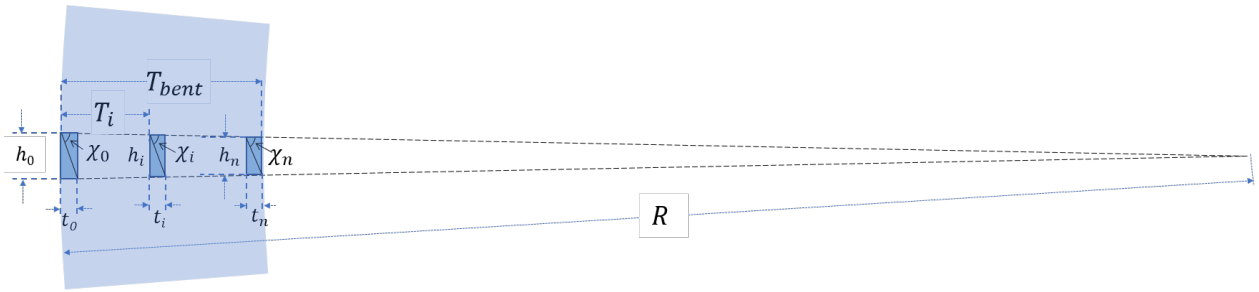

Figure 2.4: Schematic to estimate the change in bent crystal thickness and asymmetric angle χ. The relevant dimensions and angles are discussed in the text.

crystal through Poisson's ratio, which is defined by

$$\nu = -(\Delta X/X)/(\Delta Y/Y). \tag{2.2}$$

The negative sign implies that the compression (expansion) ΔY results in a transverse expansion (compression) ΔX. Thus, a crystal when bent will experience a growth in thickness on the compressed concave side and a reduction in thickness on the expanded convex side.

It can be shown that the thickness τ of bent crystal can be related to the unbent distance, x, away from the neutral plane along X direction, by

$$\tau = \left(e^{\frac{\nu x}{R}} - 1\right)\frac{R}{\nu}, \tag{2.3}$$

where R is the bending radius of the crystal plate. As a value, τ and x will be positive on the compressed side and negative on the expanded side. τ will be used in the discussion on $\Delta\phi$ and $\Delta\chi$ because using this variable avoids accounting for the change of sign when crossing the neutral plane.

For bent crystal with original thickness T, the thickness values on each side of the neutral planes are

$$\tau_{\pm} = \pm\left(e^{\pm\frac{\nu T/2}{R}} - 1\right)\cdot\frac{R}{\nu}, \tag{2.4}$$

where the plus sign refers to the compressed side of the crystal and the minus sign refers to the expanded side. Note that τ_+ and τ_- are both positive values. Therefore, $\tau = \tau_+$ and $\tau = -\tau_-$ for the compressed and expanded sides, respectively.

Since the original thicknesses for the compressed half of the crystal and the expanded half of the crystal are both $T/2$, the total thickness T_{bent} after bending with radius R is, using Equation (2.4),

$$T_{bent} = \tau_+ + \tau_- = \frac{2R}{\nu}\cdot\sinh\frac{\nu T}{2R}. \tag{2.5}$$

In the limit of large bending radius ($\nu T/2R \to 0$), the bent crystal thickness is just flat crystal thickness T, as expected.

2.3.2 The change in the angle between the diffraction plane and the surface normal, $\Delta\chi$

The change in χ over the crystal thickness is also a result of the deformation of crystal as shown in Figure 2.4. Now that we have T_{bent}, we can calculate h and t for determining $\tan(\chi + \Delta\chi)$. Assuming in the first unit cell (the left dark blue shaded box in Figure 2.4), $\tan\chi_0 = \frac{h_0}{t_0}$, then in the last unit cell (the right blue box),

$$h = h_0\left(1 - \frac{\tau_+}{R}\right) \tag{2.6}$$

$$t = t_0\left(1 + \nu\frac{\tau_+}{R}\right) \tag{2.7}$$

Therefore,

$$\tan(\chi + \Delta\chi) = \frac{h}{t} = \frac{1 - \tau_+/R}{1 + \nu\cdot\tau_+/R}\cdot\frac{h_0}{t_0} = \frac{1 - \tau_+/R}{1 + \nu\cdot\tau_+/R}\cdot\tan\chi_0. \tag{2.8}$$

Replacing $\tan(\chi_0 + \Delta\chi)$ with $\frac{\tan\chi_0 + \tan\Delta\chi}{1 - \tan\chi_0\cdot\tan\Delta\chi}$, then

$$\frac{\tan\chi_0 + \tan\Delta\chi}{1 - \tan\chi_0\cdot\tan\Delta\chi} = \frac{1 - \tau_+/R}{1 + \nu\cdot\tau_+/R}\cdot\tan\chi_0. \tag{2.9}$$

Solving the equation using the small angle approximation for $\Delta\chi$, we get

$$\Delta\chi_+ = \tan\Delta\chi = \frac{-(1+\nu)\cdot\tau_+\cdot\tan\chi_0}{(R + \nu\tau_+) + (R - \tau_+)\cdot\tan^2\chi_0}. \tag{2.10}$$

It can be generalized to both side of the neutral plane as

$$\Delta\chi = \tan\Delta\chi = \frac{-(1+\nu)\cdot\tau\cdot\tan\chi_0}{(R + \nu\tau) + (R - \tau)\cdot\tan^2\chi_0}. \tag{2.11}$$

The term τ can be replaced by the Equation (2.3) for the calculation with flat crystal thickness if needed. The total $\Delta\chi_T$ across the crystal is then

$$\Delta\chi_T = \frac{-(1+\nu)\cdot\tau_+\cdot\tan\chi_0}{(R + \nu\tau_+) + (R - \tau_+)\cdot\tan^2\chi_0} - \frac{(1+\nu)\cdot\tau_-\cdot\tan\chi_0}{(R - \nu\tau_-) + (R + \tau_-)\cdot\tan^2\chi_0} \tag{2.12}$$

$$\approx -\frac{\tau_+ + \tau_-}{2R}(1+\nu)\sin 2\chi_0 \tag{2.13}$$

$$= -\frac{T_{bent}}{2R}(1+\nu)\sin 2\chi_0 \qquad \text{or} \qquad -\frac{T_{bent}}{R}(1+\nu)\frac{\tan\chi_0}{1+\tan^2\chi_0}. \tag{2.14}$$

2.3.3 The change in the angle between the x-ray diffraction direction and the crystal surface normal, $\Delta\phi$

Figure 5 shows again the compressed half of the crystal and O is the center of the crystal bending circle. AO and BO are along the corresponding crystal surface normal directions, and AB is the path of the diffracted single x-ray in the crystal. It is obvious that the change of angle ϕ is equal to angle ω,

$$\omega = \phi_1 - \phi_0. \tag{2.15}$$

In the triangle ABO,

$$a + b = R, \tag{2.16}$$

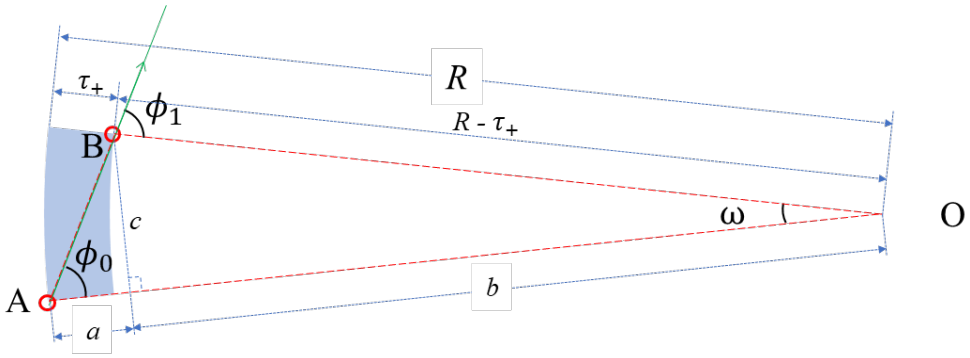

Figure 2.5: Schematic to estimate the change in ϕ. Point A and B are the same as in Figure 2.3. The relevant dimensions and angles are discussed in the text.

where

$$a = \frac{c}{\tan}\phi_0 = \frac{c}{\tan}\left(\theta_B - \chi_0\right) = \frac{\left(R-\tau_+\right)\sin\omega}{\tan\left(\theta_B - \chi_0\right)} \tag{2.17}$$

$$b = \left(R-\tau_+\right)\cos\omega. \tag{2.18}$$

Therefore,

$$\frac{\left(R-\tau_+\right)\sin\omega}{\tan\left(\theta_B - \chi_0\right)} + \left(R-\tau_+\right)\cos\omega = R. \tag{2.19}$$

Using the small angle approximation, we have

$$\frac{\left(R-\tau_+\right)\omega}{\tan\left(\theta_B - \chi_0\right)} + \left(R-\tau_+\right)\left(1 - \frac{\omega^2}{2}\right) = R. \tag{2.20}$$

Solving the equation for ω, and we get 2 solutions,

$$\omega_1 = \frac{1}{\tan\left(\theta_B - \chi_0\right)} - \sqrt{\frac{1}{\tan^2(\theta_B - \chi_0)} - \frac{2\tau_+}{R-\tau_+}}, \tag{2.21}$$

and

$$\omega_1 = \frac{1}{\tan\left(\theta_B - \chi_0\right)} + \sqrt{\frac{1}{\tan^2(\theta_B - \chi_0)} - \frac{2\tau_+}{R-\tau_+}}. \tag{2.22}$$

The first solution, ω_1, is the solution we need, while ω_2 exists mathematically but it is not practical for the optical application here. Generalizing ω_1 to both sides of the neutral plane,

$$\Delta\phi = \frac{1}{\tan\left(\theta_B - \chi_0\right)} - \sqrt{\frac{1}{\tan^2(\theta_B - \chi_0)} - \frac{2\tau}{R-\tau}}. \tag{2.23}$$

The total angler change $\Delta\phi_T$ across the entire crystal thickness is then

$$\Delta\phi_T = \sqrt{\frac{1}{\tan^2(\theta_B - \chi_0)} + \frac{2\tau_-}{R+\tau_-}} - \sqrt{\frac{1}{\tan^2(\theta_B - \chi_0)} - \frac{2\tau_+}{R-\tau_+}} \tag{2.24}$$

$$\approx \frac{\tau_+ + \tau_-}{R}\tan\left(\theta_B - \chi_0\right) \tag{2.25}$$

$$= \frac{T_{bent}}{R}\tan\left(\theta_B - \chi_0\right). \tag{2.26}$$

2.3.4 Calculation for the condition: $\Delta\chi_T + \Delta\phi_T = 0$

Adding the two angular contributions (Equations (2.14) and (2.26)) and forcing the sum to be zero results in,

$$\frac{T_{bent}}{R}\tan\left(\theta_B - \chi_0\right) - \frac{T_{bent}}{R}\left(1+\nu\right)\frac{\tan\chi_0}{1+\tan^2\chi_0} = 0, \tag{2.27}$$

or

$$(2+\nu)\cdot\tan\chi_0 + \nu\cdot\tan\theta_B\cdot\tan^2\chi_0 + \tan^3\chi_0 - \tan\theta_B = 0. \tag{2.28}$$

Solving Equation (2.28) for χ_0 is best done numerically. There is an analytical solution, but it is not insightful. When applied to high energy x-rays, both θ_B and χ_0 are close to zero. Using the approximations of $\tan^2\chi_0 \approx 0$ & $\tan^3\chi_0 \approx 0$, we then get

$$\tan\chi_0 = \frac{\tan\theta_B}{\nu+2}, \tag{2.29}$$

which agrees with the approximated solution for magic condition from other literature [44].

2.4 Energy Spread of the Single Exit Ray

With a source at an infinite distance and assuming the lattice d-spacing is not affected by the crystal deformation, the magic condition would be the ultimate energy dispersion condition at a specific energy for a bent Laue crystal. However, the energy spread mostly will not be smaller than that allowed by an unbent crystal.

When the d-spacing variation caused by the crystal deformation is taken into account, the energy spread in the single exit ray is increased according to Bragg's law.

When $\chi_0 = 0$, the d-spacing on the compression side of the crystal

$$d' = d_0\left(1 - \frac{\tau}{R}\right). \tag{2.30}$$

When $\chi_0 \neq 0$,

$$d' = d_0\left(1 - \frac{\tau}{R}\right)\frac{\cos\chi'}{\cos\chi_0}. \tag{2.31}$$

Although d' is at the compressed side of the crystal, d' is not necessarily smaller that d_0. When

$$\frac{R-\tau}{R} > \frac{\cos\chi_0}{\cos\chi'}, \tag{2.32}$$

d' is greater than d_0, which means the distance of the lattice planes are expanded rather than compressed at the compression side of the bent crystal. This condition can also be easily described with crystal original thickness and asymmetry angle.

The bandwidth $\Delta E/E$ from a bent crystal arising from d-spacing variation will be the difference between the d-spacing on the compressed side from the uncompressed side.

$$\Delta E/E = \Delta d/d = \left|\left(d_+ - d_-\right)/d_0\right|. \tag{2.33}$$

The approximated first order value of the bandwidth is

$$\frac{\Delta d}{d_0} = \frac{T}{R}\left(\cos^2\chi_0 - \nu\sin^2\chi_0\right). \tag{2.34}$$

There are other aspects that will be involved in the energy resolution of such a monochromator. There is only one energy that matches the magic condition. The divergence of the beam in the diffraction plane will create energies that 'wander off' the matching condition. Other factors will also affect the ultimate energy dispersive properties, for example, i) the spatial resolution of the detector, ii) the x-ray source size, iii) the intrinsic Darwin width of the effective Bragg plane, iv) the monochromatic beam spread on a detector [21]. When there is an asymmetry angle and the magic condition is met, it can be considered as the mono beam spread (the 4th term) is minimized. Every single-ray in the diffracted beam is monochromatic and the only adverse contribution of the crystal to the undesired energy spread in a monochromatic single-ray is caused by the d-spacing variation over the bent crystal.

2.5 Conclusions

A conceptual and mathematical model of magic condition bent Laue focusing geometry was presented with emphasis on its energy dispersive properties. The condition required for focusing and the energy dispersion are derived along with their approximate solutions. The solutions for the local χ and d-spacing values can be used to ray trace diffracted beams. This will allow us to better develop single or multiple crystal bent Laue optics for imaging and energy dispersive spectroscopy applications.

Acknowledgements

Research was funded by the Natural Sciences and Engineering Research Council of Canada (PQ, DC) and support from the Canada Research Chairs (DC).

Chapter 3

X-ray Spectral Imaging Program: XSIP

Publication status The content of this chapter is a manuscript to be submitted to *Journal of Synchrotron Radiation: Computer Programs* for publication as an article. Minor modifications may be made to the manuscript before publication.

Author contribution The author of the thesis developed the algorithm of the software introduced in this paper with Prof. Chapman, collected the data presented in the paper with help from Dr. Samadi, wrote all the code of the software, tested the software compatibility on multiple types of operating systems, wrote all sections of the paper, wrote user guide documents and is maintaining the open source GitHub repository of the software. Dr. Samadi helped in the experiments for collecting data presented in the paper, tested the program with spectral K-edge subtraction imaging data and revised the manuscript. Prof. Chapman helped developing the algorithm, wrote core prototype code in IDL (Interactive Data Language) and revised the manuscript.

Preface Developing a new imaging technique means there is no existing standard program for analysing the experiment data from this project. And because of the complexity of the data acquired, analysis cannot be completed in a few simple steps. Therefore, developing an automated data analysis tool is essential for the study in this project.

This paper addresses Objective III to develop user-friendly software for data analysis including that for a similar method - spectral K-Edge Subtraction imaging.

The development of the program has been started with simulated data before any experiments. IDL procedures and functions have been written and used for analysing data in the early stage of the project. Later, the Python based program (XSIP) that fully automates the entire data analysis workflow was developed for the following considerations.

To help the newly developed imaging technique being acknowledged and employed by potentially interested researchers worldwide, an all-in-one user friendly data analysis program is essential. Plus, the software built for the presented Wide Field EDXAS imaging system can be easily adapted for another imaging technique - the spectral K-edge subtraction imaging, because the two techniques share the same principles and data analysis algorithms. The software is developed with Python for several advantages: (i) it is easy to learn and easy to use and thus (ii) it is the most popular scientific programming language for general purpose, (iii)

it works better at handling large volume dataset and (iv) it is free.

XSIP is an open access software developed with Python 3.6. It is accessible at `https://github.com/darwinqii/XSIP` along with detailed documentation for installation and user guide.

X-Ray Spectral Imaging Program: XSIP

Peng Qi,[1] Nazanin Samadi,[2] and L. Dean Chapman[3]

[1]Division of Biomedical Engineering, University of Saskatchewan, Saskatoon, Canada

[2]Swiss Light Source, Paul Scherrer Institut, 5232 Villigen, Switzerland

[3]Anatomy, Physiology & Pharmacology, University of Saskatchewan, Saskatoon, Canada

Abstract

Spectral K-edge Subtraction Imaging and Wide Field Energy Dispersive XAS imaging are novel, related, synchrotron imaging techniques for element absorption contrast imaging and element speciation imaging, respectively. These two techniques serve different goals but share the same x-ray optics principles with a bent Laue type monochromator and the same data processing algorithms. As there is a growing interest to implement these novel techniques in synchrotron facilities, a Python based software has been developed to automate the data processing procedures for both techniques. In this paper, the concept of the essential data processing algorithms are explained, the workflow of the software is described, the main features and some related utilities are introduced.

3.1 Introduction

Bent Laue or transmission type silicon crystals have been widely used as monochromators in synchrotron x-ray studies, including K-edge Subtraction Imaging (KES) [84] and Energy Dispersive X-ray Absorption Spectroscopy (EDXAS) [21]. KES and EDXAS are x-ray techniques that serve different research purposes and have different experimental procedures and data analysis. Recently, the developments of a spectral KES imaging technique and a Wide Field EDXAS imaging technique (WF-EDXAS) blur the boundary between these two techniques as they share the same principle, similar instrumentation and similar data analysis method. The difference between the two imaging techniques are that spectral KES is meant for studying the absorption contrast between an element and its matrix at relatively high energies (e.g., $>$ 20keV), while the WF-EDXAS is for investigating the local environment and/or the speciation of an element at lower energies (e.g., $<$ 15 keV) where there is informative absorption structure in the near edge region of the element. Spectral KES and WF-EDXAS imaging will be referred to as 'spectral imaging' in this chapter for simplicity, because of the commonality of the two imaging techniques.

Both spectral KES and WF-EDXAS are enabled by a bent Laue monochromator with excellent energy dispersive properties [49, 68]. This improved energy resolution, especially in the case of KES, has resulted in the elimination of a splitter to separate the x-rays into above and below the K-edge of the contrast element

beams, giving a system that is simpler and easier to align. This ease of use, however, has resulted in a more complex image analysis requirement. The program described here was developed to take advantage of the improvement in energy resolution for KES and XAS applications.

As there is a growing interest of implementing these novel imaging techniques in facilities worldwide, a user friendly Python based software, the X-ray Spectral Imaging program (XSIP), was developed for the spectral imaging data analysis.

3.2 Theory

In conventional KES, two x-ray absorption images are collected at energies below and above the edge (usually the K edge) energy of the contrast element. A negative logarithm subtraction is done between the two absorption images so that the absorption jump by the contrast agent at the edge energy is prominent from the background absorption. In other words, the two measurements made allow for solving for two materials given the attenuation properties of the two materials.

The spectral imaging system prepares a focused line x-ray beam that has a small focal size and a good energy dispersion property in the focusing dimension (e.g., the vertical hereafter), while the other dimension (e.g., the horizontal) of the beam forms a line at the focus where the object to be imaged is located.

According to the Bragg's law, the diffraction angles and the energies of the x-rays in the focused beam are correlated. When an area detector is hit by the beam at a certain distance, the angle-energy correlation then results in a position-energy correlation on the detector in the vertical dimension. Having the monochromator match the so-called 'magic condition' [44] is critical for achieving a small focal size and good energy resolution.

When a sample is placed at the focal line, the x-rays at all energies in the beam is attenuated by the sample, and the transmitted x-rays propagate to the detector. Now the pixels on the detector captures the transmitted x-ray signal, and the vertical positions of these pixels on the detector provide the energy information of the captured x-ray photons. Therefore, an attenuation spectrum for every horizontal position of the sample is captured. Because the shape of the beam at the focus is a line beam, the contrast materials are quantified in the horizontal dimension. By scanning the sample in the vertical dimension for a 2D distribution of the contrast materials. Similarly, a rotation of the sample can be used to generate a CT image of the materials. Detailed descriptions of the system can be found in [49] and [68].

To solve for the quantities of the subject materials in the beam, the two-equation problem in KES becomes a n-equation problem or a curve fitting problem in the spectral KES case. Regardless of the number of materials, as long as less than n, the equation system is over-defined and a least square fit algorithm is used for the best solution of the quantities.

Reference mass attenuation spectra ($\frac{\mu}{\rho}(E)$ as a function of energy, E) of the materials is needed for the least square fit calculation and proper extraction of quantifiable projected density values (ρt, the mass density and thickness product). For spectral KES which is suitable for high energies, the references are

calculated with built-in functions (including absorption, elastic scattering and inelastic scattering) in the program, because of the simplicity of the near edge absorption spectrum of high atomic number elements. For WF-EDXAS, the reference data can be external measurements by dedicated XAS beamlines or internal using the spectral imaging system. Reference data measured by the system is preferred as it accounts for the monochromator energy resolution and energy calibration.

3.3 Program Workflow

The core algorithm of the spectral imaging data analysis is to fit a series of reference spectra to the measured spectrum at every location on the sample. The workflow of the program includes loading system settings and the data, preprocessing, curve fitting for XANES data and CT reconstruction if needed.

3.3.1 System settings and data loading

Some parameters of the imaging system should be defined prior to the data analysis. The critical ones are the Laue crystal asymmetry angle [49], reflection reciprocal indices, the contrast element K-edge x-ray energy, the effective pixel size of the detector and the distance between the focus of the diffracted beam and the detector. This information is essential for analysis. These parameters can be input either with an 'arrangement.dat' file which will be then read by the program, or with manual input in a prepared pop-up window when the 'arrangement.dat' file is unavailable or not preferred.

For proper data analysis, the images from the detector need to be corrected for dark current and detector response. Correction images in the form of beam off images, 'Dark' images, and beam on with no sample images, 'Flat' images, are required. A number of Dark images and Flat images (10 images for each by default) are read in and averaged. A number of 'Edge' images are read in for the energy calibration. These images are taken with an elemental form of the contrast material in the beam with no sample present. Data images with the sample or 'Tomo' images are read in and are grouped by slice if a multi-slice CT scan was done.

3.3.2 Preprocessing

Dark and flat normalization

The averaged Dark images and averaged Flat images are used to normalize the absorption of x-rays by the sample as shown (Equation (3.1))

$$\sum_{i=1}^{n}(\frac{\mu}{\rho})_i(\rho t)_i = -\ln\left(\frac{N_{Tomo}-N_{Dark}}{N_{Flat}-N_{Dark}}\right), \tag{3.1}$$

where $(\frac{\mu}{\rho})_i$ is the energy dependent mass attenuation coefficient of component i inside the sample, $(\rho t)_i$ is the projected density of component i contributing to the attenuation and N is the measured photon count for Dark, Flat and Tomo images as marked by the subscriptions, respectively.

The Flat image is also used for determining the useful field of the beam. Due to the nature of the synchrotron source x-rays, the beam intensity profile is a near Gaussian distribution in vertical dimension. Also, the detector may have spatial variations in response that needs to be accounted for in determining the useful beam region.

K-edge position and energy distribution on the detector

To determine the energy distribution information on the detector, the element under investigation in the form of a solid film or solution was placed in the beam for collecting the reference Edge images. An example of the Edge image is shown in Figure 3.1(a).

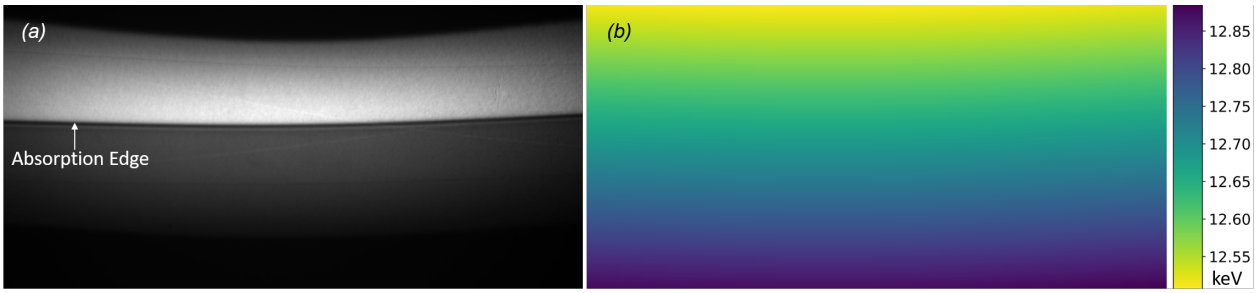

Figure 3.1: An example Edge image. (a) A 0.2 mm selenium film is used as the edge reference material. The arrow indicates the absorption edge at 12.658 keV. Data collected on Sep. 10, 2015. (b) The energy-pixel mapping in the total field of view of the detector.

Because of the absorption jump at the edge energy, the Edge image is darker on the high energy side and brighter on the lower energy side. In theory, the border of the two regions is a sharp transition. The transition takes place in a small energy range ($\frac{\Delta E}{E} \approx 10^{-4}$) because of the core-hole lifetime and the monochromator energy resolution. Derivatives of all the columns of the Edge image is taken and the peak index of the derivative curve sets the edge energy.

The energy-position information for every pixel of the detector can then be determined using Figure 3.2(a). The relation between energy and detector pixel position is given by (Equation (3.2))

$$E_{Di} = \frac{hc}{2d_{hkl}\sin\left[\theta_K + \frac{1}{2}\tan^{-1}(\frac{y_{Di}-y_K}{d_{fd}})\right]}, \tag{3.2}$$

where E_{Di} is the energy at the ith pixel of the detector, h is the Planck constant, c is the speed of light, d_{hkl} is the lattice spacing of the crystal Bragg planes, θ_K is the Bragg diffraction angle of the x-rays at the K-edge energy, d_{fd} is the focus-to-detector distance, y_K is the detector pixel location of the K-edge energy and y_{Di} is the ith detector pixel location. An example of the energy mapping in the detector field of view is shown in Figure 3.1(b).

The energy mapping can be done in another way which is more accurate but requires the reference material with identifiable absorption features at two energies. For example, the near edge absorption spectrum of selenate (in pH 7.4 Bicine buffer ($C_6H_{13}NO_4$)) has two absorption peaks at 12.667 keV and 12.681 keV.

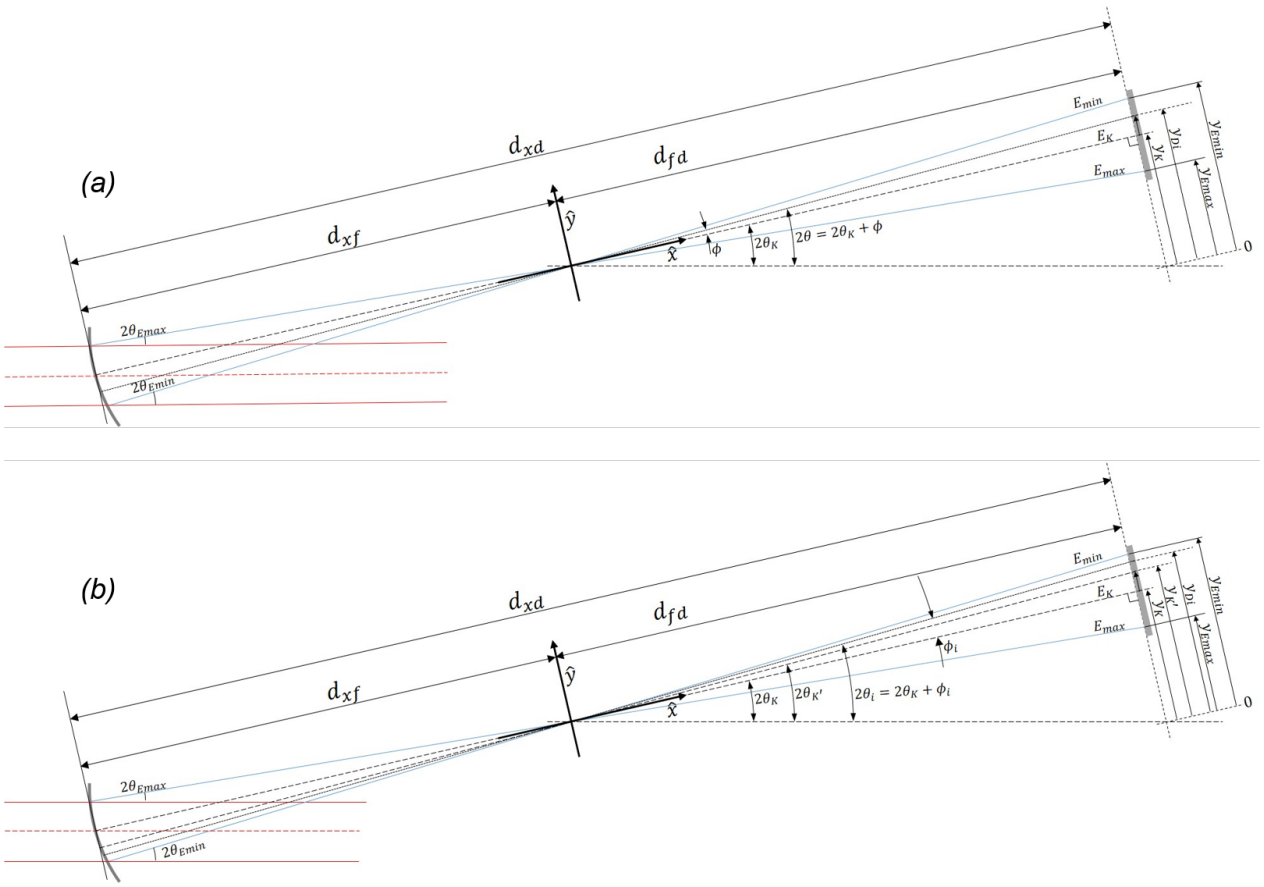

Figure 3.2: The geometry for relating the diffraction angles and the pixel positions on the detector with (a) one reference energy and (b) two reference energies. The K-edge energy, the monochromator focal distance, the focus-to-detector distance, the Bragg plane indices and the crystal asymmetry angle are the determining factors.

With the pixel positions and the energies of the two peaks, the energy distribution on the detector can be determined as shown in Figure 3.2(b) and Equation (3.2), where d_{fd} can be substituted with

$$d_{fd} = \frac{y_{K'} - y_K}{\tan(2\theta_{K'} - 2\theta_K)}, \tag{3.3}$$

where y_K and θ_K are the pixel position and the Bragg diffraction angle corresponding to the x-rays with energies at the first absorption peak, $y_{K'}$ and $\theta_{K'}$ are the pixel position and the Bragg diffraction angle corresponding to the x-rays with energies at the second absorption peak.

The edge image is also useful for determining the energy resolution of the system. Specifically, the width of the absorption edge is calculated as the full width half maximum (FWHM) of the derivative of the edge absorption spectrum. This value can be used with a Gaussian filter to blur an externally measured reference by dedicated beamline to match the measured resolution.

3.3.3 X-ray absorption near edge curve fitting

Reference mass attenuation spectra of the materials is needed for the calculation, which can be generated interally, externally or measured as described before.

Every column of a projection image contains the spectrum of transmitted x-rays for the corresponding location of the sample. With a list of mass attenuation spectra for all possible constituents, a lease square fitting is used to solve for the projected density of all constituents that best fits the measured spectrum [49, 68]. An example result for the curve fitting with least square approach is shown in Figure 3.3. In the case that some constituents are not present in the sample, the linear coefficient for the projected density is zero, theoretically. With an extensive reference library, the knowledge of possible constituents in the sample prior to the data processing is not required. However, over the energy range measured the mass absorption coefficient need to be distinctively different as a function of energy.

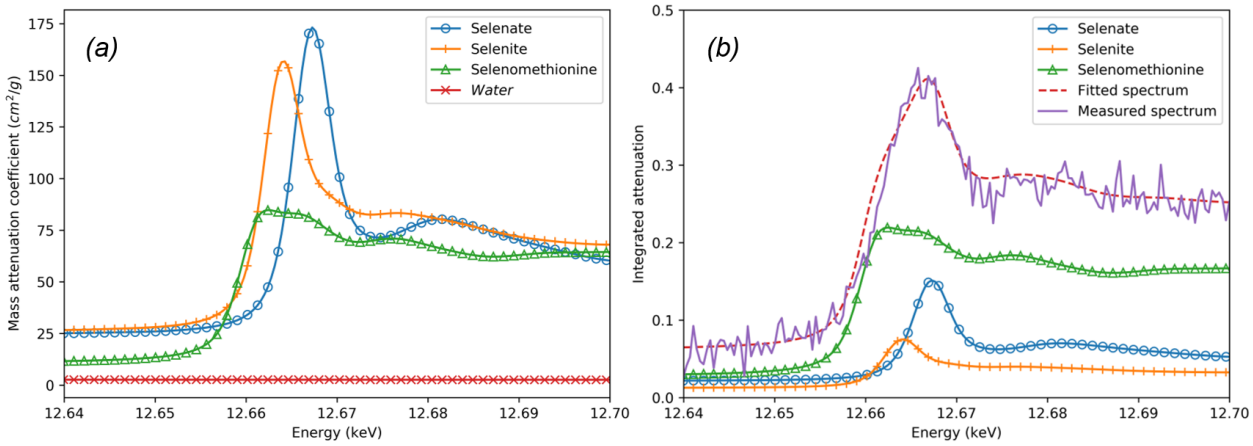

Figure 3.3: An example of spectra curve fitting. (a) The mass attenuation coefficient of reference materials. (b) Measured absorption spectrum and fitted absorption spectrum with reference materials. The reference spectra are also shown in the figure with their fitted weight (represented by the amplitudes). The attenuation by *Water* is removed from the total attenuation for better demonstration.

Therefore, a horizontal projected concentration of every reference component is acquired from one sample position. With a series of projections by scanning the sample vertically, a 2D distribution of projected concentrations is determined. With a series of projections by rotating the sample, a sinogram of every species can be acquired, which when constructed will give density values of various components. An example is shown in Figure 3.4, which demonstrates the sinograms and CT reconstruction images for samples containing different selenium species. The gray scale of the reconstruction images represents the mass density of corresponding selenium species (the gray scale bar is not shown). More experiemental details and clarifications are given in Chapter 4 section 4.2.1.

In terms of programming for the least square fit calculation, the 'torch.tensor' object from 'PyTorch' package [85] is preferred to the more popular 'numpy.array' [86]. Although the 'PyTorch' package is dedicated for machine learning tasks, the program takes advantage of its fast calculations for large multiple dimension

matrices. Roughly, it reduces by two thirds the time used for the least square fit with 'numpy.array'.

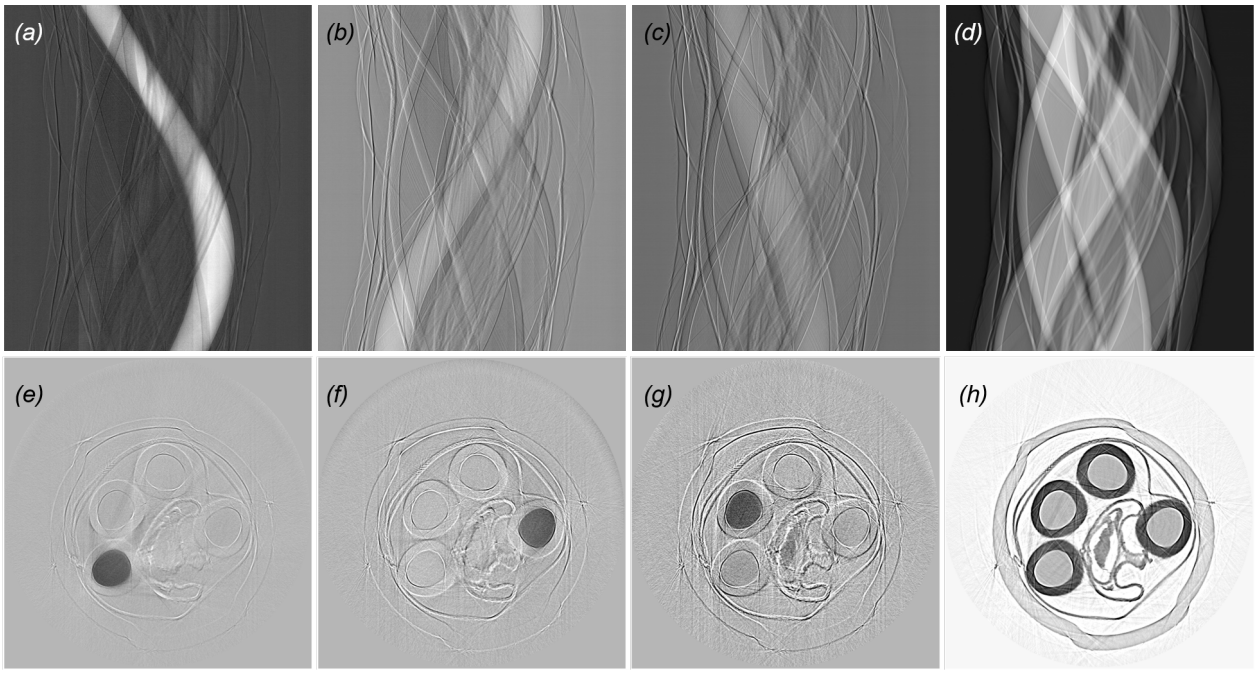

Figure 3.4: The sinograms of the projected density of (a) selenate, (b) selenite, (c) selenomethionine and (d) water. The CT reconstruction of the density distributions of (e) selenate, (f) selenite, (g) selenomethionine and (h) water. Every Se compound solution is prepared with 100 mM concentration. 7 mg/cm^3 selenomethionine was detected in the seedpod of *Astragalus bisulcatus*, which is placed in the center of the sample holder.

The previous examples show the results of WF-EDXAS imaging. Spectral KES data analysis can be done the same way. The only difference is that the provided reference material list is somewhat limited to the contrast element and a matrix material, such as water. The lack of edge structure prevents solving for species of the contrast element and the lack of strong energy dependence of the matrix material will prevent for solving for more than one components.

3.4 Features

3.4.1 Main task

Sharing the same principle theory and system design, experiment data for both spectral KES and WF-EDXAS can be processed by the XSIP software.

With the input being the Dark images, the Flat images, the Edge images and the Tomo images (the real data of the sample), the outputs of the program are individual projected densities of the reference materials. Those reference materials not present in the sample will simply result in projected densities at or near zero.

3.4.2 Result storage

During data processing, some important mid-way results have been collected and saved together with the final result in a specified destination. Some examples are the energy mapping in the beam, the useful beam region by a threshold to the intensity of the Flat image, the reference materials spectra in-use and the attenuation data corrected by the Flat and Dark images. These mid-way results are useful when in-depth evaluation of the data is necessary.

All results are saved in a PKL format file [87] for future access by the program. The final results are also saved in the TIF format images for visualization.

The system settings and the main function parameters used for the analysis are saved in a TXT file as a record for future reference.

3.4.3 Utilities

CT reconstruction

A CT reconstruction tool is provided in the program. It is a wrapper of the 'iradon' function from the 'scikit-image' Python package [88], which applies an filtered back projection algorithm [89]. Options for desired reconstruction filters provided by 'scikit-image' are available. A function for finding the rotation center index automatically in the CT projections is also provided.

A typical CT scan with the spectral imaging system can take about 10 minutes (the time varies depending on the exposure time and number of projections per CT slice). During the scanning, the incident photon flux decreases because of the decay of the electron beam in storage ring, which has an adverse influence to the data analysis. Therefore, preferred CT projection data will have an area on the left and right side of the field of view being empty during the scan (no sample is presented in this area). In this case, the change of the signals in the empty areas are only due to the electron beam decay and can be used to fix this issue.

Magic condition related calculators

The core principle that enables the small focal size and good energy resolution of the spectral imaging system is the magic condition [44]. Thus, some magic condition related calculators are provided in the program for designing and evaluating magic condition monochromators.

Variables for designing a magic condition monochromator The variables required to designed a magic condition bent Laue monochromator are: χ (asymmetry angle), θ (center ray Bragg angle), R (crystal bending radius), D (x-ray source distance) and ν (Poisson ratio of the crystal, which is assumed to be uniform in the diffraction plane of the crystal). This calculator is used for one variable defining the magic condition while the other variables are assumed to have known values.

Metric for magic condition evaluation Due to practical limitations, such as the cost of customized crystal, the limited space of a beamline or using the same monochromator for different energy applications, sometimes the monochromator is seldom at the perfect magic condition. In this scenario, an evaluation for the 'distance' to the magic condition is necessary. The quasi-monochromatic beam width is a useful metric for this purpose (see Chapter 5 section 5.5). It measures the width of an x-ray beam parallel to the diffracted center x-ray, which is zero when the monochromator matches the magic condition. It can be directly related to both the broadened focal size and the blurred energy resolution.

Calculator for energy resolution

A good energy resolution is important for XAS studies. This calculator calculates the theoretical energy resolution of the magic condition monochromator. The algorithm used in this calculator is more accurate than the classic way which sums all contributions in quadrature using a Gaussian distribution model. It calculates the mutual effect of the contributions of crystal lattice spacing variation and the finite source distance. Details are explained in Chapter 5 section 5.4.2.

3.4.4 A graphic user interface

A graphic user interface (GUI) is available in addition to using command line functions. As shown in Figure 3.5, there are two panels contained in the GUI. The 'Spectral Imaging' panel contains the main data analysis pipeline and options to tune several parameters to optimize the data analysis. The 'Reconstruction' panel contains available reconstruction tools and a display canvas for sinogram and reconstruction results. The GUI was built with the 'tkinter' package built-in with Python 3.5+.

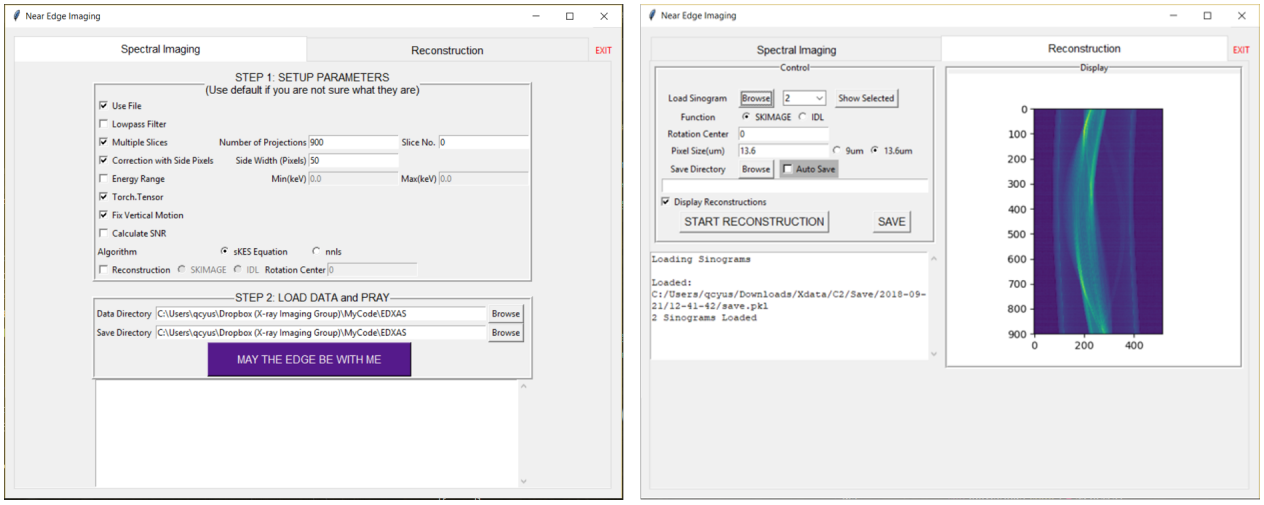

Figure 3.5: Screenshots of the XSIP GUI. (a) The 'Spectral Imaging' panel contains the main data analysis pipeline and several parameters to tune for best result. (b) The 'Reconstruction' panel contains the reconstruction tool and a display canvas for the sinogram and reconstruction results.

3.5 Summary

The X-ray Spectral Imaging Program (XSIP) is built specifically for the spectral KES and WF-EDXAS imaging techniques, which have been deployed at the Canadian Light Source BMIT-BM beamline. The program automates the analysis of the data generated from the two imaging methods and provides the flexibility of several parameters for optimizing the analysis. Quantified projected density distributions of the reference materials are the principle outputs of XSIP. In the case of computed tomography, the sinograms can be optionally constructed. A GUI is provided for the essential functions and result visualization.

XSIP is an open access software developed with Python 3.6. It is accessible at `https://github.com/darwinqii/XSIP` along with detailed documentation for installation and user guide. The program is compatible on Windows (tested on Windows 10) and Linux (tested on Ubuntu 18.04.3 LTS and CentOS 7) platforms. MacOS has not been tested.

Acknowledgements

Research was funded by the Natural Sciences and Engineering Research Council of Canada (PQ, NS, DC). Experiment data described in this paper was collected at the Canadian Light Source, which is funded by the Canada Foundation for Innovation (CFI), the Natural Sciences and Engineering Research Council of Canada (NSERC), the National Research Council Canada, the Canadian Institutes of Health Research (CIHR), the Government of Saskatchewan, Western Economic Diversification Canada, and the University of Saskatchewan (U of S).

Chapter 4

Wide Field Imaging Energy Dispersive X-ray Absorption Spectroscopy

Publication status The content of this chapter was published as an article on *Scientific Reports* on 27 November 2019.

Citation Qi, P., Samadi, N., Martinson, M., Ponomarenko, O., Bassey, B., Gomez, A., George, G., Pickering, I., and Chapman, D. Wide field imaging energy dispersive X-ray absorption spectroscopy. *Sci Rep* **9**, 17734 (2019). https://doi.org/10.1038/s41598-019-54287-8

Author contribution The author of the thesis performed all the experiments with help from other co-authors (Dr. Samadi, Dr. Martinson, Dr. Bassey), developed the algorithm and program for data analysis, analysed the data and wrote the manuscript with help from Prof. Chapman. Prof. Chapman, Prof. Pickering and Prof. George designed the project and revised the manuscript. Dr. Ponomarenko prepared the selenium samples for most of the experiments. Dr. Bassey helped with the literature review and the Introduction section. Dr. Gomez measured the energy resolution of the dispersive beam.

Preface This paper reported the development and performance of imaging system in detail. The principles and the design of the system were explained. The result of the feasibility test demonstrated that the concept of the project was valid. Further tests for evaluating the ability and limitation of the system were reported. It has shown the ability of the technique for potential applications in biology or industry field. The work reported in this chapter also motivated us to pursue better understanding of bent Laue optics and to develop the theory reported in the next chapter. Experiment procedures can be found in Appendix A.

This paper addresses the Primary Objective to demonstrate a properly designed energy dispersive bent Laue monochromator can achieve an energy resolution sufficient to perform wide field of view x-ray absorption spectroscopy imaging studies.

Wide field imaging energy dispersive X-ray absorption spectroscopy

Peng Qi[1], Nazanin Samadi[2,3], Mercedes Martinson[2], Olena Ponomarenko[4], Bassey Bassey[2], Ariel Gomez[3], Graham N. George[4,5], Ingrid J. Pickering[4,5] and L. Dean Chapman[3,6]

[1]Division of Biomedical Engineering, University of Saskatchewan, Saskatoon, Canada

[2]Department of Physics and Engineering Physics, University of Saskatchewan, Saskatoon, Canada

[3]Canadian Light Source, Saskatoon, Canada

[4]Molecular and Environmental Science Group, Department of Geological Sciences, University of Saskatchewan, Saskatoon, Canada

[5]Department of Chemistry, University of Saskatchewan, Saskatoon, Canada

[6]Anatomy, Physiology & Pharmacology, University of Saskatchewan, Saskatoon, Canada

Abstract

A new energy dispersive X-ray absorption spectroscopy (EDXAS) method is presented for simultaneous wide-field imaging and transmission X-ray absorption spectroscopy (XAS) to enable rapid imaging and speciation of elements. Based on spectral K-Edge Subtraction imaging (sKES), a bent Laue imaging system diffracting in the vertical plane was developed on a bend magnet beamline for selenium speciation. The high flux and small vertical focus, forming a wide horizontal line beam for projection imaging and computed tomography applications, is achieved by precise matching of lattice plane orientation and crystal surface (asymmetry angle). The condition generating a small vertical focus for imaging also provides good energy dispersion. Details for achieving sufficient energy and spatial resolution are demonstrated for both full field imaging and computed tomography in quantifying selenium chemical species. While this system has lower sensitivity as it uses transmission and may lack the flux and spatial resolution of a dedicated focused beamline system, it has significant potential in rapid screening of heterogeneous biomedical or environmental systems to correlate metal speciation with function.

4.1 Introduction

X-ray Absorption Spectroscopy (XAS) is one of the methods used for imaging and speciation of heavier elements in biological samples [1]. It involves measuring absorption as a function of energy near and above the absorption edge (e.g., the K-edge) of an element [2]. XAS is often divided into two distinct regions: X-ray Absorption Near Edge Structure (XANES)-region from 0 up to about 50 eV above the absorption edge and Extended X-ray Absorption Fine Structure (EXAFS)-region from 50 to 1000 eV above the absorption edge [1, 2]. Conventional x-ray and synchrotron radiation sources have been used for XAS. The advantages of using

synchrotron sources over conventional x-ray sources are the continuous spectrum, high flux and brightness, and small source size and beam divergence [90].

The classical method of performing XAS, which is mostly used, is to scan mechanically through the required energy range using flat double-crystal monochromators. Most XAS measurements of dilute systems are achieved by detecting fluorescence from the element of interest. The prevalence of using fluorescence is because of the high sensitivity which requires an energy scanning method so that the excitation energy and fluorescence can be correlated [91].

In Energy Dispersive XAS (EDXAS), a bent crystal monochromator is typically used to provide a focused x-ray beam that contains all the energies required to make an XAS measurement [91]. Bent crystal monochromators in either the Bragg (reflection) or Laue (transmission) geometry have been developed for EDXAS with the former being the first type to be developed, and the more frequently used [3, 13, 92]. The Laue geometry may require a thin crystal to avoid significant photon loss through the crystal depending on the x-ray energy chosen. High stability during measurements, acquisition of the spectral data in a very short time (few microseconds), and the simultaneous collection of the whole x-ray absorption spectrum are the reported advantages of EDXAS compared to the classical method [6].

There are few instances of the Laue geometry being used for dispersive XAS systems [39, 25, 21, 93]. One of the impediments of using this geometry is the energy blurring that occurs due to "diffraction" in depth through the crystal thickness because of the bending of the crystal, which results in the Borrmann fan [94] on the exit surface of the crystal. The energy dispersive properties essential to the success of XAS are degraded by this energy blurring.

All dedicated EDXAS beamlines use the horizontal fan of radiation to provide an energy range for XANES and EXAFS and focus the energy dispersed beam onto the sample. These systems provide high intensity, small focus size and stability for interrogating systems rapidly or in complex environments. However, since the focus sizes on both the vertical and horizontal dimension are small, speciation imaging for larger samples requires mechanically scanning the sample in both dimensions, thus the imaging efficiency is largely limited.

There is a need for EDXAS systems that are more amenable to full field imaging applications of specimens such as plants and animals. Based on previous experience with spectral K-Edge Subtraction imaging (sKES) [49, 44, 79], a bent Laue imaging system was developed on a bend magnet beamline, which diffracts in the vertical plane and preserves the horizontal dimension of the beam. This system forms a wide horizontal line beam with high flux and a small vertical focal size at the sample location, which sets the spatial resolution perpendicular to the line beam. In addition, the system has sufficient energy dispersion and resolution for selenium (Se) speciation and is completely compatible with full field imaging or computed tomography. This is achieved when a proper matching condition involving the relation between the orientation of the lattice planes and the crystal surface is met (asymmetry angle). Remarkably, the condition that provides very small focal conditions for imaging also provides very good energy dispersion [49].

Though the sensitivity is limited due to the use of transmission XAS, a potential application is for rapid

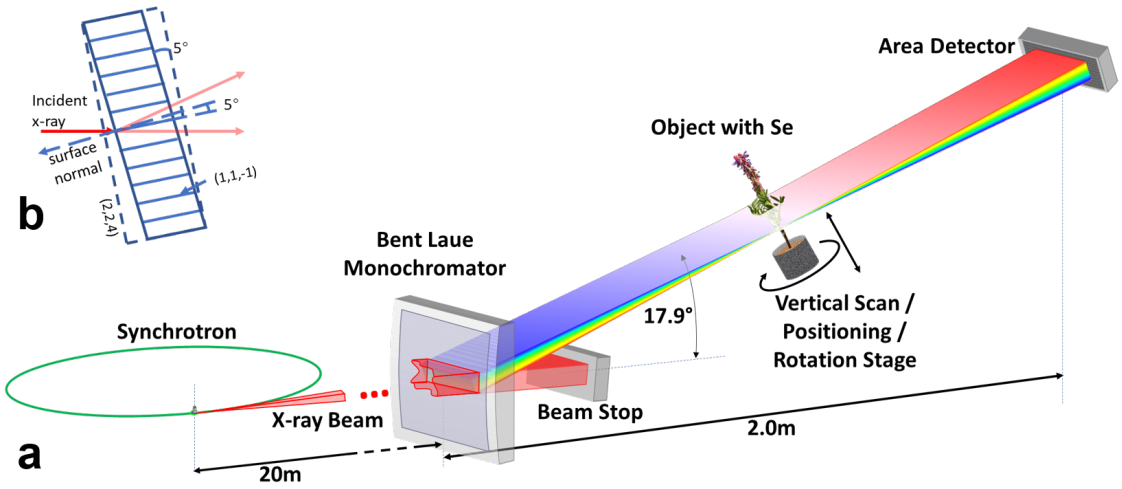

Figure 4.1: Schematic (a) of the bent Laue energy dispersive system for speciation imaging application. On the top left (b) shows the crystal orientation before being bent. There is a 5-degree angle between the normal of the crystal surface and the diffraction planes.

screening of biological / biomedical systems for the role of speciation in function. For the initial application of this approach to speciation imaging, selenium was chosen because of its biological importance and the variety of the oxidation states it presents.

Selenium is essential at trace levels in the diet for human and animal health [1, 95]. Though toxic at high concentrations [96], it has been reported that up to 1 billion people worldwide are selenium deficient [97] and several studies suggest Se supplementation can reduce the risk of some cancers [98, 99, 100, 101, 102]. Some common species of selenium that demonstrate its different oxidation states are selenate (SeO_4^{2-}), selenite (SeO_3^{2-}) and selenide (Se^{2-}). As a means of adaptation for survival in Se-rich soil, some plants, referred to as Se hyperaccumulators (e.g., *Astragalus bisulcatus* and *Stanleya pinnata*), are known to accumulate Se in excess of 1% plant dry weight [103, 104]. Due to the importance of Se, several studies using spatial imaging, speciation, quantification and distribution of Se in plants and animals have been undertaken [95, 96, 105, 106, 107, 108, 109].

For these reasons, a Se specific speciation imaging system based on a bent Laue monochromator was developed. By proper choice of crystal diffraction planes and asymmetry angle of those planes in relation to the crystal surface, an energy dispersive wide field imaging system was designed and shown schematically in Figure 4.1. The key to achieve good spatial and energy resolution is the relationship between the energy or Bragg angle for the lattice planes, and the relative angle between the lattice planes and the crystal surface (the asymmetry angle). Details are contained in the Method section.

The feasibility and performance of sKES for speciation imaging of selenium was demonstrated and compared with standard XAS in terms of acquisition time and energy resolution.

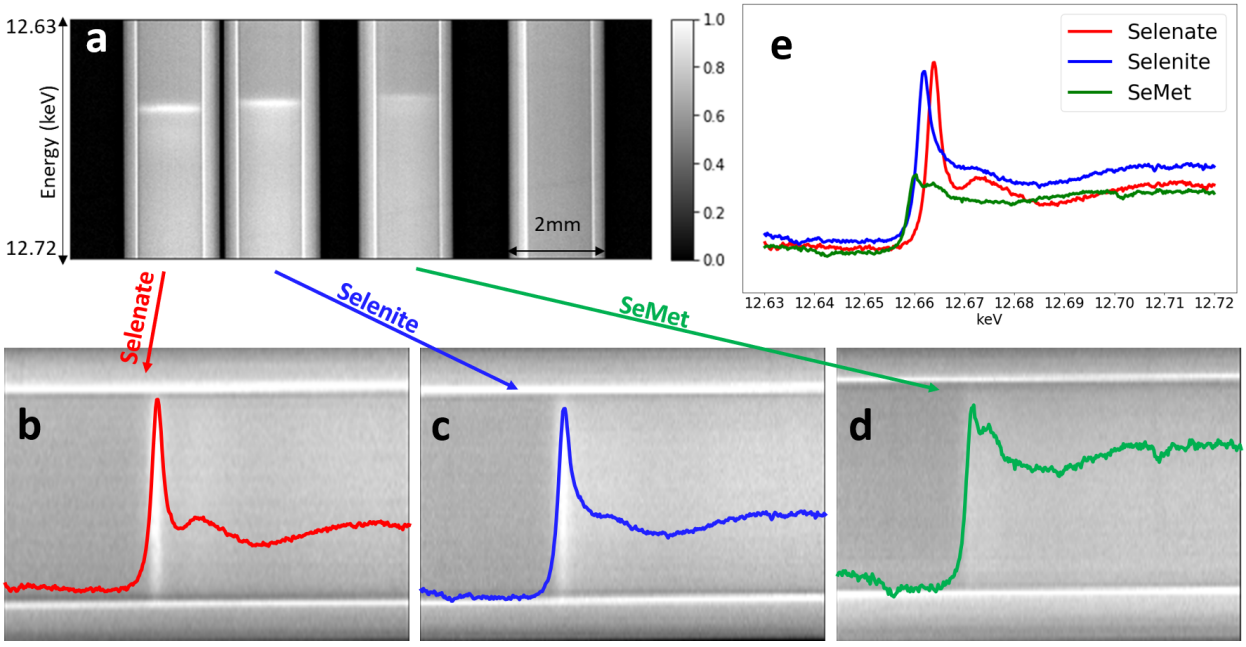

Figure 4.2: (a) A projection image of Na2SeO4 (Selenate), Na2SeO3 (Selenite), selenomethionine (SeMet) solutions and water in separate tubes (from left to right) with 100 ms exposure time. Figure (b–d) show the three tubes with Se compounds rotated so the horizontal axis is energy with superimposed (80 horizontally adjacent spectra) plots of the absorption spectra; each plot is color coded specifically to a compound. The absorption edge jump can be clearly observed in each tube and plot. (e) The absorption profiles from (b–d) superimposed for comparison.

4.2 Results

4.2.1 Feasibility test

An example of a line projection image of a series of tubes of Se compounds or water at the system focus is shown in Figure 4.2(a). The vertical direction in the image is photon energy increasing from top to bottom covering an energy range of approximately 90 eV. The sample included 100 mM solutions of Na_2SeO_4 (Selenate), Na_2SeO_3 (Selenite) and selenomethionine (SeMet) prepared with bicine buffer and placed in 2 mm internal diameter nylon tubes. As noted in the caption, the absorption edge is clearly seen, and plots of the measured absorption are shown over the tubes (Figure 4.2(b-d)). The plots when compared show the variation in edge location and structure due to speciation (Figure 4.2(e)). The acquisition time of the projection image with the Hamamatsu AA60 + ORCA Flash 4.0 detector is 100 ms.

The measured absorption profiles (Measured) were compared to high energy resolution measurements (Reference) using a dedicated XAS beamline with a double crystal monochromator [110] and are shown in Figure 4.3. The curves in the plot demonstrate the relation between mass absorption coefficient (cm^2/g) and photon energy (keV) for the Measured and Reference profiles. A 1.5 eV convolution is required to obtain a reasonable match between the Measured and Reference data, indicating the reduced energy resolution

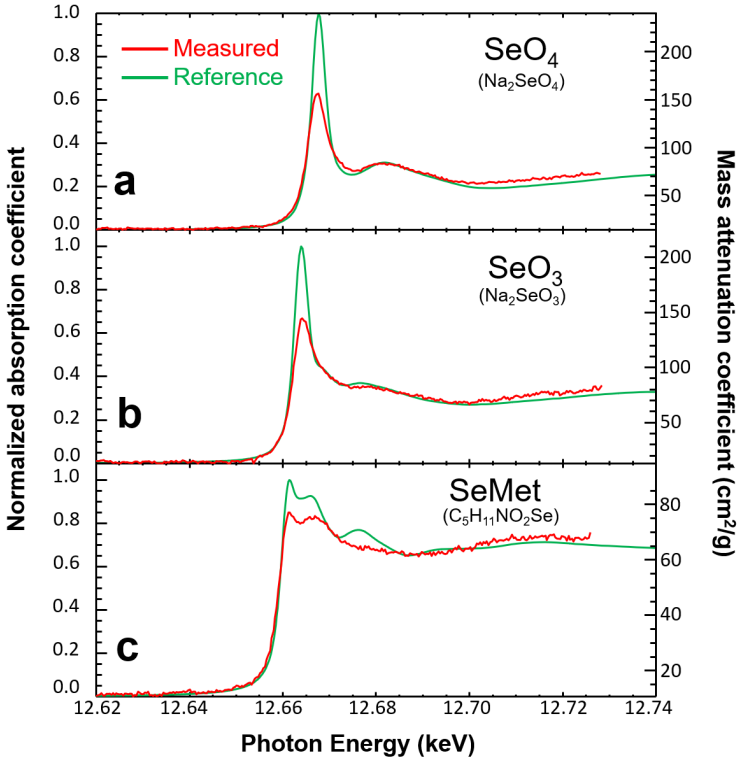

Figure 4.3: Spectrum comparison for experiment data (Measured) and traditional XAS measurement (Reference) for (a) Na_2SeO_4, (b) Na_2SeO_3 and (c) Selenomethionine

of the bent Laue system. This is expected because of the inherently poorer energy resolution of the bent Laue system. The signal to noise ratio in the measured data can be improved by increased acquisition time and signal averaging. In addition, the detector used in these experiments is an imaging detector and is not particularly well suited for spectroscopy measurements. A pixel array detector with the ability to photon count above a threshold would improve significantly the signal-to-noise.

A sample was prepared for Computed Tomography (CT) imaging that include the 100 mM solutions of the Se compounds as well as a natural *Astragalus bisulcatus* seedpod which was collected on the Saskatchewan River bank in Saskatoon, SK, Canada. CT images were acquired with the solution tubes placed in a circle with the seedpod placed in the center. Each CT slice contained 900 projections (180 degrees in 0.2-degree steps). The average acquisition time per slice was 12 minutes which is significantly less compared to a typical XAS scan reported to be hours for one slice depending on the size of the desired area for analysis [111]. While the total energy range of the beam at the focus is about 500 eV, the energy range was cropped during data collection to be about 180 eV centered at 12.658 keV (Se K-edge) for analysis. The cropping of the energy range can either be done physically with apertures in the beamline or post data collection by limiting the energy range during the data analysis. Both approaches have advantages with the use of apertures allowing reduction of dose and the use of software cropping allowing the most flexibility for data analysis. In practice, both approaches are used in the data presented.

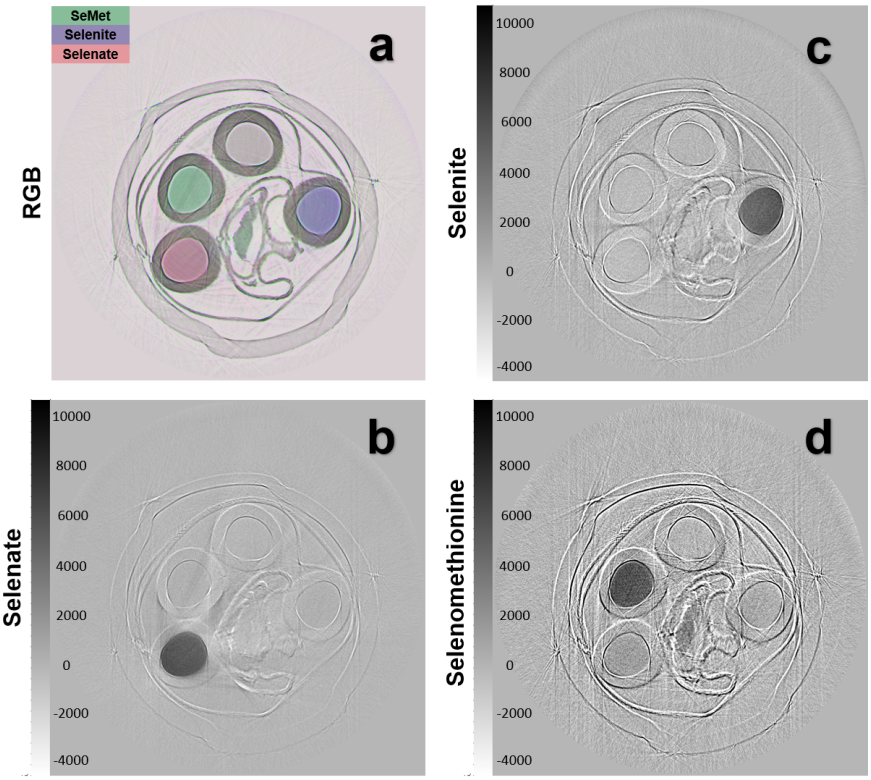

Figure 4.4: CT reconstruction of Se compound solutions. (a) A composite image of the reconstructed data with the water equivalent concentration shown as gray, SeMet concentration as green, selenite as blue and selenate as red. The individual reconstructed selenium compound concentrations are shown in (b) selenate, (c) selenite and (d) selenomethionine. The gray scale bars for (b), (c) and (d) represent the mass density values in ppm for the corresponding images.

The spectral transmission data acquired with the focused beam through the object is converted into projected concentration values using a least squares algorithm fit to the Reference data. Again, a 1.5 eV convolution to the Reference data is required before the fitting. The projected concentration line images at each angular setting then form sinograms that are reconstructed into section images using a parallel beam ramp-filter back-projection algorithm. The section images are shown in Figure 4.4.

As can be seen from the CT reconstruction, all of the tubes with specific selenium compounds are distinguished from each other. Figure 4.5 shows the measured concentration of every compound in the sample solutions, with a comparison to the actual concentration prepared. For example, in the Selenate tube, the solution contains 100 mM Na_2SeO_4, and no Na_2SeO_3 or SeMet. The measured concentration is comparable to the prepared concentration. Measurements of Selenite and SeMet solutions show better correspondence to the prepared concentration. Note the presence of negative concentration values in the figure for the selenite compound and the presence of false positive values for the selenate solution sample. The negative values are unphysical. A non-negative least squares algorithm can be used to prevent these values, but their presence indicates the lower detectability level for the system and data acquired. The presence of false values could

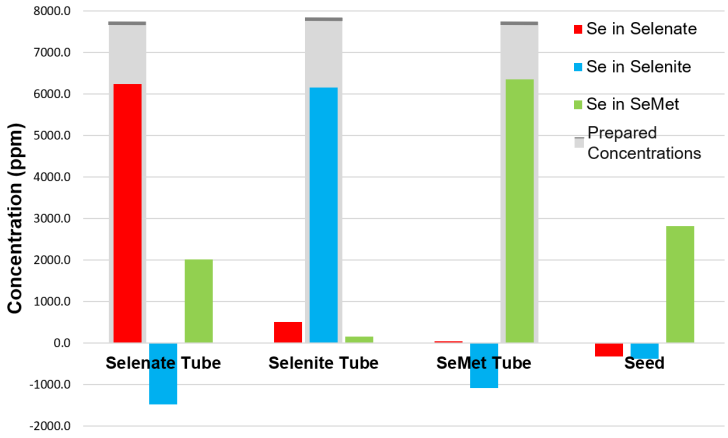

Figure 4.5: Measured (colored bars) and prepared (gray bars) concentration of compounds from reconstructions in Figure 4.4 for selenate (Na_2SeO_4), selenite (Na_2SeO_3), SeMet solutions in separate tubes, and the tube with the Astragalus bisulcatus seedpod.

be due to improper normalization, improper matching of the Reference standards resolution compared with that of the Laue configuration, or noise in the imaging system. Better thermal cooling and crystal polishing in future experiments is expected to improve the signal to noise level. Furthermore, measuring standard materials with the Laue system for use in the data analysis can avoid matching resolutions between systems.

Remarkably, significant amount of SeMet (7 mg/cm^3) is detected in the seedpod reconstruction images. The dominant form of selenium compounds in the seed of *Astragalus bisulcatus* was reported to be Se-methylselenocysteine [96]. Because the local structural environments of Se-methylselenocysteine and SeMet are similar, each bound to one methyl and one other aliphatic carbon, their XAS are almost the same in terms of edge energy and near edge structure [96]; the measured concentration of SeMet thus is expected to represent the Se-methylselenocysteine contained in the seed and is evidence for the application of the method for speciation imaging in plant samples.

4.2.2 Concentration sensitivity test

To determine the concentration sensitivity of the system for Se speciation imaging, two sets of CT imaging experiments are reported. The first experiment is a detection limit test for the concentrations, the results of which are shown in Figure 4.6. Overall, the detection limit of our speciation method is about 5 mM (400 ppm, 0.04% weight) in terms of the prepared concentration.

Other experiments were done to show that combinations of the three Se solutions could be distinguished but are not presented as they do not add significant additional information.

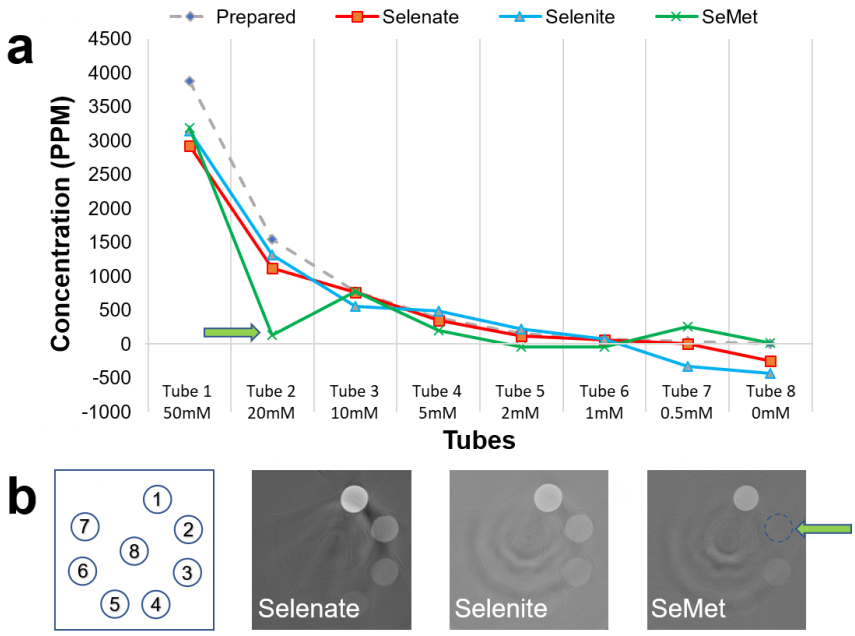

Figure 4.6: CT concentration sensitivity for selenate, selenite and selenomethionine. Figure a shows the graph of the measured vs. prepared solution concentration. The green arrow highlights an outlier value for SeMet where the solution leaked from the tube. The gray represents the prepared concentrations, (each solution sample was prepared with only one selenium species, and the gray bar only represents the species prepared in that sample), and colored bars represent measured concentrations.

4.2.3 Energy resolution

The energy resolution arises from (a) crystal lattice spacing compression/expansion, (b) source size effects, (c) the finite source to crystal distance, (d) intrinsic diffraction effect from the crystal, and (e) finite pixel size in the diffraction plane at the detector. Estimation of these contributions to the energy resolution are given in the Online Methods section. The total theoretical energy resolution is 2.52 eV. This resolution is dominated by the lattice plane expansion & compression (1.899 eV) and the intrinsic diffraction effect from the crystal (1.61 eV).

In order to independently determine the energy resolution of the monochromator, measurements and simulations were done. To assess the energy width associated with a single ray incident on the monochromator, a 10 µm diameter pinhole was placed in front of the crystal to prepare a small beam. The size of the diffracted beam at and near the Se K-edge was measured by an imaging detector (Hamamatsu AA60 + ORCA Flash 4.0) at a distance of 2.0 m from the monochromator. The contribution to the beam size at the detector is due to the Bragg plane rotation inside the wafer and, to a smaller extent, the size of beam through the pinhole (16 µm). The pinhole beam size is a combination, in quadrature, of the pinhole size (10 µm) and the bend magnet source size seen through the pinhole (12.5 µm) at the detector location.

Ray-tracing calculations were carried out with SHADOW [112] to simulate the experimental set-up and the results accurately reproduced the beam size measurements (see Figure 4.7), which demonstrate the

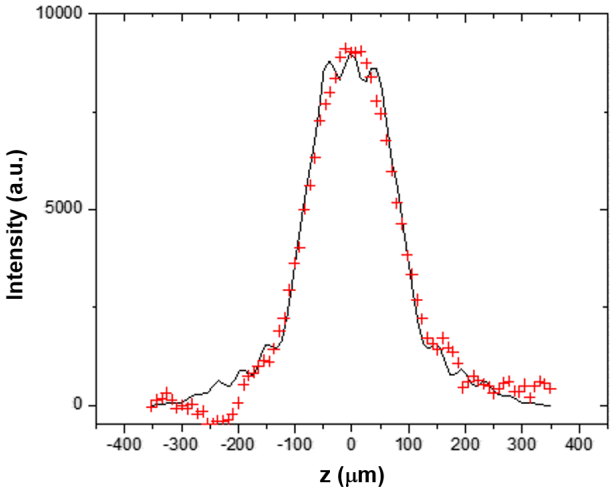

Figure 4.7: Measured (red crosses) and ray-tracing simulated peak (line) at the detector from a 10 µm diameter pinhole. Calculated peak width from sum of pinhole and Bragg planes rotation effect: 184 µm, ray-tracing result: 182 µm, measured: 181 µm.

validity of our model. The ray-tracing also shows that the peak at the detector has an energy width of 2.69 eV (More details are described in the Method section). This value matches the 2.52 eV width from the simple calculation as a sum of the various contributions.

4.3 Discussion

In previous bent Laue EDXAS systems development, the coincidence of the geometric focus and the polychromatic focus [47] has been considered to minimize the focal size [47, 83, 35] which, in part, determines the spatial resolution of the imaging system. However, the method to optimize the energy dispersion and energy resolution has not been fully exploited. This paper describes an optimized bent Laue EDXAS system for speciation imaging of Se compounds. The optimization requires a specific lattice plane and asymmetric angle and crystal thickness, which is further described in the Online Method section. This results in the system being somewhat element specific.

Also, all functional EDXAS beamlines are adapted to use the horizontal dimension of the x-ray beam to provide wide energy range with horizontally diffracting bent crystal optics [25, 21, 23, 24, 4, 28]. While this results in a small focused beam, it limits the ability to do full field imaging of larger specimens. The system presented here prepares a vertically dispersed beam with a line focus fully compatible with projection and computed tomography imaging. This allows for rapid screening of specimens.

For the system described here, the overall detection limit for Se compounds is about 5 mM (400 ppm, 0.04% weight) in terms of the prepared concentration (Figure 4.6), which is better than typical low concentration limit (0.1% weight) expected for transmission XAS. The series of concentration measurements from CT

showed overall agreement of 5% to the prepared values. The advantage in this case is demonstrated by the ability to do full field quantifiable 2D or 3D imaging in plant applications. As an example, some selenium accumulating species of *Astragalus* and *Stanleya* are able to contain selenium up to 1% dry weight [103, 104, 113].

Referring to Figure 4.5, there are two aspects that are of concern and require further attention. One, the systematic underestimation of the contrast values that were present in each of the tubes by approximately 20% at high concentration values (> 7000 ppm). Also, there are some false positive and negative concentration values noted earlier. The reasons for these discrepancies are currently being investigated both in changes to our data analysis (non-negative least squares and iterative reconstruction methods) and to our monochromator (improved thermal cooling and better polishing to remove fine spatial structure in the imaging beam).

The energy resolution was modeled and measured to be about 2.69 eV, which is sufficient to visualize the near edge structure or speciation of the Se compounds. The system's ability to do so for Se can be seen in Figure 4.2(a) where the 'white line' for the three Se compounds can be clearly observed at different vertical (energy) locations. From the SHADOW simulation and pinhole test, we found 2.69 eV energy width. This is consistent with the 1.5 eV Gaussian blurring of measured data from the dedicated beamline, as well as with other works that model bent Laue EDXAS systems [21].

Contributions to the energy resolution are dominated by the intrinsic diffraction effect from the crystal and the lattice plane expansion and compression, the latter being driven by the crystal thickness and the bending radius. The two contributions are quite close and indicate that the system is nearly optimal for the material/reflection chosen and the desired focal length of the EDXAS system. Other contributions to the energy resolution such as source size effect, beam divergence and the detector pixel size were found to be minimal.

For the examples shown, the effective pixel size was 13.6 µm parallel to the line focus and the estimated size at the focus was calculated to be 8 µm. The energy range covered could be as much as 500 eV, but in practice was limited to $100 \sim 200$ eV to minimize dose. The delivered dose with the full 500 eV beam was measured at about 20.4 Gy/s with 250 mA ring current. A CT slice dataset with 900 angular steps covering 180 degrees took 12 minutes. The time limitation could be improved by reducing detector readout and motor motion time.

The data analysis method is based upon calculated or measured reference absorption coefficient values with a least square algorithm used to extract concentration or projected concentration values. The energy dependent absorption for all the compounds considered have differing near edge structure including the edge location. It is these differences that give the ability to independently determine from the imaging data, the amount of those materials in either projection or computed tomography. The measurements are interpreted against the reference data in a least square algorithm, to extract projected values for the three Se compounds and water from the data, such as shown in Figure 4.3. This gives projected values for a single line where

the focused beam intercepts the object. That line can form the basis of a set of 2D or projection images by scanning the object vertically through the beam, or a set of sinograms if the object is rotated. A CT example of a test object is shown in Figure 4.4.

The ability to determine independent projected concentration (2D) or concentration (3D) values depends on having differences between the energy dependence of the absorption for each of the materials. In other words, over the energy range used by the system, the absorption coefficient for each of the materials must be linearly independent. For this reason, the method is not able to extract independent plastic or water values in the data presented. However, there is no limitation, other than computation, to the number of compounds that can be included in the analysis as long as they meet the linear independent condition. The same analysis method has been used to extract as many as six independent compounds [67].

In summary, the reported imaging system (a) provides a wide horizontal imaging beam that is vertically energy dispersed allowing for wide field imaging applications, (b) uses an asymmetric bent Laue crystal monochromator which provides minimized focal size and optimized energy dispersion that is sufficient for Se speciation imaging, (c) has reasonable concentration sensitivity for rapid screening of specimens, and (d) provides quantifiable concentrations in 2D and 3D imaging.

4.4 Methods

4.4.1 Imaging system

As shown in the system layout (Figure 4.1), the incident polychromatic beam from the synchrotron source strikes the bent Laue monochromator whose specific lattice planes diffract the imaging beam in the vertical plane. The lattice plane, asymmetry angle, and crystal thickness are chosen to match the imaging energy and desired angular energy dispersion properties. After the monochromator, the direct beam is stopped to prevent unnecessary scatter from reaching the object and detector. A lead shield is used at this location to allow the diffracted beam for this purpose. The bent crystal focuses the beam at the object location where translation and rotary stages position the object in the imaging beam and allows for linear scanning through the beam for projection imaging and rotation for computed tomography. The beam then diverges in the diffraction plane and after some drift distance, the beam is then intercepted and detected by an area or imaging detector.

The horizontal position (x) in the detector corresponds to the horizontal width of the beam and object, while the vertical position corresponds to the energy of the beam (E) defined by the monochromator and distance from the focus or the monochromator. The area detector thus measures the spectral transmission in an x-energy or x-E projection. Scanning the object vertically along y-axis (perpendicular to the central diffracted x-ray beam) gives an x-energy-y data set while rotating the object by an angle θ about the y-axis gives an x-energy-θ data set from which a slice can be reconstructed.

Using the Canadian Light Source (CLS) biomedical bend magnet beamline [114], the photon rate per hori-

zontal beam width and per milli-ampere storage ring current was measured at 1.07×10^9 photons/(s·horizontal-mradian·mA) with an air-filled ionization chamber. As a comparison, a calculation of the vertically integrated photon rate for the same conditions using a double-crystal Si(111) Bragg monochromator was 1.18×10^9 photons/(s·horizontal-mradian·mA), which is quite close to the measurement with our bent Laue monochromator. The dose rate was about 20.4 Gy/s with 250 mA ring current.

Monochromator

For this work around the Se K-edge at 12.658 keV, 0.80 mm thick silicon wafers were purchased and were thinned to 0.30 mm for optimal Laue geometry diffraction performance (Addison Engineering, Inc). The wafers had a [2,2,4] surface normal and the (1,1,-1) reflection was used. The (1,1,-1) lattice planes were inclined 5 degrees from the surface normal in the diffraction plane which was chosen to provide nearly optimal energy dispersive properties [32]. The crystal wafer of the monochromator was bent to a 2.0 m radius which resulted in a 0.96 m focus downstream at the sample location.

The frame bender was designed to be cylindrical on one side with a radius of 2.0 m, and flat on the other side. The window through the frame bender is narrower on the cylindrical side and wider on the other side, allowing the emergent beam to go through the bender after diffraction. The crystal was fixed on to the cylindrical side of the frame bender with stainless steel ruler and binder clips (Figure 4.8).

The vertical size of the incident beam on the crystal give an energy range of about 500 eV. However, given the vertical distribution of the intensity, the energy range was typically limited to about half that value. The detector was approximately 2.4 m downstream from the monochromator (Figure 4.1).

4.4.2 Bent Laue energy dispersion geometry (magic condition)

In the Laue or transmission geometry with a bent crystal plate, each incident x-ray beam that strikes the crystal undergoes two overall effects that influence the focal and energy dispersive properties. These two effects are shown in Figure 4.9. Each incident polychromatic x-ray that traverses the crystal in a focusing geometry will diffract in depth through the crystal. Typically, these will result in a bundle of diffracted x-rays that exit the crystal plate on a converging trajectory that will focus at the so-called 'polychromatic' or 'single-ray' focus designated as f_p in Figure 4.9. Other incident rays that are parallel but displaced in the diffraction plane will form a focus due to the overall bending of the crystal (f_g in Figure 4.9). This is analogous to the focusing of a lens and the formation of a geometric focus. Typically, these two foci will occur at different distances downstream of the crystal. The energy of each diffracted beam is mostly defined (aside from crystal expansion and compression due to bending) by the scattering angle of the beams or the 2θ angle (2θ in Figure 4.9). Using Bragg's law, these scattering angles are directly related to the diffracted beam's wavelength or energy using $\lambda = 2d \sin\theta$. By inspection of the figure, if each ray that exits the crystal arrives at a single focus ($f_p = f_g$), then it will have a unique wavelength or energy irrespective of the origin of the ray (either from the geometric effects of the lattice curvature or diffraction in depth through the crystal or

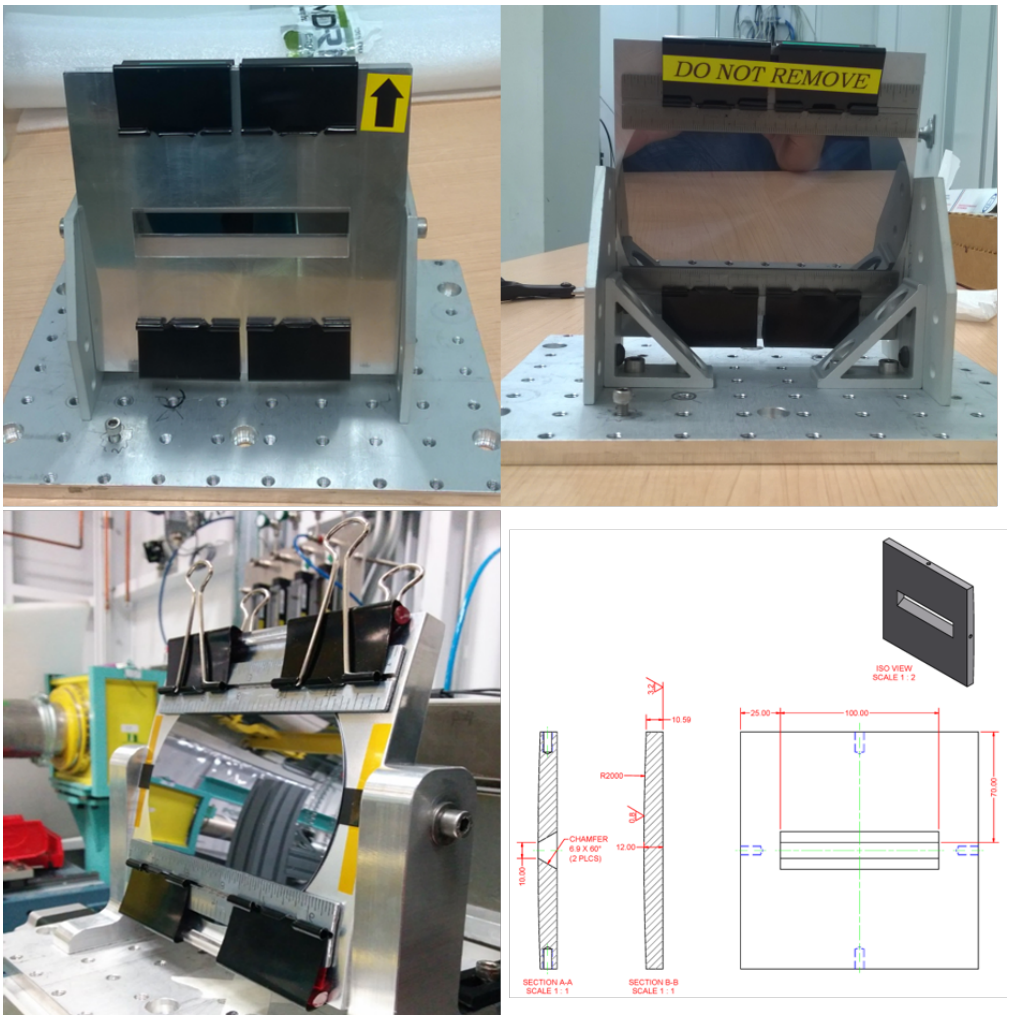

Figure 4.8: Bent Laue monochromator. The designed radius of the cylindrical side of the frame bender is 2 m.

polychromatic focal effects). Again, this is true only if the lattice is not compressed or expanded on bending. Thus, if the two focal lengths are matched, then it should be possible to (1) have a very small focal spot and (2) very good energy dispersive properties. This is the geometry used for the bent Laue energy dispersive monochromator and is what we call the 'magic condition' [44, 115].

The 'magic condition'

As noted for minimal focus and optimal energy dispersive properties, both the geometric and polychromatic foci should be co-located. The geometric focus is defined by [47]:

$$\frac{\cos(\chi \mp \theta_B)}{f_g} - \frac{\cos(\chi \pm \theta_B)}{f_s} = \frac{2}{R}, \tag{4.1}$$

where χ is the asymmetry angle of the lattice planes, θ_B is the Bragg angle, f_g is the geometric focus distance, f_s is the source to the crystal distance and R is the bend radius of the crystal. The signs identify

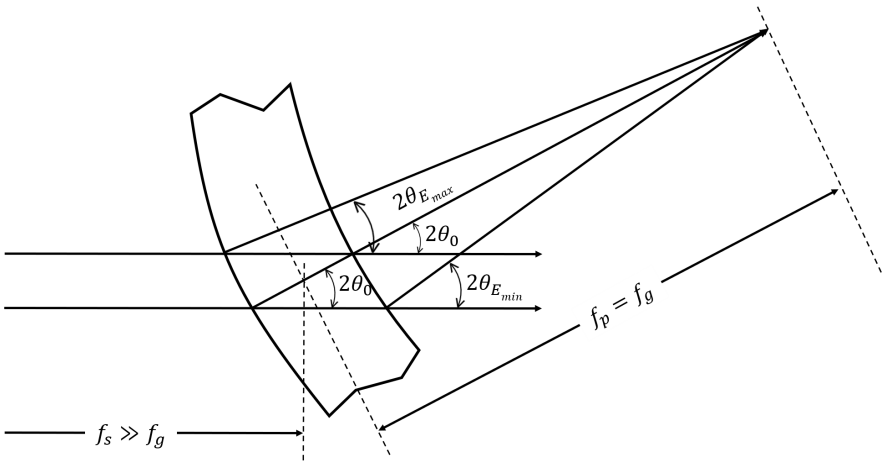

Figure 4.9: Bent Laue geometry crystal that meets the 'magic condition' has overlapped geometrical focus (f_g) and polychromatic focus (f_p).

the relationship between the entrance and exit beams, the lattice planes and the bend radius.

The polychromatic focus is defined by [44]:

$$f_p = \pm \frac{R \sin 2\theta_B}{2 \sin(\chi \pm \theta_B) + (1+\nu) \sin 2\chi \cos(\chi \pm \theta_B)}, \tag{4.2}$$

where ν is the Poisson ratio, and the sign convention is the same as in Equation (4.1).

The condition for achieving a small focus is achieved when (1) the upper sign is used and (2) the geometric focus, f_g, and polychromatic focus, f_p, match. The solution for the focal match is best done numerically. The solution will be independent of the bend radius and will relate the Bragg angle to the asymmetry angle. A simple solution can be found if one assumes that the source to crystal distance is large ($f_s \gg f_g$) and the photon energy is high ($\theta_B \ll 1$) which leads to:

$$\chi \approx \frac{\theta_B}{2+\nu}, \tag{4.3}$$

which indicates that the asymmetry angle choice needs to be small for the magic condition to be met.

A [2,2,4] type wafer was used as the monochromator crystal. The (1,1,-1) lattice planes were used for the diffraction planes for the monochromator. With no asymmetry angle the (1,1,-1) lattice planes will be perpendicular to the wafer. However, the wafer was cut with a 5 degree offset towards the [2,-2,0] direction, which results in a 5 degree asymmetry angle of the (1,1,-1) plane. Based on the discussion above, the focal matching condition of the asymmetric angle would be 4.47 degrees. This mismatch of the asymmetry angle from the ideal condition will result in focal blurring and minimal effect on the energy dispersive properties, which will now be discussed.

Beam size at focus For the conditions given, with an asymmetry angle of 5 degrees for the (1,1,-1) lattice planes, there is a mismatch from the calculated 4.47 degrees value needed to match the two foci. This mismatch of 0.53 degrees will result in an estimated beam size at the geometric focus of 5.87 µm. The beam

size at the focus will also be affected by the source size which for the BMIT bend magnet is 118 µm FWHM in the vertical dimension. The de-magnified source size will then be 5.12 µm (source to crystal distance of 22 m and crystal to geometric focus 0.96 m). The combination of the two contributions results in a focus of 7.79 µm when added in quadrature.

Estimated depth of field The detector used for imaging had a pixel size of 13.6 µm. A conservative estimate of the spatial resolution would be no less than about 30 µm. The energy range used in the data analysis corresponds to a vertical beam size of about 0.5 mm which focuses about 1 m from the crystal. Thus, the distance from the approximate 8 µm focus where the beam size is equal to the spatial resolution is about 4.4 mm. Therefore, the estimated depth of field is about 8.8 mm.

Energy resolution with the magic condition The magic condition results in every ray diffracted within the crystal arriving at the same focus. The energy spread of each ray going towards that focus (focal ray) will be set by the range of energies that occur from where the ray originates at the entrance side of the crystal to where it exits on the other side. Since every incident beam ray that intersects a focal ray will have the scattering angle, 2θ, then it also has the same Bragg angle, θ. Under this condition, the spread of wavelengths in the focal ray will be set only by the spread of lattice plane spacings along the focal ray. Specifically, in terms of energy wavelength or bandwidth

$$\frac{\delta\lambda}{\lambda} \;=\; \frac{\delta d}{d} \;=\; \frac{\delta E}{E}, \tag{4.4}$$

where λ is the x-ray wavelength, d is the lattice plane spacing, and E is the x-ray energy. Also, the equation holds for the magnitude of the values. For a symmetric Laue type crystal bent to a cylinder, the lattice plane spacing on the entrance and exit surfaces can be easily calculated with

$$\frac{\delta d}{d} = \frac{T}{R}, \tag{4.5}$$

where R is the bending radius of the crystal, and T is the thickness of the bent crystal, which can be calculated with the nominal thickness T_0 in absence of bend, and the bending radius R [115]

$$T = \frac{R}{\nu}\left(e^{\frac{\nu T_0}{R}} - 1\right). \tag{4.6}$$

Therefore, the energy spread along the focal ray is

$$\frac{\delta E}{E} = \left(e^{\frac{\nu T_0}{R}} - 1\right)/\nu, \tag{4.7}$$

which is determined by the thickness of the crystal T_0 and the bending radius R. For an asymmetric bent Laue crystal, the lattice spacing is affected by the asymmetry angle χ, but the effect is small when χ is small. Given the parameters for our crystal, $\delta E/E = 1.50 \times 10^{-4}$. At the Se K-edge energy 12.658 keV, the energy resolution, ΔE_1, for the single ray energy spread is 1.899 eV. ΔE_1 can be improved through two approaches:

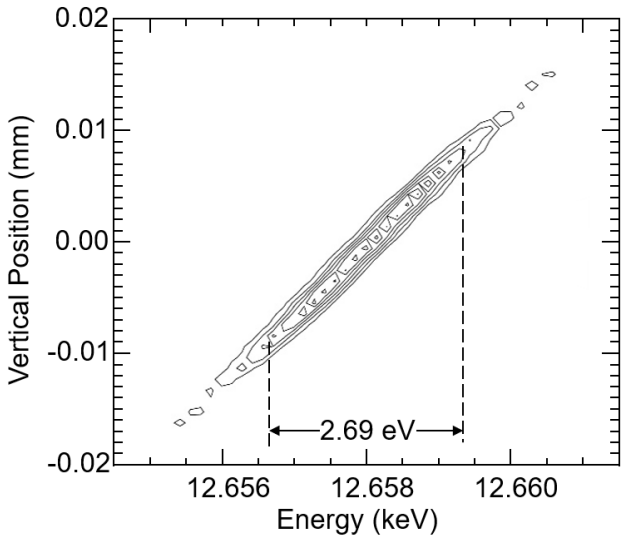

Figure 4.10: Ray tracing results for a 10 µm pinhole in front of the crystal showing the energy resolution and the vertical size (sizes are shown in cm).

decreasing the crystal thickness reduces the reflectivity of the bent crystal while allowing more transmission; in addition, increasing the bending radius reduces the energy bandwidth of the bent crystal.

There are four additional contributions to the total energy resolution of the monochromator. (i) The source size angular spread at the crystal. At 22 m distance from the source, the angular spread of the source, $\Delta\theta_s$, is 5.364 µrad, which results in $\Delta E_2 = 0.429\,\text{eV}$ at the Se K edge energy 12.658 keV. (ii) The intrinsic Darwin width of the curved Laue crystal, which results in $\Delta E_3 = 1.609\,\text{eV}$. (iii) The vertical divergence from the finite source distance, which results in $\Delta E_4 = 0.338$ eV. (iv) the pixel size of the detector. With the 13.6 µm pixel size and 1460 mm focus-to-detector distance, the contribution $\Delta E_5 = 0.376$ eV. The total energy resolution, ΔE, can be calculated with

$$\Delta E = \sqrt{\Delta E_1^2 + \Delta E_2^2 + \Delta E_3^2 + \Delta E_4^2 + \Delta E_5^2} = 2.576 \text{ eV}. \tag{4.8}$$

Energy resolution measurements

Measurements were made in order to independently determine the energy resolution of the monochromator. A 10 µm diameter pinhole in front of the crystal was used to prepare a small beam onto the monochromator, and the size of the beam was measured at the detector. The contribution to the beam size at the detector is due to the Bragg plane rotation inside the wafer

$$2 \cdot \theta_{\text{rotation}} \cdot 2.41\text{m} - \frac{T \cdot \sin 2\theta}{\cos(\chi + \theta)} = 168 \text{ µm} \tag{4.9}$$

and, to a smaller extent, the size of the pinhole (16 mm). Ray-tracing calculations (SHADOW [112]) were conducted to simulate the experimental set-up and the results accurately reproduced the measurements (see Figure 4.7), which demonstrate the validity of our model.

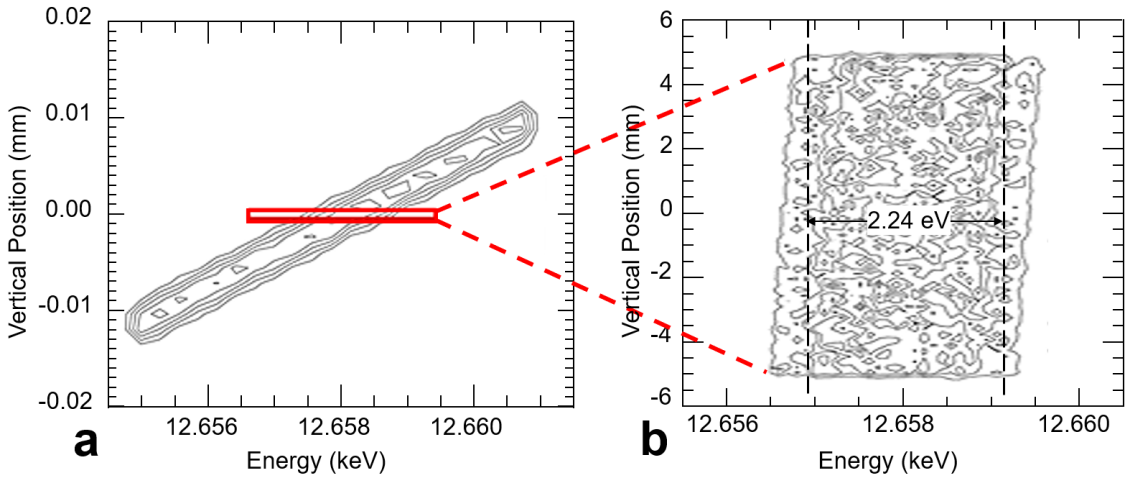

Figure 4.11: If we simulate a larger beam compared with Figure 4.10, we obtain the energy vs vertical beam location dependence as shown here (left). We then choose the rays within a 10 µm vertical window to show the energy resolution at each detector pixel.

The ray-tracing also shows that the peak at the detector has an energy width of 2.69 eV as shown in Figure 4.10. This value matches a simple calculation for the peak energy as a sum of the ΔE due to the Bragg planes rotation and lattice d-space compression (2.41 eV) and the energy contribution from the pinhole size (0.43 eV), for a total of 2.84 eV. The energy vs pinhole vertical sizes are shown in Figure 4.11. In Shadow's coordinate system the vertical beam position is inverted.

The comparison in Figure 4.7 demonstrates that our ray-tracing simulation is correct and hence the simulation for the energy resolution using our model should also be correct. We then simulated a larger beam (2 mm in the vertical direction) and from it we chose the beam in a 10 µm window, simulating the detector pixel size. The result is 2.24 eV as shown Figure 11. (Note: Darwin Widths of (1,1,1) and (2,2,0) at 12.67 keV are 20.4 and 15.1 µm, compared to the relative peak width for our bent (1,1,1) of 30.1 µm.)

4.4.3 Analysis method

At a specific x location, assume that each vertical line in the detector is a measurement of the number of photons transmitted through the object as a function of energy, $N(E_i)$, with an incident photon count to the object of, $N_0(E_i)$. The detector pixels along each vertical line will divide the energy range into n different energies values ($1 \leq i \leq n$). Also, assume that the object at that x location is composed of m different materials indexed by j, whose mass attenuation coefficients are $\left(\frac{\mu}{\rho}\right)_{ji} E_i$, densities of, ρ_j, and thicknesses of, t_j, for the selenium and matrix materials.

$$N(E_i) = N_0(E_i)\, e^{-\sum_{j=1}^{m} \left(\frac{\mu}{\rho}\right)_j (E_i) \rho_j t_j} \quad \text{or} \quad N_i = N_{0_i} e^{-\sum_{j=1}^{m} \left(\frac{\mu}{\rho}\right)_{ji} \rho_j t_j}. \tag{4.10}$$

The i index corresponds to the energy of photons detected across the vertical extent of the beam on the detector ($i = 1$ to n energies) and the j index in the exponent corresponds to the various materials

responsible for attenuating the transmitted beam through the object. The right side of Equation (4.10) is a short-hand version to simplify subsequent equations. The attenuation characteristics of the contrast and matrix materials ($\left(\frac{\mu}{\rho}\right)_{ji}$) can be measured, tabulated or modelled.

Equation (4.10) can be recast by taking a negative logarithm to give a set of n linear equations with m unknowns,

$$r_i = -\ln\left(\frac{N_i}{N_{0_i}}\right) = \sum_{j=1}^{m}\left(\frac{\mu}{\rho}\right)_{ji}\rho_j t_j, 1 \leq i \leq n. \tag{4.11}$$

Now we need to find the projected values ($\rho_j t_j$) that lead to the best fit to the measured values (r_i). A least-squared approach is used [49, 116] and results in

$$\begin{bmatrix} \rho_1 t_1 \\ \vdots \\ \rho_j t_j \\ \vdots \\ \rho_m t_m \end{bmatrix} = \begin{bmatrix} n\left(\frac{\mu}{\rho}\right)_{\langle 11\rangle} & \dots & n\left(\frac{\mu}{\rho}\right)_{\langle 1j\rangle} & \cdots & n\left(\frac{\mu}{\rho}\right)_{\langle 1m\rangle} \\ \vdots & & \vdots & & \vdots \\ n\left(\frac{\mu}{\rho}\right)_{\langle j1\rangle} & \dots & n\left(\frac{\mu}{\rho}\right)_{\langle jj\rangle} & \dots & n\left(\frac{\mu}{\rho}\right)_{\langle jm\rangle} \\ \vdots & & \vdots & & \vdots \\ n\left(\frac{\mu}{\rho}\right)_{\langle m1\rangle} & \dots & n\left(\frac{\mu}{\rho}\right)_{\langle mj\rangle} & \dots & n\left(\frac{\mu}{\rho}\right)_{\langle mm\rangle} \end{bmatrix}^{-1} \begin{bmatrix} \sum_i \left(\left(\frac{\mu}{\rho}\right)_{1i} r_i\right) \\ \vdots \\ \sum_i \left(\left(\frac{\mu}{\rho}\right)_{ji} r_i\right) \\ \vdots \\ \sum_i \left(\left(\frac{\mu}{\rho}\right)_{mi} r_i\right) \end{bmatrix}, \tag{4.12}$$

where

$$\frac{\mu}{\rho}_{\langle kl\rangle} \equiv \frac{1}{n}\sum_{i=1}^{n}\left[\left(\frac{\mu}{\rho}\right)_{ki}\left(\frac{\mu}{\rho}\right)_{li}\right] = \frac{\mu}{\rho}_{\langle kl\rangle}. \tag{4.13}$$

Thus, the task of determining the projected material values is reduced to determining the mass attenuation weighted values using the measured transmission values from Equation (4.11) and the inverse of the mass attenuation matrix in Equation (4.12). The components in that matrix are 'squares' of the mass attenuation coefficients averaged over the energy range of the measurements as defined in Equation (4.13). For simplicity, the inverse of the matrix will not be shown here but is easily evaluated numerically by computer.

4.4.4 Sample preparation

Sample holders for proof-of-principle experiments comprised 4 nylon tubes in circle, with a seedpod of *Astragalus bisulcatus* in the center. The bundle was then fixed in a disposable plastic liquid dropper to prevent unexpected sample position movement while we adjusted the stage. Every nylon tube was sealed on both ends to contain certain solution samples as described in the Result section. The sample holder for concentration sensitivity tests is a 3D printed cylinder with 8 hollows, designed with SketchUp. Pipette tips sealed on both ends are used as containers for solution samples and were placed in the hollows of the holder during experiment. Sample holders and containers are shown in Figure 4.12.

4.4.5 Data collection

All experiments were performed at the BMIT BM beamline at the Canadian Light Source (CLS) at the University of Saskatchewan. The imaging sample was placed at the focus and the prepared beam was then

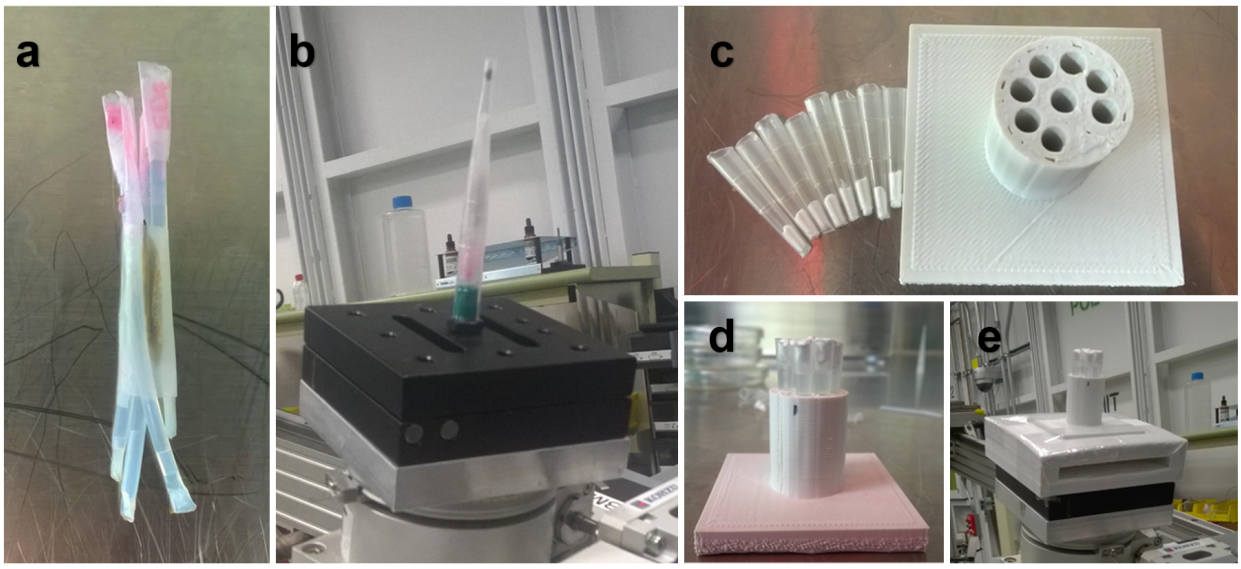

Figure 4.12: Samples and sample holders. (a) Solution samples in nylon tubes surrounding an Astragalus bisulcatus seedpod. (b) Nylon tubes and the seedpod fixed in a plastic liquid dropper on the imaging stage. (c) Top view of sample holder base and solution containers for concentration sensitivity tests. (d) Side view of sample holder for concentration sensitivity tests. (e) Sample holder for concentration sensitivity tests on the imaging stage.

transmitted through the sample into a high-resolution x-ray detector (Hamamatsu AA-60 with ORCA Flash 4.0, which has an effective pixel size of 13.6 µm), forming a 2-dimensional image with horizontal position in the sample along the x-axis and a range of energy along the y-axis. The distances are 22 m from synchrotron source to the bent crystal, 0.96 m from the bent crystal to the imaging sample, and 1.34 m from sample to the detector. Due to the high heat load on the crystal and the resulting distortion of its shape, the beam was allowed to stabilize for about 40 minutes for each sample before imaging. A water cooler to stabilize the temperature of the monochromator in shorter time length was designed and used for subsequent experiments. As a result, stabilization time was shortened to $10 \sim 15$ minutes.

The image produced in one projection represents the absorption spectrum of one horizontal position in the imaged sample. To produce 2-dimensional projection images, the samples were vertically scanned by moving the sample stage to capture a series of energy-spatial images, each representing a single vertical position in the sample. To produce CT slices, the samples were rotated through 180° with 900 energy-spatial images captured at regular intervals; the CT scan for one slice generally takes $12 \sim 14$ minutes.

Acknowledgements

Research described in this paper was performed at the Canadian Light Source, which is funded by the Canada Foundation for Innovation (CFI), the Natural Sciences and Engineering Research Council of Canada (NSERC), the National Research Council Canada, the Canadian Institutes of Health Research (CIHR), the Government of Saskatchewan, Western Economic Diversification Canada, and the University of Saskatchewan

(U of S). We acknowledge support from Canada Research Chairs (to G.N.G., I.J.P. and L.D.C.), NSERC (to G.N.G., I.J.P. and L.D.C.), CFI (to I.J.P.) and U of S. P.Q., N.S., M.M. and B.B. were Fellows and O.P. was an Associate in CIHR Training program in Health Research Using Synchrotron Techniques. We acknowledge George Belev and Adam Webb for beamline support.

Author Contributions

L.D.C., I.J.P., G.N.G. designed the project. P.Q., N.S., M.M. and B.B. performed most of the experiments. O.P. prepared the samples for most of the experiments. L.D.C. and P.Q. developed the algorithm and programs for data analysis and analyzed the data. A.G. measured energy resolution of the dispersive beam. L.D.C. and P.Q. wrote the manuscript. I.J.P. and G.N.G. revised the manuscript. All authors read and approved the paper.

Competing Interests

The authors declare no competing interests.

Additional Information

Correspondence and requests for materials should be addressed to L.D.C.

Chapter 5

New Insights into the Focusing and Energy Dispersion Properties of Bent Laue Crystals

Publication status The content of this chapter is a manuscript to be submitted to *Optica* for publication as an article. Minor modifications may be made to the manuscript before publication.

Author contribution The author of the thesis proposed and developed the concept of this paper, derived the equations and wrote the major part of the paper with the advice and guidance of Prof. Chapman. All co-authurs helped in revision of the math derivations and text content. Inspirations from discussions among all co-authors are unquantifiable contributions and should be acknowledged.

Preface For energy dispersive x-ray imaging techniques, the energy resolution of the system is a critical factor in analyzing the fine structures of x-ray absorption spectra. The magic condition provides energy resolution that is good enough to accomplish x-ray absorption spectroscopy studies but not as good as typical double flat crystal monochromators. To investigate the mechanism for energy resolution improvement, efforts have been made to better understand bent Laue crystal optics.

The present work in this chapter describes a new approach for interpreting bent Laue diffraction from a ray-tracing point of view. This new quasi-mono beam approach explains energy and spatial properties of bent Laue optics, predicts phenomena that can improve energy dispersion related x-ray imaging techniques and provides a powerful tool for easier realization of ray-tracing simulations for bent Laue monochromators. It suggests ways to improve the developed imaging system of the thesis project and also brings insights for the improvement and design of synchrotron x-ray beamlines.

This paper addresses Objective IV to lay the groundwork for a deeper understanding of the energy properties to support possible future improvements in systems of this type.

Note The work presented in Chapter 2 is the basis of the theory developed in Chapter 5. However, due to the extension of the theory, some symbols and variables in Chapter 5 have to be defined differently from Chapter 2. These symbols and variables are listed below.

- X-ray source distance: f_1 in Chapter 2; p in Chapter 5.
- Geometric focus: f_{2g} in Chapter 2; q_G in Chapter 5.

- Single-ray focus: f_{2s} in Chapter 2; q_S in Chapter 5.
- Angle ϕ: The angle between the x-ray diffraction direction and the crystal surface normal in Chapter 2; the directional angle from the x-ray incident direction to the crystal surface normal in Chapter 5.

New Insights into the Focusing and Energy Dispersion Properties of Bent Laue Crystals

Peng Qi,[1] Xianbo Shi,[2] Nazanin Samadi,[3] and L. Dean Chapman[4]

[1]Division of Biomedical Engineering, University of Saskatchewan, Saskatoon, Canada

[2]Advanced Photon Source, Argonne National Laboratory, Lemont, Illinois, USA

[3]Swiss Light Source, Paul Scherrer Institut, 5232 Villigen, Switzerland

[4]Anatomy, Physiology & Pharmacology, University of Saskatchewan, Saskatoon, Canada

Abstract

X-ray Laue type monochromators are common and essential optical components in many high-power x-ray facilities, e.g., synchrotron facilities. The x-ray optics of bent Laue crystals is a well developed area. However, there is difficulty of understanding when considering the multiplicity of diffracted beams with different angles and energies resulted from single polychromatic rays penetrating the crystal. There is a need for a way to organize the rays that allows one to sort out the energy and the spatial properties of the diffracted beam.

In the presented work, we introduce a new approach for describing the general behavior of bent Laue crystals from a ray-tracing point of view. The so-called quasi-mono beam approach provides an intuitive view of bent crystal diffraction and leads to deeper understandings. It explains energy and spatial properties of common and special cases of bent Laue optics, predicts phenomena that can improve energy dispersion related x-ray imaging techniques and provides a theory framework that makes ray-tracing simulation easier to realize.

5.1 Introduction

X-ray Laue or transmission type monochromators have been used for many types of applications, especially in high x-ray energy applications where the Laue geometry is better at handling high incident powers that are generated by synchrotron or other high-power x-ray sources. The description of bent Laue crystal optics is a well developed area. The difficulty of understanding the behavior of bent Laue crystal is that a single incoming polychromatic ray gives rise to a multiplicity of diffracted beams all with different angles and energies. The situation is further complicated when several incoming beams intercept the crystal. Though the energy and trajectory of these rays are predictable, understanding the focusing and the energy dispersive properties of the diffracted beams is hindered by accounting for all of these rays. What is needed is a way to organize the rays that allows one to sort out the energy and the spatial properties of the diffracted beam.

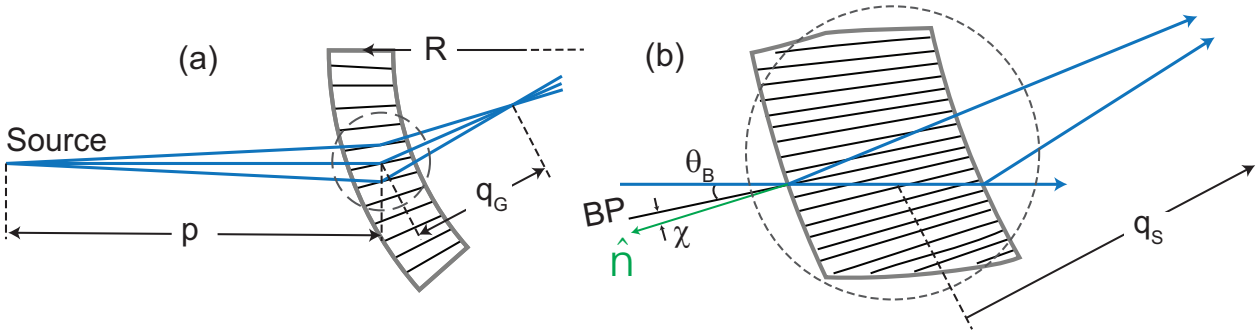

Figure 5.1: Bent asymmetric Laue focusing. (a) The geometric focusing with the source at a distance p, the bent Laue crystal with radius R, asymmetry angle χ, Bragg angle θ_B and focal distance q_G. (b) A chosen relationship between the incident ray in relation to the Bragg planes (BP), the crystal surface normal vector ($\hat{n}$) and the asymmetry angle χ. The geometry shown results in the single-ray focus at a distance q_S.

In the presented work, a general description of bent Laue optics is introduced that (i) explains the path of diffracted x-rays, the focusing properties and the energy properties in simple geometrical terms, and (ii) predicts a new phenomenon of monochromatic focusing which may enable new bent Laue energy dispersive applications or improving the existing ones.

This new approach is best understood from the so-called 'magic condition' [44, 115] that allows bent Laue crystals to provide a small focal size and good energy resolution simultaneously which is described in detail in the next section.

5.2 Background

Often, elastic bending of crystals is desired to focus or increase the energy dispersion of the diffracted x-ray beams. The diffraction properties of elastically bent Laue crystals can be described by wave theories [81, 51, 40] and lamella models [82]. For the discussion that follows, the crystals will be elastically bent single crystals such as silicon.

Earlier works [46, 47] have shown the focal size of an asymmetric bent Laue monochromator can be minimized by coinciding the geometric focus and the single-ray focus with a carefully chosen asymmetry angle. Later, some works have reported that at this condition the angle-energy dispersion of the diffracted polychromatic beam is also improved in addition to the focal size minimization [49]. Novel imaging techniques [49, 44, 67, 68] have been developed to take advantage of this 'magic condition'.

However, the mechanism of the energy properties of the magic condition is unclear. The coinciding of geometric focus and single-ray focus guides the way to the magic condition, but leaves its optical attributes unknown. The presented work unveils the magic condition optics from the perspective of diffraction angles at representative locations in the crystal, and provides a new way of studying bent Laue monochromators which makes ray-tracing easier to realize.

5.3 Magic Condition

5.3.1 Concept

As demonstrated in Figure 5.2, the coinciding state of geometric focus and single-ray focus is directly related to the equality of Bragg angles at point A and B because of the Bragg's law [31], where B is the location the diffracted x-rays from point A exit the crystal. Assuming the incident x-ray beam is parallel, when the two Bragg angles are equal to each other, the travel path of the x-rays diffracted from A and B coincide, which makes the geometric focus and single-ray focus coincide in consequence. Therefore, the determining condition can be transformed from coinciding the two foci to assimilating the two Bragg angles. It can be also seen that, when the angle condition is met, the plane α and β behave like they are stitched together and form a larger Bragg plane as shown in Figure 5.3. The diffracted x-rays from the two planes become continuously energy dispersive as if diffracted from one plane. The diffraction angles are the same not only at point A and B, but at every point on the path from A to B. Because when the magic condition is met, the crystal thickness is not present in the magic condition equation (Equation (5.10) in section 5.3.3).

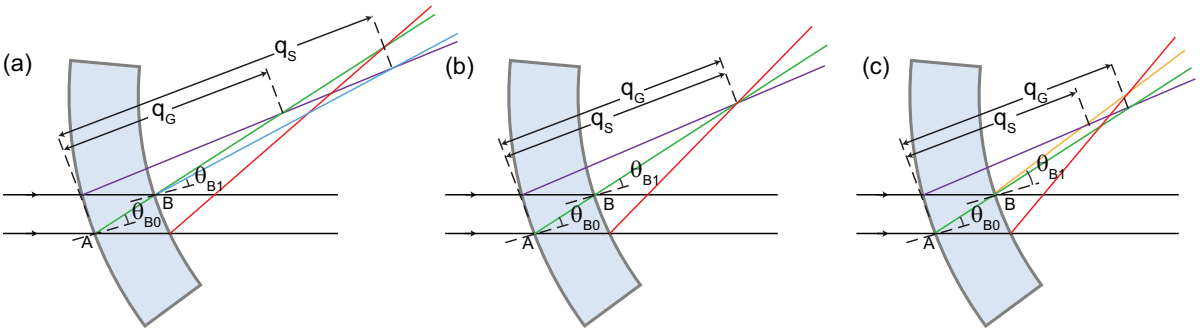

Figure 5.2: Geometric foucs, single-ray focus and Bragg angles when magic condition is met or not met. (a) Geometric focus is less than single-ray focus, Bragg angle at B is smaller than Brgg angle at A; (b) Geometric focus equals single-ray focus, Bragg angle at B equals Bragg angle at A (the magic condition); (c) Geometric focus is greater than single-ray focus, Bragg angle at B is larger than Bragg angle at A.

5.3.2 Magic condition with infinite source distance

When the magic condition is met, x-rays diffracted at point A and B travel on the same path. This can be directly translated to $\theta_{B0} = \theta_{B1}$ when the source distance is infinite, where the subscripts $_0$ and $_1$ correlate to points A and B, as shown in Figure 5.3. In general, the diffraction angle θ_B can be described by χ and ϕ,

$$\theta_B = \phi - \chi, \tag{5.1}$$

where ϕ is the directional angle from the x-ray incident direction to the crystal surface normal and χ (the asymmetry angle) is the directional angle from the diffraction lattice to the surface normal. (The angle ϕ

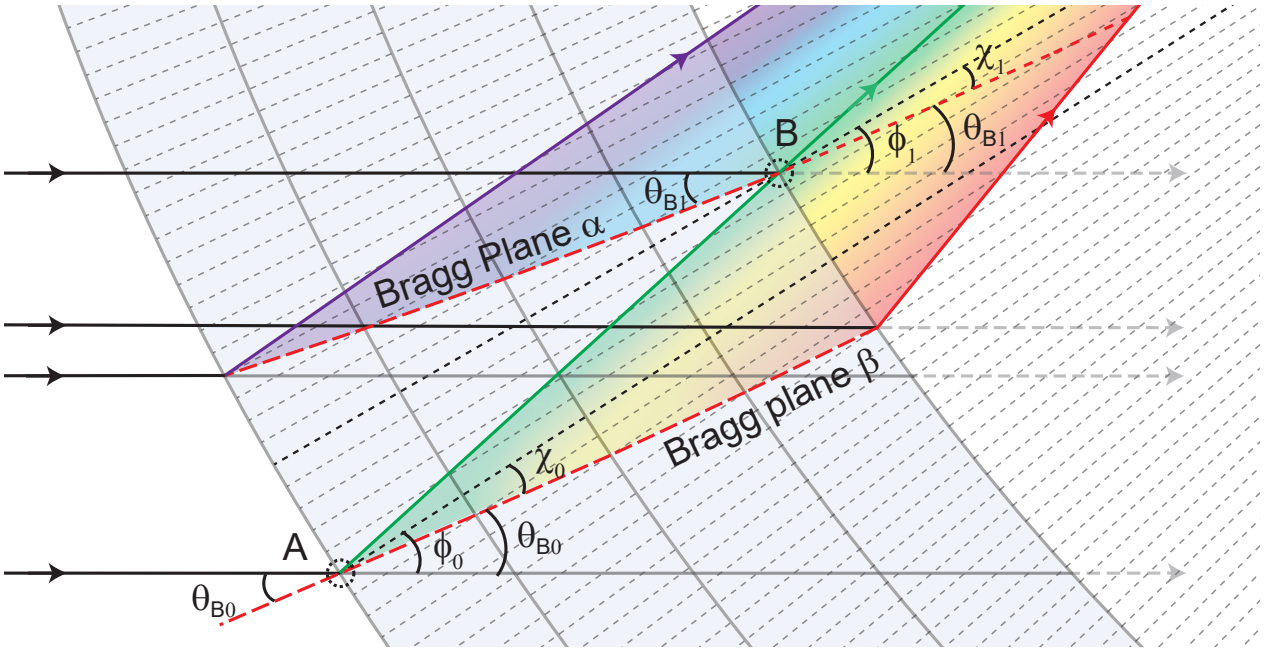

Figure 5.3: Magic condition concept geometry for infinite distant source.

is not a direct parameter for describing the crystal but is helpful for simplifying the discussion hereinafter.) The magic condition can then be described as the changes of χ and ϕ summing to zero.

$$\theta_{B1} - \theta_{B0} = (\phi_1 - \phi_0) - (\chi_1 - \chi_0) = \Delta\phi - \Delta\chi = 0. \tag{5.2}$$

The change of χ is caused by the deformation of the bent crystal. As shown in Figure 5.3, the concave (convex) side of the crystal is compressed (expanded) in one dimension which results in elastic expansion (compression) in the two transverse dimensions. The change of χ is given by

$$\Delta\chi = -\frac{1+\nu}{2}\frac{T}{R}\sin 2\chi. \tag{5.3}$$

(See Appendix B.1 for detailed derivation.)

The change of ϕ can be determined from the magic condition geometry, and is given by

$$\Delta\phi_\infty = -\frac{T}{R}\tan(\theta_B - \chi), \tag{5.4}$$

where the subscript $_\infty$ indicates the infinite source distance scenario. $\Delta\phi$ in general will be given in section 5.3.3 (see Appendix B.1 for detailed derivation).

Therefore, the magic condition equation when the source distance is infinite is given by

$$\Delta\phi_\infty - \Delta\chi = \frac{1+\nu}{2}\frac{T}{R}\sin 2\chi - \frac{T}{R}\tan(\theta_B - \chi) = 0. \tag{5.5}$$

5.3.3 Magic condition with finite source distance

When the source distance is finite, the diffracted x-rays exiting in the same path to the common focus are diffracted by slightly different Bragg angles. The variation of Bragg angles between point A and B (Figure 5.4)

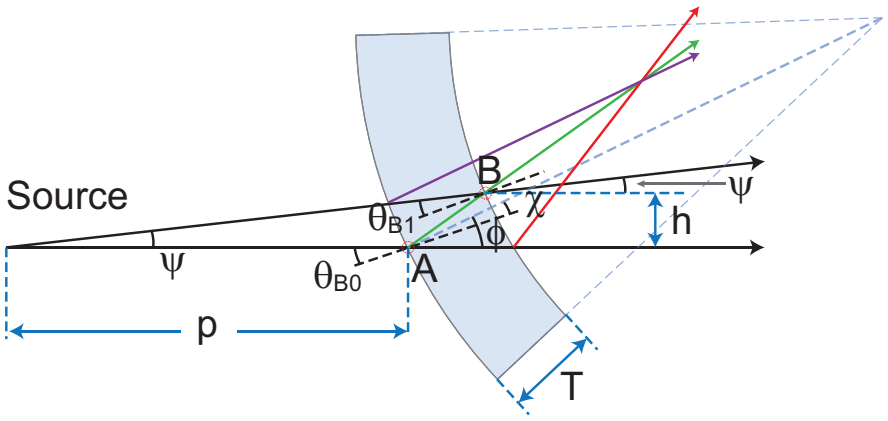

Figure 5.4: Magic condition with finite source distance

is

$$\Delta\theta_{B_{01}} = -\frac{1}{2}\psi, \tag{5.6}$$

where ψ is the angle from x-rays diffracted at point A to the x-rays diffracted at point B, given by

$$\psi = \frac{T}{p}\frac{\sin(2\theta_B)}{\cos(\chi - \theta_B)}, \tag{5.7}$$

where p is the x-ray source distance (see Appendix B.2.1 for the derivation of Equation (5.7)).

The $\Delta\phi$ should be adjusted from the $\Delta\phi_\infty$ with

$$\Delta\phi = \Delta\phi_\infty - \psi. \tag{5.8}$$

The magic condition concept equation considering the source distance is

$$\Delta\theta_{B_{01}} = \Delta\phi - \Delta\chi = (\Delta\phi_\infty - \psi) - \Delta\chi, \tag{5.9}$$

or

$$\frac{1+\nu}{2}\frac{T}{R}\sin 2\chi - \frac{T}{R}\tan(\theta_B - \chi) - \frac{1}{2}\frac{T}{p}\frac{\sin 2\theta_B}{\cos(\chi - \theta_B)} = 0. \tag{5.10}$$

Note that R or p can be either positive or negative. A positive R corresponds to the convex side of the crystal facing the source, and a negative R corresponds to the concave side of the crystal facing the source. A positive p corresponds to a finite source distance or a diverging incident beam, and a negative p corresponds to a 'beyond-infinite' source distance or a converging incident beam. When the source distance is infinite, Equation (5.10) is equivalent to Equation (5.5).

When the magic condition is not met, the residual, $\Delta\theta_{B_{\text{mis}}}$, of Equation (5.10) is the misalignment of the Bragg angles from matching the magic condition. The misalignment angle is given by

$$\Delta\theta_{B_{\text{mis}}} = \Delta\phi_\infty - \Delta\chi - \frac{\psi}{2}. \tag{5.11}$$

5.3.4 Equivalency to the other magic condition apporach

In previously published studies [49, 44], a different method has been used to approach the magic condition. The matching of geometric focus, q_G, and single-ray focus, q_S, is used as the determinate condition (the focus-matching approach). The geometric focus is defined by [47]

$$\frac{\cos(\chi-\theta_B)}{q_G}-\frac{\cos(\chi+\theta_B)}{p}=\frac{2}{R}, \tag{5.12}$$

and the single-ray focus is defined by [44]

$$q_S=\frac{R\sin 2\theta_B}{2\sin(\chi+\theta_B)+(1+\nu)\sin 2\chi\cos(\chi+\theta_B)}. \tag{5.13}$$

Note that, in the cited works [47, 44], sign conventions are used to treat for different diffraction scenarios. With the definition of variables in the presented work, Equations (5.12) and (5.13) can be generalized to all scenarios and, thus, the sign convention is not needed. By combining the two equations with $q_S = q_G$ and rearranging it, the magic condition can be described as

$$\frac{R}{2p}\frac{\sin 2\theta_B}{\cos(\chi-\theta_B)}-\frac{1+\nu}{2}\sin 2\chi+\frac{\sin 2\theta_B}{\cos(\chi+\theta_B)\cos(\chi-\theta_B)}-\tan(\chi+\theta_B)=0. \tag{5.14}$$

Rearranging the previous magic condition equation (Equation (5.10)), we have

$$\frac{R}{2p}\frac{\sin 2\theta_B}{\cos(\chi-\theta_B)}-\frac{1+\nu}{2}\sin 2\chi+\tan(\theta_B-\chi)=0. \tag{5.15}$$

By comparing Equation (5.14) and Equation (5.15), the first two terms in the two equations are identical, respectively. And it is not hard to get

$$\frac{\sin 2\theta_B}{\cos(\chi+\theta_B)\cos(\chi-\theta_B)}-\tan(\chi+\theta_B)=\tan(\theta_B-\chi). \tag{5.16}$$

Thus, Equation (5.14) and Equation (5.15) are equivalent mathematically. The angle-matching approach proposed in this work and the focus-matching approach are describing the same optical phenomenon from different perspectives and are supportive to the correctness of each other. However, the focus-matching approach explains only the focal size minimization and does not reveal the energy properties of the magic condition intuitively. The angle perspective to the magic condition explicitly describes energy related properties, forms a deeper understanding and enables more opportunities for the improvement of bent Laue crystal related applications. This is discussed with more details in section 5.5.

5.4 Energy Resolution of a Magic Condition Monochromator

X-rays diffracted by a magic condition monochromator is sorted by angle and form a perfect fan beam. However, x-rays diffracted at the same Bragg angle are not purely monochromatic, but contain x-rays with a range of energies, thus determine the energy resolution of the magic condition monochromator. This section will discuss the individual contributions to the energy resolutions, the integration of the individual contributions, and the ultimate energy resolution that is achievable under special condition.

5.4.1 Contributions to the energy resolution

Firstly, the lattice spacing of the crystal is not uniform because of the crystal bending deformation. Those diffracted x-rays exiting the crystal at the same point travel on the same path, but the d-spacing variation creates energy spread in those x-rays and the contribution can be described in the following equation

$$\frac{\Delta E}{E}_1 = -\frac{\Delta d}{d} = \frac{T}{R}(\cos^2\chi - \nu\sin^2\chi). \tag{5.17}$$

Secondly, the x-ray source is at a finite distance. Thus, the incident angles of the x-rays vary when they hit the crystal at different locations in the diffraction plane. The source-to-crystal distance contribution to the energy spread can be described in the following equation.

$$\frac{\Delta E}{E}_2 = -\frac{\Delta\theta_{B_{01}}}{\tan\theta_B} = \frac{T}{p}\frac{\cos^2\theta_B}{\cos(\chi-\theta_B)}. \tag{5.18}$$

Thirdly, the intrinsic Darwin width is the fundamental contribution to the energy spread in a monochromatic x-ray. The contribution of the Darwin width can be described by

$$\frac{\Delta E}{E}_3 = \frac{w_D}{\tan\theta_B}, \tag{5.19}$$

where w_D is the Darwin width and is a constant value for a given reflection lattice [30].

Fourthly, the source size is not infinitely small. Its contribution to the energy resolution is

$$\frac{\Delta E}{E}_4 = \frac{S}{p\tan\theta_B}, \tag{5.20}$$

where S is the size of the source transverse to the median ray in the diffraction plane.

In addition, the detector spatial resolution is also a factor for the overall energy resolution. Smaller pixel size of the detector may give better energy resolution. Detector considerations are out of scope of the discussion for the monochromator here.

5.4.2 Integration of all contributions

The first two contributions ($\frac{\Delta E}{E}_1$ and $\frac{\Delta E}{E}_2$) to the energy resolution are directional. For the geometry in Figure 5.4, because of the Bragg's law, the lattice spacing compression at point B results in a higher energy than point A for parallel incident x-rays. In the meantime, the x-rays incident at point B with a shallower angle than point A, which also corresponds to a higher energy for x-rays diffracted at point B. And it is not hard to derive that the energy divergence between point A and B are the sum of the two terms and their values should be dealt with signs. Therefore, the combined contributions of the first two terms to the energy resolution is

$$\frac{\Delta E}{E}_{1\&2} = \frac{\Delta E}{E}_1 + \frac{\Delta E}{E}_2. \tag{5.21}$$

The interaction of these two contributions in different scenarios are explained in Appendix B.3.

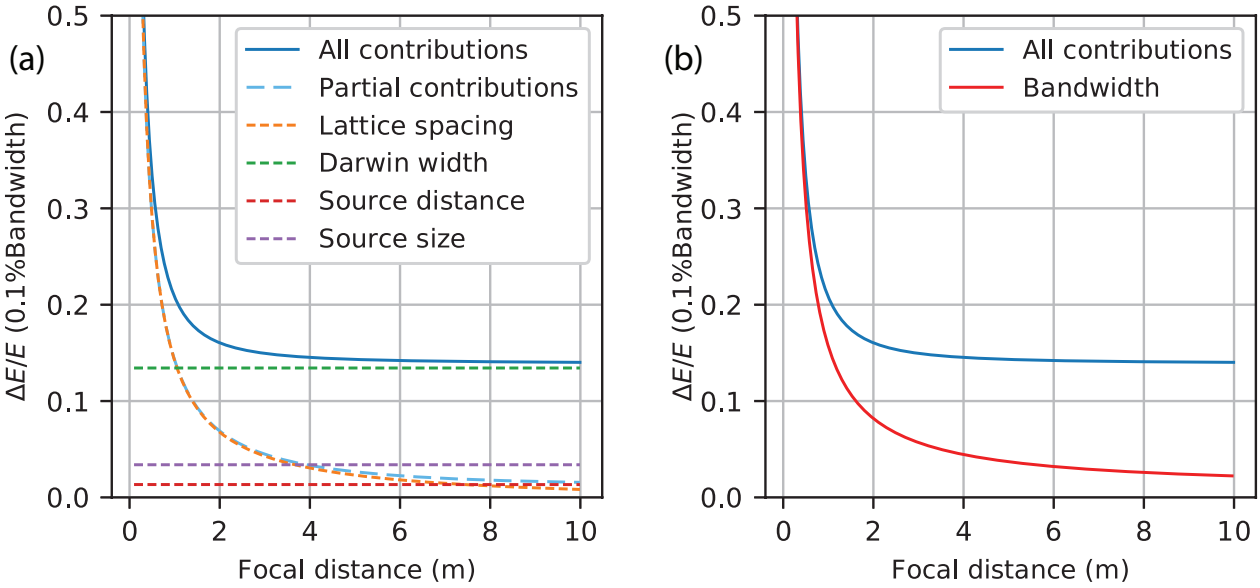

Figure 5.5: Energy resolution of a magic condition monochromator in a range of focal distance, with Si(111) reflection, 0.3 mm crystal thickness, 22 m source distance, 0.2 Poisson's ratio and center energy at 12.658 keV. (a) Total energy resolution and individual contributions. (b) Total energy resolution and the relative bandwidth.

Assuming the source size is Gaussian distributed, and is uncorrelated to the angular distribution, then the third and fourth contributions will add in quadrature with other contributions. The overall energy resolution from all contributions should be put together in the following way

$$\frac{\Delta E}{E} = \sqrt{\left(\frac{\Delta E}{E}_1 + \frac{\Delta E}{E}_2\right)^2 + \left(\frac{\Delta E}{E}_3\right)^2 + \left(\frac{\Delta E}{E}_4\right)^2}.$$

The simulated energy resolution for the magic condition geometry is shown in Figure 5.5 (focal distance is restrained for up to 10 m). The lattice spacing contribution is dominant when the focal distance is relatively close, as the crystal bending radius is small and caused more deformation of the crystal. Darwin width contribution is constant for a given reflection and is the dominant term when the focal distance is relatively large as the crystal deformation is not significant. The source size and distance contribution is usually small for a synchrotron x-ray source. The combined contributions of the two directional terms (lattice spacing and source distance) is dominated by lattice spacing in the shown range of focal distance. Larger focal distance corresponds to smaller bandwidth of the monochromator as the crystal bending radius is larger.

5.4.3 The ultimate energy resolution magic condition

Depending on the signs of R and p, it is obvious that the $\frac{\Delta E}{E}_1$ and $\frac{\Delta E}{E}_2$ can be either supplemental or subtractive to each other. When R and p are both positive (or both negative), $\frac{\Delta E}{E}_1$ and $\frac{\Delta E}{E}_2$ are supplemental to each other; and vice versa. When $\frac{\Delta E}{E}_{1\&2} = 0$, the energy blurring from $\frac{\Delta E}{E}_1$ and $\frac{\Delta E}{E}_2$ can be eliminated. With Equation (5.17), Equation (5.18) and Equation (5.21), this condition is met when

$$\frac{R}{p} = -\frac{2(\cos^2\chi - \nu\sin^2\chi)\cos(\chi - \theta_B)}{\cos^2\theta_B}. \tag{5.22}$$

When the magic condition equation (Equation (5.10)) and the ultimate resolution equation (Equation (5.22)) are both true, the energy resolution of a magic condition monochromator is only limited by the intrinsic Darwin width and the source size. For example, a pair of χ and R can be obtained by solving Equation (5.10) and Equation (5.22) simultaneously for a given energy of interest and the rest parameters.

For high energy applications, Equation (5.22) requires the bending radius of the crystal to be about twice the source distance (the negative sign suggests the source and the center of the crystal bending circle are on the same side of the crystal). While this ultimate energy resolution magic condition is impractical to achieve for single crystal systems in synchrotron x-ray beamlines, it could be near the second crystal of a beam expander [44] or some other multiple crystal systems.

For example, with a 22.0 m source distance and Si(111) type reflection, the ultimate resolution magic condition for 12.658 keV x-ray is met when χ is -4.0° and R is -43.7 m; with a 1.0 m source distance and other parameters being the same, the magic condition is met when χ is -4.0° and R is -2.0 m.

5.5 Quasi-Monochromatic Beam for Off-Magic Condition

5.5.1 Concept

When the crystal does not match the magic condition, diffracted x-rays exiting at point B no longer propagate on the same path but form a fan beam with a deviation angle, as shown in Figure 5.6. This deviation angle, Θ, is resulted by the misalignment of diffraction angles θ_{B0} and θ_{B1} at points A and B, respectively,

$$\begin{aligned}\Theta &= 2\theta_{B\text{mis}} \\ &= T\left[\frac{1+\nu}{R}\sin 2\chi - \frac{2}{R}\tan(\theta_B - \chi) - \frac{1}{p}\frac{\sin 2\theta_B}{\cos(\chi - \theta_B)}\right].\end{aligned} \tag{5.23}$$

Figure 5.6 shows the scenario that θ_{B1} is smaller than the magic condition diffraction angle, hence the deviation angle is below the reference ray, $\overrightarrow{AA'}$. If travelling from point B downwards along the crystal surface, the diffraction angle gets larger and larger, and eventually a point C can be found where θ_{B2}, the diffraction angle at point C, equals the magic condition diffraction angle and the diffracted rays are parallel to the reference ray. Again, when the source is infinitely far away, $\theta_{B2} = \theta_{B0}$; otherwise, θ_{B0} and θ_{B2} are different by a correction for the finite source distance.

Therefore, no matter the magic condition is met or not, there are always a series of diffracted x-rays parallel to the diffracted reference x-ray. The magic condition is a special case when all these parallel rays travel on the same path and exit the crystal at the same location; when the magic condition is not met, these parallel rays do not travel on the same path but exit the crystal at a series of continuous locations on the crystal surface and form a parallel beam (between $\overrightarrow{AA'}$ and $\overrightarrow{CC'}$ in Figure 5.6) with a width not equal to

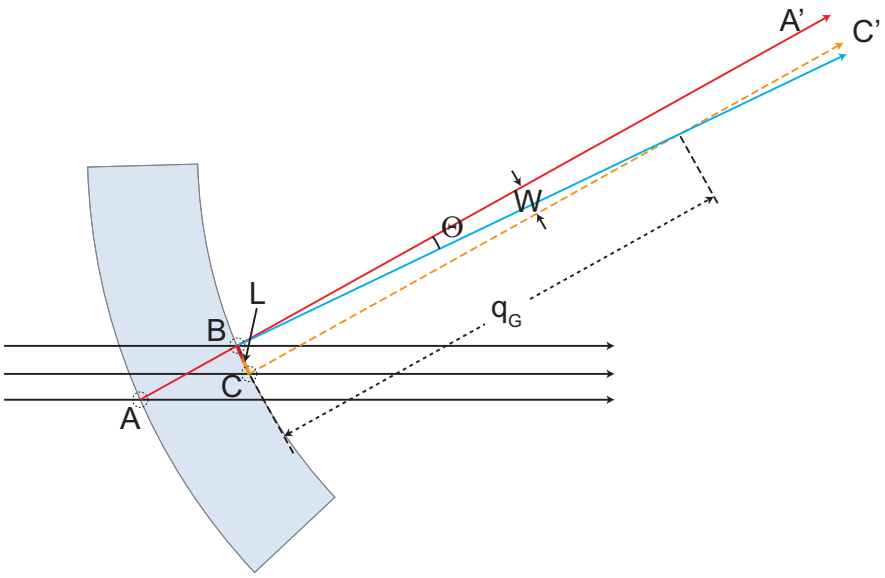

Figure 5.6: Geometry for quasi-mono beam width calculation

zero. The term *quasi-monochromatic beam* or *quasi-mono beam* is used to represent this beam parallel to the diffracted reference ray. The phrase 'quasi' is used because 'monochromatic' is only true for this beam when the lattice spacing variation, source distance, source size and crystal intrinsic Darwin width are neglected.

Not only the reference ray, but every incident ray that is diffracted at the surface of the crystal is accompanied by a quasi-mono beam when it leaves the crystal. The entire diffracted beam can be treated as a group of rays diffracted at the surface and their companion quasi-mono beams. The quasi-mono beam is a useful concept for interpreting the bent Laue crystal optics in terms of its focusing geometry and energy property.

In the following, both infinite and finite source distance versions of relevant parameters are given. The infinite version helps to understand the bulk of the behaviour as, in most instances, the source to crystal distance is large.

Quasi-mono beam width (QMBW)

For a source infinitely far away, the arc length L between point B and C corresponds to the diffraction angle divergence that amounts to half of the deviation angle, Θ. For a finite source distance, the x-ray incident angles at point B and C are different. Alternatively, an easy way to find point C is to draw a straight line parallel to the reference ray and through the geometric focus (caused by the downstream surface of the crystal to be accurate). Hence, the two edges of the quasi-mono beam is defined by the diffracted x-rays at point A and C, or $\overrightarrow{AA'}$ and $\overrightarrow{CC'}$.

The width of the quasi-mono beam is given by

$$\begin{aligned} W &= -q_{G_1}\Theta \\ &\approx -q_{G_0}\Theta \\ &= -\frac{T}{\frac{2p}{R}+\cos\left(\chi_0+\theta_B\right)}\left[(1+\nu)\frac{p}{R}\sin 2\chi_0\cos\left(\chi_0-\theta_B\right)+\frac{2p}{R}\sin\left(\chi_0-\theta_B\right)-\sin 2\theta\right], \end{aligned} \tag{5.24}$$

where q_{G_0} and q_{G_1} are geometric focus corresponds to the upstream and downstream crystal surface, respectively; and χ_0 is the effective asymmetry angle at point A, which is equivalent to χ hereinafter. The negative sign in the equation above is used to define counter clockwise rotation as positive relative to the focal point.

With the source distance at infinity, the width of the quasi-mono beam, W_∞, is given by

$$W_\infty \approx T\left[\frac{1+\nu}{2}\sin 2\chi_0\cos(\theta_{B0}-\chi_0)+\sin(\theta_{B0}-\chi_0)\right]. \tag{5.25}$$

For a symmetric bent Laue crystal with infinite source distance, the width of the quasi-mono beam, W_∞^{sym}, is given by

$$W_\infty^{\mathrm{sym}} = T\sin\theta_{B0}. \tag{5.26}$$

The arc length of the quasi-mono beam footprint on the downstream side of the crystal is given by

$$\begin{aligned} L &= \frac{W}{\cos(\theta_{B2}-\chi_2)} \\ &\approx \frac{W}{\cos(\theta_{B0}-\chi_0)}, \end{aligned} \tag{5.27}$$

where the subscripts $_0$ and $_2$ refer to variables corresponding to the points A and C in Figure 5.6, respectively.

With the source distance at infinity, the arc length of the quasi-mono beam footprint on the downstream side of the crystal, L_∞, is given by

$$L_\infty \approx T\left[\frac{1+\nu}{2}\sin 2\chi_0+\tan(\theta_{B0}-\chi_0)\right]. \tag{5.28}$$

For a symmetric bent Laue crystal with infinite source distance, the arc length of the footprint, L_∞^{sym} is given by

$$L_\infty^{\mathrm{sym}} = T\tan\theta_{B0}. \tag{5.29}$$

5.5.2 Focal size

Because the quasi-mono beam width is constant all the way from the monochromator to the detector, it is not hard to see that the focal size of a bent asymmetric Laue crystal for x-rays from a point source is the same size of the QMBW. When the finite source size, S, is considered, the total focal size is given by

$$S_f = \sqrt{\left(\frac{q_G S}{p}\right)^2+\frac{W^2}{12}}, \tag{5.30}$$

where the source is treated as a Gaussian distribution and the quasi-mono beam is treated as a uniform distribution where the variance has been used to represent its effective Gaussian width.

Another approach to calculate the focal size is using the single-ray focal distance and the geometric focal distance - a two-foci approach (see Appendix B.4). The focal sizes calculated using Equation (5.30) and the two foci approach for a point source and a range of asymmetry angles are compared (Figure 5.7). The results of each show excellent agreement with each other, which supports the quasi-mono beam description.

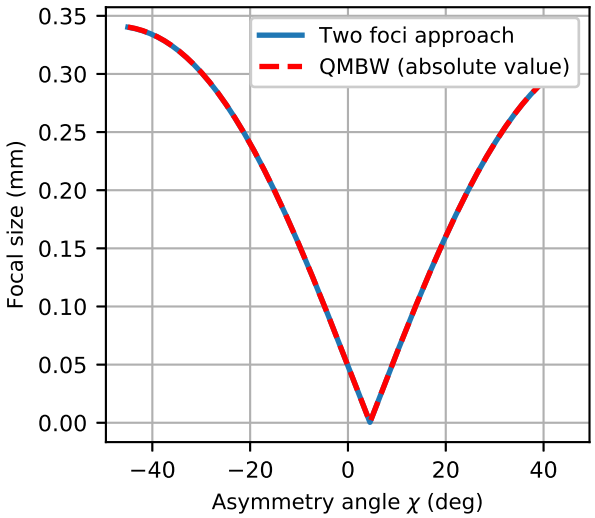

Figure 5.7: Calculated focal size against a range of asymmetry angle with two approaches: the foci distance geometry and the quasi-mono beam. The calculation was done for 0.3 mm thick Si(111), 12.658 keV, 22 m source distance and 2 m crystal bending radius.

5.5.3 Energy spread

The energy spread in the quasi-mono beam is similar to the energy resolution of the magic condition reference ray. The intrinsic Darwin width of the crystal and the size of the source blurs the energy resolution of every ray. The energy spreads caused by the lattice spacing variation and the source distance are directional. The combination of the latter two makes the energy of the quasi-mono beam lower on one side and higher on the other side.

The angular energy spread caused by the lattice spacing variation is

$$\Delta\theta_{Q1} = \frac{\Delta d}{d}\tan\theta_{B0} = -\frac{T}{R}(\cos^2\chi_0 - \nu\sin^2\chi_0)\tan\theta_{B0}. \tag{5.31}$$

(See Appendix B.5)

The angular energy spread caused by the finite source distance is

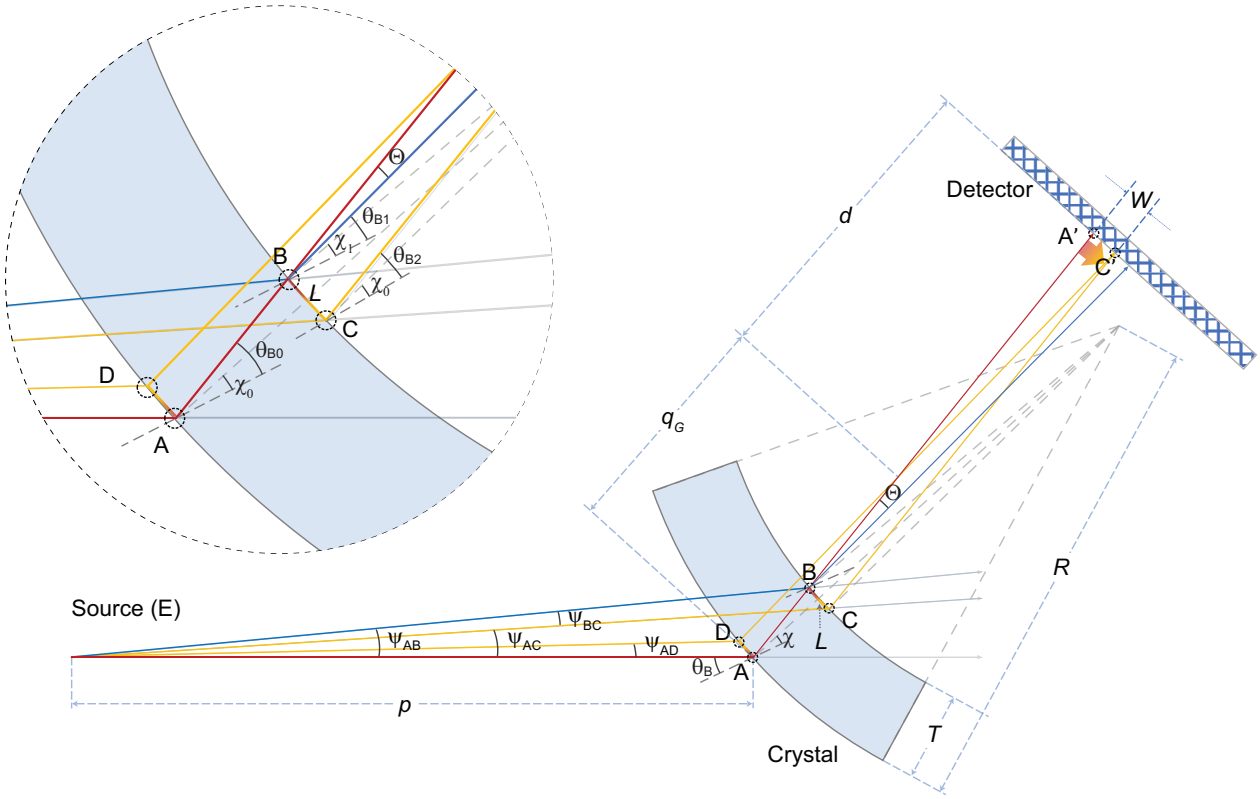

Figure 5.8: Quasi-mono beam geometry

$$\begin{aligned}\Delta\theta_{Q2} &= -\frac{1}{2}\left[\frac{T\sin 2\theta_{B0}}{p\cos(\chi_0-\theta_{B0})} - \frac{L\cos(\chi_2+\theta_{B2})}{p}\right] \\ &\approx -\frac{1}{2}\left[\frac{T\sin 2\theta_{B0}}{p\cos(\chi_0-\theta_{B0})} - \frac{L\cos(\chi_0+\theta_{B0})}{p}\right].\end{aligned} \tag{5.32}$$

(See Appendix B.5)

The total directional energy spread is simply given by

$$\Delta\theta_Q = \Delta\theta_{Q1} + \Delta\theta_{Q2}, \tag{5.33}$$

relative to the reference edge ($\overrightarrow{AA'}$ in Figure 5.8) of the quasi-mono beam.

5.5.4 Optimal detector distance

When the detector is placed at a special distance, energy resolution widening caused by lattice spacing deformation and finite source distance can be neutralized by the crystal surface curvature oriented energy dispersion. The only remaining contributors to the energy resolution widening will be the crystal intrinsic Darwin width and the source size. This is valuable because not only the energy resolution is improved significantly, but also the remaining two contributors are constants to a monochromator itself. This means a

crystal can be bent as much as possible for a larger bandwidth without compromising on the energy resolution. This optimal detector distance is explained in details below.

As mentioned in section 5.5.1, the total diffracted beam can be treated as x-rays diffracted by the lattices at the surface of the crystal (Surface Diffracted X-rays) and their companion quasi-mono beams. Because of the curvature of the crystal surface, the Surface Diffracted X-rays become an energy dispersive fan beam with an angle-energy correlation and thereby a position-energy correlation when the fan beam hit a position sensitive detector. In the example geometry shown in Figure 5.8, upper positions on the detector correlates to lower x-ray energies, and vice versa.

The actual energy spread direction of the quasi-mono beam on the detector depends on the beam position and the energy spread direction relative to the reference edge of the quasi-mono beam. It can be either the same direction or the opposite to the direction of the Surface Diffracted X-rays energy spread, which means the quasi-mono beam can either degrade or improve the energy resolution comparing to a magic condition monochromator, since the magic condition geometry compresses all this energy spread into a zero width quasi-mono beam. And it is obvious that the ultimate improvement arises if the energy spread of the quasi-mono beam matches that of the Surface Diffracted X-rays perfectly on the detector.

While the quasi-mono beam is unchanged on its way to the detector, the energy range per width of the fan beam changes as it propagates. When the detector is placed at a special distance (d in Figure 5.8), the energy spreads of the two can be aligned with each other perfectly. A 'monochromatic focus' (the intersection point of the yellow lines in Figure 5.8) is formed at this distance. X-rays arrive at the same pixel on the detector will have the same energy.

The optimal focus-to-detector distance is given by

$$d = -\frac{q_G}{\Delta\theta_Q}\left[\frac{L}{R} + \frac{L\cos(\chi_0 + \theta_{B0})}{p}\right], \tag{5.34}$$

or

$$d = -\frac{q_G W}{\Delta\theta_Q \cos(\chi_0 - \theta_{B0})}\left[\frac{1}{R} + \frac{\cos(\chi_0 + \theta_{B0})}{p}\right]. \tag{5.35}$$

(See Appendix B.6)

With the source distance at infinity, the optimal focus-to-detector distance, d_∞, is given by

$$d_\infty = R\frac{(1+\nu)\sin 2\chi_0 \cos(\theta_{B0} - \chi_0) + 2\sin(\theta_{B0} - \chi_0)}{4(\cos^2\chi_0 - \nu\sin^2\chi_0)\tan\theta_{B0}}. \tag{5.36}$$

For a symmetric bent Laue crystal with infinite source distance, the optimal focus-to-detector distance, d_∞^{sym}, is

$$d_\infty^{\text{sym}} = \frac{R\cos\theta_B}{2} \equiv q_{G\infty}, \tag{5.37}$$

where $q_{G\infty}$ is the geometric focal distance with infinite source distance.

When the detector is placed at this special position, the only contribution to the widening of the energy resolution is from the intrinsic Darwin width of the crystal and the source size. Given a pre-installed bent Laue

monochromator with an existing asymmetry angle, every energy of interest corresponds to a detector distance that optimizes the energy resolution. An example is shown in Figure 5.9(a) for a Si(022) monochromator with -15.8° asymmetry angle, 2 m bending radius and 22 m source distance. (Again, the effective detector pixel size resulted energy resolution contribution is put aside of the discussion in this work.)

By simply moving the detector upstream or downstream for a certain distance, existing bent Laue K-edge subtraction imaging systems will gain the capability for high energy resolution applications (e.g., spectral KES [49] and wide field x-ray absorption spectroscopy imaging [68]). It should be noted, however, that the detector distance for optimal energy resolution may be, and likely is, not accessible in many cases.

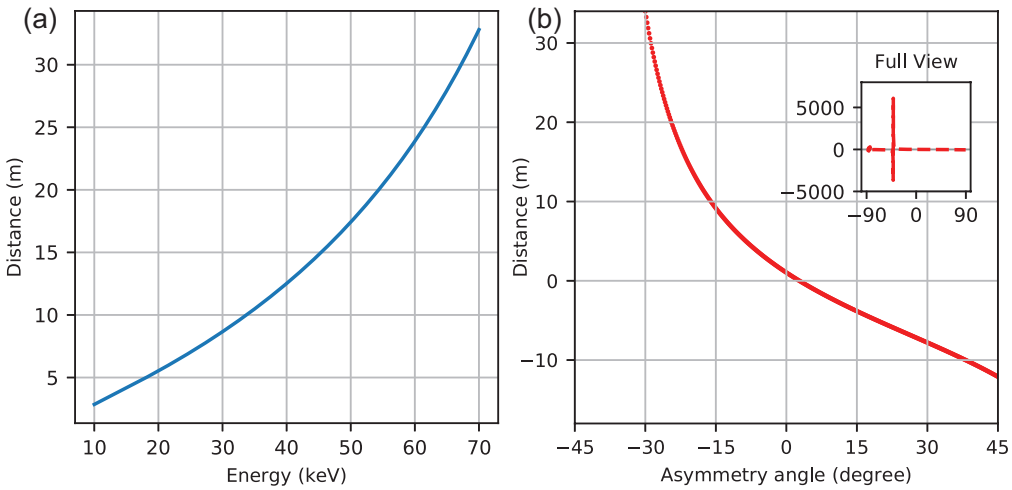

Figure 5.9: The optimal detector distance for a Si(022) reflection in a [5,1,1] oriented crystal with 22 m source distance, 2 m bending radius. (a) The optimal distance in range of energy. The asymmetry angle is -15.8°. (b) The optimal distance in range of asymmetry angle for x-rays at 33.169 keV.

For a particular energy of interest and tunable asymmetry angle, the relation between asymmetry angle and the optimal focus-to-detector distance is shown in Figure 5.9(b). The optimal focus-to-detector distance is found to be positive between the magic condition χ angle and a singularity χ angle. The singularity χ angle corresponds to zero directional energy spread in the quasi-mono beam.

5.5.5 Monochromatic focus

The optimal position for the detector is also the *monochromatic focus*. The monochromatic focus is the location where the x-rays with one energy intersect. The parameters taken into account is the lattice spacing variation and the source distance. The source size is not accounted for, but the energy blurring caused by the finite source size is a small portion of the total, especially for a synchrotron source.

The monochromatic focal distance is given by

$$q_E = q_G + d. \tag{5.38}$$

For a given monochromator, the monochromatic focal distance is energy dependent. As the example

shown in Figure 5.9(a), the distance-energy relation is nearly linear over a few keV range. Thus, for an energy range of a few hundred eVs, the blurring of energies off focus is not a major issue.

For a symmetric bent Laue crystal with infinite source distance, the monochromatic focal distance is

$$q_{E\infty}^{\text{sym}} = 2q_{G\infty} = R\cos\theta_B. \tag{5.39}$$

The existence of the monochromatic focus can be described in the following way as well. For fixed λ in $\lambda = 2d_{\text{hkl}}\sin\theta$, it requires a recombination of variation of lattice spacing, δd_{hkl}, and Bragg angle variation, $\delta\theta$, given by

$$\begin{aligned} \delta\lambda &= 2\sin\theta\delta d_{\text{hkl}} + 2d_{\text{hkl}}\cos\theta\delta\theta \equiv 0 \\ \delta\theta &= -\tan\theta\frac{\delta d_{\text{hkl}}}{d_{\text{hkl}}}. \end{aligned} \tag{5.40}$$

For fixed curvature of bent crystal, there is a continuous distribution in lattice spacings from the compressed side to the expanded side. Because of the curvature of the crystal, there will be planes where the variation in angle given by Equation (5.40) is met. Therefore, there is a continuous set of diffracted beams all with the same energy. And since there is a range of diffracted beam angles, this set of rays will focus somewhere: either at a real or virtual focus.

The concept of another 'monochromatic focus' has been described by Tolentino [55, 17] where the focus is located on the Rowland circle of the crystal for corresponding monochromatic x-rays. At this spot, the image size of the source is zero for these monochromatic x-rays, therefore the size of the source has zero contribution to the blurring of the energy. Tolentino's monochromatic focus works better for Bragg type monochromator than the Laue type. Because in a bent Laue type monochromator, the lattice spacing deformation caused by the bending of the crystal needs to be taken into account, and it is a much bigger contribution (inversely proportional to the crystal bending radius) than the source size related contribution to the energy blurring. Another limitation to Tolentino's monochromatic focus is that, to fulfill the Rowland circle geometry, the x-ray source has to be on the concave side of the crystal, which is not suitable for a focusing Laue monochromator where the convex side of the crystal is facing the source.

Whether the new monochromatic focus and Tolentino's monochromatic focus can be put together will be studied in future works.

5.6 Discussion

This paper describes the general behavior of bent Laue crystals from a ray-tracing point of view. Though this has been extensively covered in previous works, there is a need to decouple the description of the spatial focal properties of these crystals from the diffracted beam energies of the rays.

The analysis in this paper introduced a parallel quasi-monochromatic beam in the bent crystal diffracted x-rays. It interprets the bent crystal diffraction to rays diffracted at the crystal surface and their companion

quasi-mono beams. This quasi-mono beam leads to a deeper understanding of bent crystal diffraction because it (i) provides an intuitive view of bent crystal diffraction, (ii) contains both the energy and spatial information of the diffracted beam, (iii) builds the knowledge for more accurate evaluation of the energy resolution and, thus, (iv) directs to the options for improvements.

The quasi-mono beam approach predicts that bent Laue crystals have a monochromatic focus where the focused x-rays have the same energy. Note that this monochromatic focus is different from a previously known monochromatic focus [55, 17], because it accounts for the crystal lattice deformation and does not rely on the Rowland circle geometry. The Rowland circle is not such a useful tool in this situation because it depends only on the angular conditions for monochromatic point-to-point focusing and does not account for lattice spacing changes due to bending. Whether the two types of monochromatic focus can be put together is one topic of future work.

This new approach explains the magic condition, which gives the requirements for achieving a small spatial focus and good energy resolution, as a special case when the width of the quasi-mono beam is zero and, more importantly, the focusing behavior of bent crystals when the magic condition is not met. This allows one to predict the more realistic diffraction conditions encountered experimentally.

Acknowledgements

Research was funded by the Natural Sciences and Engineering Research Council of Canada (PQ, DC).

Chapter 6

Conclusion and Future Work

6.1 Conclusion

The thesis detailed an energy dispersive x-ray absorption spectroscopy wide field imaging system which was the primary objective of this work. The principle of the system, the instrumentation and the applications were studied and software for data analysis was developed.

The system provides a wide horizontal imaging beam that is vertically energy dispersed allowing for wide field imaging applications. The energy dispersive property is provided an asymmetric bent Laue crystal that matches the so-called 'magic condition'. The energy resolution achieves $\frac{\Delta E}{E} \approx 10^{-4}$ or about 2.6 eV at 12.658 keV, which is sufficient for Se speciation. The concentration sensitivity is about 5 mM (400 ppm or 0.04% weight) and is better than the typical concentration sensitivity expected for transmission XAS (0.1% weight). Because the beam in use is polychromatic, using fluorescence imaging to aid the sensitivity of the transmitted imaging is not an option. The advantage of this system is the combination of good energy dispersion and wide field of view comparing to conventional XAS. This makes 2D and 3D speciation screening of samples highly efficient.

A software package (XSIP) has been developed to analyse the data for both the wide-field XAS imaging technique and another x-ray imaging technique - spectral KES, because of the shared optical principle and analysis algorithm of the two techniques. XSIP automates the data analysing process and ensures that the potential spectral KES and wide-field XAS imaging synchrotron users can analyse the data independently. It is an open access software developed with Python 3.6 and accessible at `https://github.com/darwinqii/XSIP` along with detailed documentation for installation and user guide.

Motivated by optimizing the energy resolution of the system, a novel method of describing the bent Laue crystal optics is developed from a ray-tracing point of view. By introducing the concept of a quasi-monochromatic beam (a parallel diffracted beam), the new method is a general approach to describe the focal size and the energy properties of a bent Laue crystal. These concepts can provide important new tools for ray-tracing simulation.

The new approach explains the magic condition as a special case when the quasi-mono beam width equals zero. It also predicts the existence of a monochromatic focus, which takes into account the mutual effect of the crystal lattice spacing deformation, crystal curvature and the finite source distance so that these three

factors will not blur the energy resolution. The monochromatic focus predicts where the detector in an energy dispersive system should be placed for the best energy resolution.

6.2 Future Work

6.2.1 Future upgrades

Instrumentation

At the Se K-edge energy (12.658 keV), the air absorption rate of the x-ray is about 62% in the entire path of the beam. Evacuated flight path would reduce the air absorption and thus improve the signal captured by the detector.

A better cooling system can be built to improve the thermal stability of the monochromator. The frame of monochromator in-use is made of aluminium. An improved design could be using water-cooled copper as the frame material and a liquid metal, such as In-Ga eutectic, between the frame and the crystal for better thermal conductivity.

Adding angle flexibility for the '2θ rail' in the BMIT-BM experimental hutch would provide a more convenience and increase the potential of the system. Currently, the rail is fixed at 13 degrees, which is inconvenient for the Bragg diffraction angle of the present system and sometimes even makes experiments using other energies and diffraction planes not practical. Having the flexibility to adjust the angle of the rail provides the possibility for these needs.

Data analysis

In the current version of data analysis program, data with a certain range of energies are used for the analysis. However, data at some energies within the range do not provide the information to differentiate the references and some provide repetitive information as the neighbouring data. Therefore, an algorithm to effectively select the most informative subset of the data might improve the accuracy and efficiency of the analysis.

Another possible way for improvement is calculating the total element attenuation in all species with the K-edge subtraction algorithm. After quantifying the element, the percentage of all species can then be calculated with a least square fit.

6.2.2 Future applications

Considering the efficiency and the cost of the project, the monochromator built for the Se speciation project does not perfectly match the magic condition for the Se K-edge energy (12.658 keV). In fact, the magic condition for the present monochromator is met at 11.323 keV, which is closer to As K-edge energy (11.867 keV) and Ge K-edge energy (11.103 keV). Therefore, applications for studying As or Ge speciation will be

convenient since the monochromator is ready to use and theoretically will perform better than at the Se K-edge energy.

Provided the high efficiency of spectra acquisition, the developed system is well suited for time-resolved studies. As an example, a potential application is Se as a cathode material in batteries. The high concentration of Se in such batteries is favoured by transmission type XAS, and the change of oxidation state can be recorded by the high speed wide-field EDXAS imaging technique. The one dimensional spatial information in addition to the time-resolved x-ray absorption spectra is an advantage as it is not provided by most time-resolved XAS techniques.

6.2.3 Experimental proof of the predicted monochromatic focus

The new theory of interpreting bent Laue crystal optics provides novel and intuitive understanding of their behavior. The monochromatic focusing, which is a direct deduction from this theory, provides important information for the energy dispersion property of bent Laue diffraction. A direct application is that the energy resolution of a bent Laue imaging system can be highly improved with a special detector distance, and K-edge subtraction imaging systems with bent Laue crystals will possess the capability of XAS style imaging. This monochromatic focus is not because of a Rowland circle focusing with a bent crystal which occurs when a crystal is curved with a (mostly) fixed lattice parameter.

To prove the existence of the "non-Rowland circle" monochromatic focus, an asymmetric bent Laue crystal will be used to provide a focusing beam. This beam will arrive at a focus and de-focus after it, which will form an energy dispersive beam on the diffraction plane. This beam will arrive at an area detector perpendicular to the beam propagation direction, and thus an energy-position relation will be established on the detector.

The detector will be placed first at a location downstream to the monochromatic focus, then it will be moved upstream to the monochromatic focus location in steps. (The crystal used in this system will be carefully chosen so that the monochromatic focal distance will be larger than the geometric focus and within a practical range for the beamline experimental hutch). The energy resolution can be evaluated with the sharpness of an absorption K-edge while the detector is moved closer to the monochromatic focus. If the monochromatic focus is ignored, the observed changing of the energy resolution should be worse since the pixel size contribution is gets larger. However, the existence of the monochromatic focus should result in an improvement of energy resolution at that location.

The proof to the monochromatic focus will also be a proof to the new approach for understanding and describing bent Laue diffraction which makes ray-tracing easier to realize.

References

[1] R. Lobinski, C. Moulin, and R. Ortega. Imaging and speciation of trace elements in biological environment. *Biochimie*, 88(11):1591–1604, 2006.

[2] B. Wu and J. S. Becker. Imaging techniques for elements and element species in plant science. *Metallomics*, 4(5):403–416, 2012.

[3] R. P. Phizackerley, Z. U. Rek, G. B. Stephenson, S. D. Conradson, K. O. Hodgson, T. Matsushita, and H. Oyanagi. An energy-dispersive spectrometer for the rapid measurement of X-ray absorption spectra using synchrotron radiation. *Journal of Applied Crystallography*, 16(2):220–232, Apr 1983.

[4] F. Baudelet, Q. Kong, L. Nataf, J. D. Cafun, A. Congeduti, A. Monza, S. Chagnot, and J. P. Itié. ODE: a new beam line for high-pressure XAS and XMCD studies at SOLEIL. *High Pressure Research*, 31(1):136–139, Mar 2011.

[5] M. Muñoz, V. De Andrade, O. Vidal, E. Lewin, S. Pascarelli, and J. Susini. Redox and speciation micromapping using dispersive X-ray absorption spectroscopy: Application to iron in chlorite mineral of a metamorphic rock thin section. *Geochemistry, Geophysics, Geosystems*, 7(11), Nov 2006.

[6] S. Pascarelli and O. Mathon. Energy Dispersive XAS. In *XAFS Techniques for Catalysts, Nanomaterials, and Surfaces*, pages 109–125. Springer International Publishing, Cham, 2017.

[7] Y. Cauchois. *Les spectres de rayons X et la structure électronique de la matière*. Centre national de la recherche scientifique, 1948.

[8] K. Taniguchi, K. Oka, N. Yamaki, and S. Ikeda. X-Ray Spectrometer for EXAFS Using a Position Sensitive Detector. *Advances in X-ray Analysis*, 24:177–180, Mar 1980.

[9] U. Kaminaga, T. Matsushita, and K. Kohra. A Dispersive Method of Measuring Extended X-Ray Absorption Fine Structure. *Japanese Journal of Applied Physics*, 20(5):L355–L358, May 1981.

[10] T. Matsushita and R. P. Phizackerley. A Fast X-Ray Absorption Spectrometer for Use with Synchrotron Radiation. *Japanese Journal of Applied Physics*, 20(11):2223–2228, Nov 1981.

[11] A. Flank, A. Fontaine, A. Jucha, M. Lemonnier, D. Raoux, and C. Williams. EXAFS in dispersive mode, Apr 1983.

[12] E. Dartyge, A. Fontaine, A. Jucha, and D. Sayers. Fundamental Aspects in X-Ray Absorption in Dispersive Mode. In *EXAFS and Near Edge Structure III. Springer Proceedings in Physics*, pages 472–475. Springer, Berlin, Heidelberg, 1984.

[13] E. Dartyge, C. Depautex, J. Dubuisson, A. Fontaine, A. Jucha, P. Leboucher, and G. Tourillon. X-ray absorption in dispersive mode: A new spectrometer and a data acquisition system for fast kinetics. *Nuclear Instruments and Methods in Physics Research Section A: Accelerators, Spectrometers, Detectors and Associated Equipment*, 246(1-3):452–460, May 1986.

[14] M. Hagelstein, S. Cunis, R. Frahm, W. Niemann, and P. Rabe. The energy dispersive X-ray absorption spectrometer DEXAFS at HASYLAB. *Physica B: Condensed Matter*, 158(1-3):324–325, Jun 1989.

[15] F. D'Acapito, F. Boscherini, A. Marcelli, and S. Mobilio. Dispersive EXAFS apparatus at Frascati. *Review of Scientific Instruments*, 63(1):899–901, Jan 1992.

[16] P. L. Lee, M. A. Beno, G. Jennings, M. Ramanathan, G. S. Knapp, K. Huang, J. Bai, and P. A. Montano. An energy dispersive x-ray absorption spectroscopy beamline, X6A, at NSLS. *Review of Scientific Instruments*, 65(1):1–6, Jan 1994.

[17] H. Tolentino, E. Dartyge, A. Fontaine, and G. Tourillon. Improved optics of the energy dispersive spectrometer for X-ray absorption spectroscopy. *Physica B: Condensed Matter*, 158(1-3):317–321, Jun 1989.

[18] H. Tolentino, F. Baudelet, E. Dartyge, A. Fontaine, A. Lena, and G. Tourillo. Aberration-free and harmonic-free optics for time-resolved X-ray absorption spectroscopy using synchrotron radiation. *Nuclear Instruments and Methods in Physics Research Section A: Accelerators, Spectrometers, Detectors and Associated Equipment*, 289(1-2):307–316, Apr 1990.

[19] M. Hagelstein, C. Ferrero, M. del Rio, U. Hatje, T. Ressler, and W. Metz. XAFS with an energy-dispersive Laue monochromator. *Physica B: Condensed Matter*, 208-209:223–224, Mar 1995.

[20] J. Headspith, J. Groves, P. N. Luke, M. Kogimtzis, G. Salvini, S. L. Thomas, R. C. Farrow, J. Evans, T. Rayment, J. S. Lee, W. D. Goward, M. Amman, O. Mathon, and S. Diaz-Moreno. First experimental data from XH, a fine pitch germanium microstrip detector for Energy Dispersive EXAFS (EDE). *IEEE Nuclear Science Symposium Conference Record*, 4:2421–2428, 2007.

[21] S. Pascarelli, O. Mathon, T. Mairs, I. Kantor, G. Agostini, C. Strohm, S. Pasternak, F. Perrin, G. Berruyer, P. Chappelet, C. Clavel, and M. C. Dominguez. The Time-resolved and Extreme-conditions XAS (TEXAS) facility at the European Synchrotron Radiation Facility: the energy-dispersive X-ray absorption spectroscopy beamline ID24. *Journal of Synchrotron Radiation*, 23(1):353–368, Jan 2016.

[22] J. A. van Bokhoven and C. Lamberti. *X-Ray Absorption and X-Ray Emission Spectroscopy: Theory and Applications*. John Wiley and Sons, Ltd, Chichester, UK, Feb 2016.

[23] J. C. Cezar, N. M. Souza-Neto, C. Piamonteze, E. Tamura, F. Garcia, E. J. Carvalho, R. T. Neueschwander, A. Y. Ramos, H. C. N. Tolentino, A. Caneiro, N. E. Massa, M. J. Martinez-Lope, J. A. Alonso, J. Itié, C. Cezar, N. M. Souza-Neto, C. Piamonteze, E. Tamura, F. Garcia, E. J. Carvalho, R. T. Neueschwander, A. Y. Ramos, H. C. N. Tolentino, A. Caneiro, N. E. Massa, M. Jesus Martinez-Lope, J. A. Alonso, and J. Itié. Energy-dispersive X-ray absorption spectroscopy at LNLS: investigation on strongly correlated metal oxides. *Journal of Synchrotron Radiation*, 17(1):93–102, Jan 2010.

[24] D. Bhattacharyya, A. Poswal, S. Jha, Sangeeta, and S. Sabharwal. First results from a dispersive EXAFS beamline developed at INDUS-2 synchrotron source at RRCAT, Indore, India. *Nuclear Instruments and Methods in Physics Research Section A: Accelerators, Spectrometers, Detectors and Associated Equipment*, 609(2-3):286–293, Oct 2009.

[25] Z. W. Ouyang, Y. H. Matsuda, H. Nojiri, Y. Inada, Y. Niwa, and T. Arima. Insulator–metal phase transition of Pr0.6Ca0.4MnO3studied by x-ray absorption spectroscopy in pulsed magnetic fields. *Journal of Physics: Condensed Matter*, 21(1):16006, Jan 2008.

[26] Y. Okajima, D. Matsumura, Y. Nishihata, H. Konishi, and J. Mizuki. Energy dispersive XAFS in the high energy region at BL14B1 in SPring-8. In *AIP Conference Proceedings*, volume 879, pages 1234–1237. AIP, 2007.

[27] K. Kato, T. Uruga, H. Tanida, S. Yokota, K. Okumura, Y. Imai, T. Irie, and Y. Yamakata. Time-Resolved Energy-Dispersive XAFS Station for Wide-Energy Range at SPring-8. In S Choi, JY and Rah, editor, *AIP Conference Proceedings*, volume 879 of *AIP Conference Proceedings*, pages 1214–1217, Melville, USA, 2007. AIP.

[28] Y. Poo-arporn, P. Chirawatkul, W. Saengsui, S. Chotiwan, S. Kityakarn, S. Klinkhieo, J. Hormes, and P. Songsiriritthigul. Time-resolved XAS (Bonn-SUT-SLRI) beamline at SLRI. *Journal of Synchrotron Radiation*, 19(6):937–943, Nov 2012.

[29] M. Tada and Y. Iwasawa. Chemical Design and in Situ Characterization of Active Surfaces for Selective Catalysis. *Annual Review of Materials Research*, 35(1):397–426, Aug 2005.

[30] W. H. Zachariasen. *Theory of X-Ray Diffraction in Crystals*. John Wiley & Sons, Inc., New York, 1945.

[31] J. Als-Nielsen and D. McMorrow. *Elements of Modern X-ray Physics*. John Wiley and Sons, Inc., Hoboken, NJ, USA, Mar 2011.

[32] H. Zhang. *Imaging Dilute Contrast Materials in Small Animals Using Synchrotron Light*. PhD thesis, University of Saskatchewan, 2009.

[33] B. W. Batterman and H. Cole. Dynamical Diffraction of X Rays by Perfect Crystals, Jul 1964.

[34] M. Hagelstein, A. San Miguel, A. Fontaine, and J. Goulon. The Beamline ID24 at ESRF for Energy Dispersive X-Ray Absorption Spectroscopy. *Le Journal de Physique IV*, 7(C2):C2–303–C2–308, Apr 1997.

[35] S. Pascarelli, O. Mathon, and G. Aquilanti. New opportunities for high pressure X-ray absorption spectroscopy using dispersive optics. *Journal of Alloys and Compounds*, 362(1-2):33–40, Jan 2004.

[36] Y. Inada, A. Suzuki, Y. Niwa, and M. Nomura. Time-Resolved Dispersive XAFS Instrument at NW2A Beamline of PF-AR. In J Y Choi and S Rah, editors, *AIP Conference Proceedings*, volume 879, pages 1230–1233. AIP, 2007.

[37] H. A. Rowland. On concave gratings for optical purposes. *The London, Edinburgh, and Dublin Philosophical Magazine and Journal of Science*, 16(99):197–210, Sep 1883.

[38] R. Caciuffo, C. Ferrero, O. Francescangeli, and S. Melone. Theoretical reflectivities of bent crystal analyzers for fusion plasma diagnostics. *Review of Scientific Instruments*, 61(11):3467–3472, Nov 1990.

[39] M. Hagelstein, C. Ferrero, U. Hatje, T. Ressler, and W. Metz. Curved Crystal Transmission Optics for Energy-Dispersive X-ray Absorption Spectroscopy. *Journal of Synchrotron Radiation*, 2(4):174–180, Jul 1995.

[40] P. Penning and D. Polder. Anomalous transmission of X-rays in elastically deformed crystals. *Philips Res. Rep*, 16:419 – 440, 1961.

[41] E. Erola, V. Eteläniemi, P. Suortti, P. Pattison, and W. Thomlinson. X-ray reflectivity of bent perfect crystals in Bragg and Laue geometry. *Journal of Applied Crystallography*, 23(1):35–42, Feb 1990.

[42] S. Takagi. Dynamical theory of diffraction applicable to crystals with any kind of small distortion. *Acta Crystallographica*, 15(12):1311–1312, Dec 1962.

[43] U. Lienert, C. Schulze, V. Honkima, E. Ki, T. Tschentscher, S. Garbe, O. Hignette, A. Horsewell, M. Lingham, H. F. Poulsen, N. B. Thomsen, and E. Ziegler. Focusing optics for high-energy X-ray diffraction. *Journal of Synchrotron Radiation*, 5(3):226–231, 1998.

[44] M. Martinson, N. Samadi, B. Bassey, A. Gomez, and D. Chapman. Phase-preserving beam expander for biomedical X-ray imaging. *Journal of Synchrotron Radiation*, 22(3):801–806, May 2015.

[45] P. Suortti, W. Thomlinson, D. Chapman, N. Gmür, D. Siddons, and C. Schulze. A single crystal bent Laue monochromator for coronary angiography. *Nuclear Instruments and Methods in Physics Research Section A: Accelerators, Spectrometers, Detectors and Associated Equipment*, 336(1-2):304–309, Nov 1993.

[46] C. Schulze and U. Lienert. Focusing of High Energy X-rays by Bent Crystal Optics, 1996.

[47] C. Schulze, U. Lienert, M. Hanfland, M. Lorenzen, and F. Zontone. Microfocusing of Hard X-rays with Cylindrically Bent Crystal Monochromators. *Journal of Synchrotron Radiation*, 5(2):77–81, Mar 1998.

[48] Y. Zhu. *Bent Laue Crystals in Biomedical X-ray Imaging Applications*. Doctor of philosophy, University of Saskatchewan, 2012.

[49] Y. Zhu, N. Samadi, M. Martinson, B. Bassey, Z. Wei, G. Belev, and D. Chapman. Spectral K-edge subtraction imaging. *Physics in Medicine and Biology*, 59(10):2485–2503, May 2014.

[50] N. Kato. Pendellösung Fringes in Distorted Crystals I. Fermat's Principle for Bloch Waves. *Journal of the Physical Society of Japan*, 18(12):1785–1791, Dec 1963.

[51] D. Taupin. Théorie dynamique de la diffraction des rayons X par les cristaux déformés. *Bulletin de la Société française de Minéralogie et de Cristallographie*, 87(4):469–511, 1964.

[52] C. Schulze and D. Chapman. pepo: A program for the calculation of the reflectivity of cylindrically bent Laue crystal monochromators. *Review of Scientific Instruments*, 66(2):2220–2223, Feb 1995.

[53] M. Sanchez Del Rio, N. Perez-Bocanegra, X. Shi, V. Honkimäki, and L. Zhang. Simulation of X-ray diffraction profiles for bent anisotropic crystals. *J. Appl. Cryst*, 48:477–491, 2015.

[54] G. Ice and C. Sparks. Focusing optics for a synchrotron x-radiation microprobe. *Nuclear Instruments and Methods in Physics Research*, 222(1-2):121–127, May 1984.

[55] H. Tolentino, E. Dartyge, A. Fontaine, and G. Tourillon. X-ray absorption spectroscopy in the dispersive mode with synchrotron radiation: optical considerations. *Journal of Applied Crystallography*, 21(1):15–22, 1988.

[56] P. G. Allen, S. D. Conradson, and J. E. Penner-Hahn. A four-point crystal bender for dispersive X-ray absorption spectroscopy. *Journal of Applied Crystallography*, 26(2):172–179, Apr 1993.

[57] A. Dent, J. Evans, M. Newton, J. Corker, A. Russell, M. B. Abdul Rahman, S. Fiddy, R. Mathew, R. Farrow, G. Salvini, and P. Atkinson. High-quality energy-dispersive XAFS on the 1 s timescale applied to electrochemical and catalyst systems. *Journal of Synchrotron Radiation*, 6(3):381–383, May 1999.

[58] P. M. de Wolff. Focusing monochromators and transmission techniques. *Norelco Rep*, 15:44–49, 1968.

[59] J. H. Underwood. Generation of a parallel X-ray beam and its use for testing collimators. *Space Science Instrumentation, vol. 3, Nov. 1977, p. 259-270.*, 3:259–270, 1977.

[60] J. Pellicer-Porres, A. San Miguel, and A. Fontaine. High-Focusing Bragg-Crystal Polychromator Design for Energy-Dispersive X-ray Absorption Spectroscopy. *Journal of Synchrotron Radiation*, 5(5):1250–1257, Sep 1998.

[61] A. San-Miguel, M. Hagelstein, J. Borrel, G. Marot, and M. Renier. An exchangeable Bragg/Laue polychromator for energy-dispersive XAFS. *Journal of Synchrotron Radiation*, 5(6):1396–1397, Nov 1998.

[62] S. Pascarelli, O. Mathon, M. Muñoz, T. Mairs, and J. Susini. Energy-dispersive absorption spectroscopy for hard-X-ray micro-XAS applications. *Journal of Synchrotron Radiation*, 13(5):351–358, Sep 2006.

[63] Y. Yoneda, N. Matsumoto, Y. Furukawa, and T. Ishikawa. Fixed-height exit bender of synchrotron X-rays above 40 keV, Jan 2001.

[64] A. Artemev, N. Artemiev, E. Busetto, F. Franc, J. Hrdý, D. Mraźek, and A. Savoia. Design, construction and tests of a crystal bender which provides constant position of the central part of the crystal. *Nuclear Instruments and Methods in Physics Research Section A: Accelerators, Spectrometers, Detectors and Associated Equipment*, 467-468:377–379, Jul 2001.

[65] R. T. Neuenschwander and H. C. N. Tolentino. Bent Crystal Monochromator with Constant Crystal Center Position and 2-theta Arm for a Dispersive Beamline, Jun 2004.

[66] K. Kato, T. Irie, T. Uruga, K. Uera, and M. Kawase. Development of highly stable Bragg polychromator for energy dispersive XAFS. *Journal of Physics: Conference Series*, 712:012025, May 2016.

[67] B. Bassey, M. Martinson, N. Samadi, G. Belev, C. Karanfil, P. Qi, and D. Chapman. Multiple energy synchrotron biomedical imaging system. *Physics in Medicine and Biology*, 61(23):8180–8198, Dec 2016.

[68] P. Qi, N. Samadi, M. Martinson, O. Ponomarenko, B. Bassey, A. Gomez, G. N. George, I. J. Pickering, and L. D. Chapman. Wide field imaging energy dispersive X-ray absorption spectroscopy. *Scientific Reports*, 9(1):17734, Dec 2019.

[69] N. Allinson and G. Greaves. Hybrid linear array detectors for synchrotron radiation applications. *Nuclear Instruments and Methods in Physics Research Section A: Accelerators, Spectrometers, Detectors and Associated Equipment*, 273(2-3):620–624, Dec 1988.

[70] I. Kantor, J. C. Labiche, E. Collet, L. Siron, J. J. Thevenin, C. Ponchut, J. Borrel, T. Mairs, C. Marini, C. Strohm, O. Mathon, and S. Pascarelli. A new detector for sub-millisecond EXAFS spectroscopy at the European Synchrotron Radiation Facility. *Journal of Synchrotron Radiation*, 21(6):1240–1246, Nov 2014.

[71] M. Hagelstein, U. Lienert, T. Ressler, A. San Miguel, A. Freund, S. Cunis, C. Schulze, A. Fontaine, and J. Hodeau. A scattering filter for energy-dispersive optics. *Journal of Synchrotron Radiation*, 5(3):753–755, May 1998.

[72] M. Tromp, A. J. Dent, J. Headspith, T. L. Easun, X. Z. Sun, M. W. George, O. Mathon, G. Smolentsev, M. L. Hamilton, and J. Evans. Energy dispersive xafs: Characterization of electronically excited states of copper(I) complexes. *Journal of Physical Chemistry B*, 117(24):7381–7387, Jun 2013.

[73] R. F. Pettifer, O. Mathon, S. Pascarelli, M. D. Cooke, and M. R. J. Gibbs. Measurement of femtometre-scale atomic displacements by X-ray absorption spectroscopy. *Nature*, 435(7038):78–81, May 2005.

[74] S. Pascarelli and O. Mathon. Advances in high brilliance energy dispersive X-ray absorption spectroscopy. *Physical Chemistry Chemical Physics*, 12(21):5535, May 2010.

[75] O. Mathon, F. Occelli, E. Lescoute, A. Sollier, P. Loubeyre, W. Helsby, J. Headspith, R. Torchio, I. Kantor, and S. Pascarelli. High pressure dynamic XAS studies using an energy-dispersive spectrometer. *High Pressure Research*, 36(3):404–418, 2016.

[76] R. A. Mayanovic, A. J. Anderson, H. A. N. Dharmagunawardhane, S. Pascarelli, and G. Aquilanti. Monitoring synchrotron X-ray-induced radiolysis effects on metal (Fe, W) ions in high-temperature aqueous fluids. *Journal of Synchrotron Radiation*, 19(5):797–805, Sep 2012.

[77] M. Sikora, O. Mathon, P. van der Linden, J. M. Michalik, J. M. de Teresa, Cz. Kapusta, and S. Pascarelli. Field-induced magnetostructural phase transition in double perovskite ca_2fereo_6 studied via x-ray magnetic circular dichroism. *Phys. Rev. B*, 79:220402, Jun 2009.

[78] S. Pascarelli, T. Neisius, S. De Panfilis, M. Bonfim, S. Pizzini, K. Mackay, S. David, A. Fontaine, A. San Miguel, J. P. Itié, M. Gauthier, and A. Polian. Dispersive XAS at third-generation sources: strengths and limitations. *Journal of Synchrotron Radiation*, 6(3):146–148, May 1999.

[79] N. Samadi, M. Martinson, B. Bassey, A. Gomez, G. Belev, and D. Chapman. An energy dispersive bent Laue monochromator for K-edge subtraction imaging. In C Shen, Q and Nelson, editor, *Proceedings of the 12th international conference on synchrotron radiation instrumentation (SRI2015)*, volume 1741 of *AIP Conference Proceedings*, page 040004. Natl Synchrotron Light Source II; Brookhaven Natl Lab, Amer Inst Physics, Jul 2016.

[80] P. Suortti and A. K. Freund. On the phase-space description of synchrotron x-ray beams. *Review of Scientific Instruments*, 60(8):2579–2585, Aug 1989.

[81] S. Takagi. A dynamical theory of diffraction for a distorted crystal. *Journal of the Physical Society of Japan*, 26(5):1239–1253, May 1969.

[82] P. Suortti, U. Lienert, and C. Schulze. Focusing monochromators for high energy synchrotron radiation. *Nuclear Instruments and Methods in Physics Research Section A: Accelerators, Spectrometers, Detectors and Associated Equipment*, 338(1):27–32, Jan 1994.

[83] P. Suortti, U. Lienert, and C. Schulze. Bent crystal optics for high energy synchrotron radiation. In *The 17th international conference on x-ray and inner-shell processes*, volume 389, pages 175–192. ASCE, 1997.

[84] H. Elleaume, A. M. Charvet, P. Berkvens, G. Berruyer, T. Brochard, Y. Dabin, M. C. Dominguez, A. Draperi, S. Fiedler, G. Goujon, G. Le Duc, M. Mattenet, C. Nemoz, M. Perez, M. Renier, C. Schulze, P. Spanne, P. Suortti, W. Thomlinson, F. Esteve, B. Bertrand, and J. F. Le Bas. Instrumentation of the ESRF medical imaging facility. *Nuclear Instruments and Methods in Physics Research, Section A: Accelerators, Spectrometers, Detectors and Associated Equipment*, 428(2):513–527, 1999.

[85] A. Paszke, S. Gross, F. Massa, A. Lerer, J. Bradbury, G. Chanan, T. Killeen, Z. Lin, N. Gimelshein, L. Antiga, A. Desmaison, A. Köpf, E. Yang, Z. DeVito, M. Raison, A. Tejani, S. Chilamkurthy, B. Steiner, L. Fang, J. Bai, and S. Chintala. PyTorch: An Imperative Style, High-Performance Deep Learning Library. In H Wallach, H Larochelle, A Beygelzimer, F d'Alché-Buc, E Fox, and R Garnett, editors, *Advances in Neural Information Processing Systems 32*, pages 8024–8035. Curran Associates, Inc., 2019.

[86] T. E. Oliphant. *A guide to NumPy*, volume 1. Trelgol Publishing USA, 2006.

[87] G. Van Rossum and F. L. Drake. *Python 3 Reference Manual*. Centrum voor Wiskunde en Informatica Amsterdam, The Netherlands, Scotts Valley, CA, 2009.

[88] S. Van Der Walt, J. L. Schönberger, J. Nunez-Iglesias, F. Boulogne, J. D. Warner, N. Yager, E. Gouillart, and T. Yu. Scikit-image: Image processing in python. *PeerJ*, 2014(1), 2014.

[89] A. C. Kak and M. Slaney. *Principles of computerized tomographic imaging*. IEEE Press, New York, 1988.

[90] R. Buschert, M. D. Giardina, A. Merlini, A. Balerna, and S. Mobilio. Laboratory EXAFS in a dispersive mode. *Journal of Applied Crystallography*, 21(2):79–85, 1988.

[91] M. A. Newton and A. J. Dent. Energy-Dispersive EXAFS: Principles and Application in Heterogeneous Catalysis. In J A Rodriguez, J C Hanson, and P J Chupas, editors, *In-situ Characterization of Heterogeneous Catalysts*, pages 75–119. John Wiley & Sons, Inc., Hoboken, NJ, USA, Jun 2013.

[92] O. Mathon, I. Kantor, and S. Pascarelli. Time-Resolved XAS Using an Energy Dispersive Spectrometer: Techniques and Applications. In *X-Ray Absorption and X-Ray Emission Spectroscopy*, pages 185–212. John Wiley & Sons, Ltd, Chichester, UK, Jan 2016.

[93] J. P. Guigay and C. Ferrero. Dynamical focusing by bent, asymmetrically cut perfect crystals in Laue geometry. *Acta Crystallographica Section A Foundations and Advances*, 72(4):489–499, Jul 2016.

[94] G. Borrmann. Röntgenwellenfelder. In *Beiträge zur Physik und Chemie des 20. Jahrhunderts*, pages 262–282. Vieweg+Teubner Verlag, Wiesbaden, 1959.

[95] G. S. Bañuelos, S. C. Fakra, S. S. Walse, M. A. Marcus, S. I. Yang, I. J. Pickering, E. A. H. Pilon-Smits, and J. L. Freeman. Selenium Accumulation, Distribution, and Speciation in Spineless Prickly Pear Cactus: A Drought- and Salt-Tolerant, Selenium-Enriched Nutraceutical Fruit Crop for Biofortified Foods. *Plant Physiology*, 155(1):315–327, 2011.

[96] I. J. Pickering, R. C. Prince, D. E. Salt, and G. N. George. Quantitative, chemically specific imaging of selenium transformation in plants. *Proceedings of the National Academy of Sciences*, 97(20):10717–10722, 2000.

[97] G. F. Combs. Selenium in global food systems. *British Journal of Nutrition*, 85(5):517–547, May 2001.

[98] L. C. Clark, G. F. Combs, B. W. Turnbull, E. H. Slate, D. K. Chalker, J. Chow, L. S. Davis, R. A. Glover, G. F. Graham, E. G. Gross, A. Krongrad, J. L. Lesher, H. K. Park, B. B. Sanders, C. L. Smith, and J. R. Taylor. Effects of selenium supplementation for cancer prevention in patients with carcinoma of the skin. A randomized controlled trial. Nutritional Prevention of Cancer Study Group. *JAMA*, 276(24):1957–63, Dec 1996.

[99] D. R. Ellis and D. E. Salt. Plants, selenium and human health. *Current Opinion in Plant Biology*, 6(3):273–279, Jun 2003.

[100] P. D. Whanger. Selenium and its relationship to cancer: an update. *British Journal of Nutrition*, 91(1):11–28, Jan 2004.

[101] M. P. Rayman, H. G. Infante, and M. Sargent. Food-chain selenium and human health: spotlight on speciation. *British Journal of Nutrition*, 100(2):238–253, Aug 2008.

[102] A. Tsubura, Y. Lai, M. Kuwata, N. Uehara, and K. Yoshizawa. Anticancer Effects of Garlic and Garlic-derived Compounds for Breast Cancer Control. *Anti-Cancer Agents in Medicinal Chemistry*, 11(3):249–253, Mar 2011.

[103] A. M. Davis. Selenium Accumulation in a Collection of Atriplex Species. *Agronomy Journal*, 64(6), 1972.

[104] A. M. Davis. Selenium Uptake in Astragalus and Lupinus Species1. *Agronomy Journal*, 78(4), 1986.

[105] J. L. Freeman, L. H. Zhang, M. A. Marcus, S. Fakra, S. P. McGrath, and E. A. H. Pilon-Smits. Spatial imaging, speciation, and quantification of selenium in the hyperaccumulator plants Astragalus bisulcatus and Stanleya pinnata. *Plant physiology*, 142(1):124–34, Sep 2006.

[106] J. J. Tse, M. Gallego-Gallegos, E. D. Franz, K. Liber, and I. J. Pickering. Selenium speciation and localization in chironomids from lakes receiving treated metal mine effluent. *Chemosphere*, 89(3):274–279, 2012.

[107] A. Carey, E. Lombi, E. Donner, M. de Jonge, T. Punshon, B. Jackson, M. Guerinot, A. Price, and A. Meharg. A review of recent developments in the speciation and location of arsenic and selenium in rice grain. *Analytical and Bioanalytical Chemistry*, 402(10):3275–3286, 2012.

[108] J. R. Valdez Barillas, C. F. Quinn, J. L. Freeman, S. D. Lindblom, S. C. Fakra, M. A. Marcus, T. M. Gilligan, E. R. Alford, A. L. Wangeline, and E. A. H. Pilon-Smits. Selenium Distribution and Speciation in the Hyperaccumulator Astragalus bisulcatus and Associated Ecological Partners. *Plant Physiology*, 159(4):1834–1844, 2012.

[109] C. M. Weekley, A. Shanu, J. B. Aitken, S. Vogt, P. K. Witting, and H. H. Harris. XAS and XFM studies of selenium and copper speciation and distribution in the kidneys of selenite-supplemented rats. *Metallomics*, 6(9):1602–1615, 2014.

[110] I. J. Pickering, G. N. George, V. Van Fleet-Slalder, T. G. Chasteen, and R. C. Prince. X-ray absorption spectroscopy of selenium-containing amino acids. *Journal of Biological Inorganic Chemistry*, 4(6):791–794, Dec 1999.

[111] B. E. Etschmann, E. Donner, J. Brugger, D. L. Howard, M. D. De Jonge, D. Paterson, R. Naidu, K. G. Scheckel, C. G. Ryan, and E. Lombi. Speciation mapping of environmental samples using XANES imaging. *Environmental Chemistry*, 11(3):341–350, 2014.

[112] M. Sanchez del Rio, N. Canestrari, F. Jiang, and F. Cerrina. SHADOW3 : a new version of the synchrotron X-ray optics modelling package. *Journal of Synchrotron Radiation*, 18(5):708–716, Sep 2011.

[113] A. Shrift and T. Virupaksha. Seleno-amino acids in selenium-accumulating plants. *Biochimica et Biophysica Acta (BBA) - General Subjects*, 100(1):65–75, Apr 1965.

[114] T. W. Wysokinski, D. Chapman, G. Adams, M. Renier, P. Suortti, and W. Thomlinson. Beamlines of the biomedical imaging and therapy facility at the Canadian light source—Part 1. *Nuclear Instruments and Methods in Physics Research Section A: Accelerators, Spectrometers, Detectors and Associated Equipment*, 582(1):73–76, Nov 2007.

[115] P. Qi, X. Shi, N. Samadi, and D. Chapman. Focusing and energy dispersion properties of a cylindrically bent asymmetric Laue crystal. In Christian Morawe, Ali M. Khounsary, and Shunji Goto, editors, *Advances in X-Ray/EUV Optics and Components XIV*, volume 11108E, page 12. SPIE, Sep 2019.

[116] N. Kozul, G. R. Davis, P. Anderson, and J. C. Elliott. Elemental quantification using multiple-energy x-ray absorptiometry. *Measurement Science and Technology*, 10(3):252–259, Mar 1999.

Appendix A

Wide Field EDXAS Imaging Experiment Procedures

This document is adapted from the spectral KES imaging setup document, originally developed by Dr. Nazanin Samadi at Canadian Light Source, Biomedical Imaging and Therapy Facility.

A.1 Beamline

1. Change the beamline to the 'white beam' mode.
   - In the EPIC software (master controller), switch to 'white beam' mode.
   - Adjust the vertical position of the ion chamber in POE-3 (BMIT-BM @ CLS).
2. Block the transmitted white beam after the monochromator with a lead brick as shown in Figure A.1.

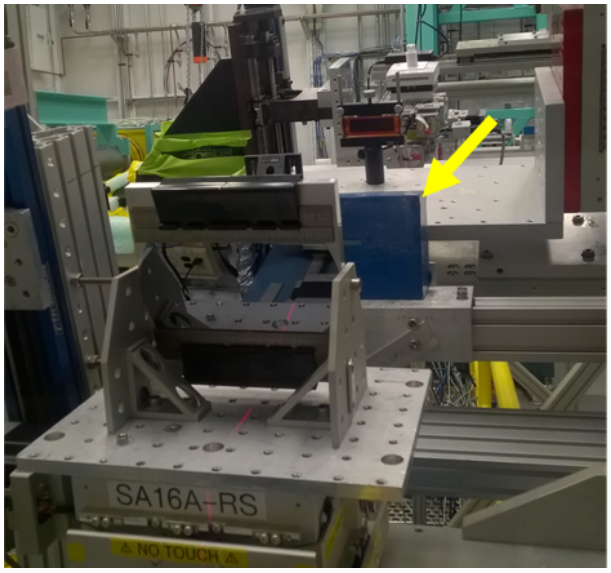

Figure A.1: System setup overview. A lead block downstream to the monochromator blocks the transmitted white beam.

3. Filter: Aluminum 0.4 mm.

A.2 Stages

Monochromator stage is on the first table. It should be motorized vertically, horizontal (optional), Bragg and Chi stages (Bragg at the bottom).

Contrast agent stage is on the rail before the sample stage. It should be motorized vertical for conveniently moving it in and out of the beam when collecting Edge image (Figure A.2).

Sample stage is on the rail. It has three axes rotational stages. The driver (stored in the cabinet in the POE-3 hutch) of the motors need to be connected (power, ethernet, motor) prior to the experiment (Figure A.3).

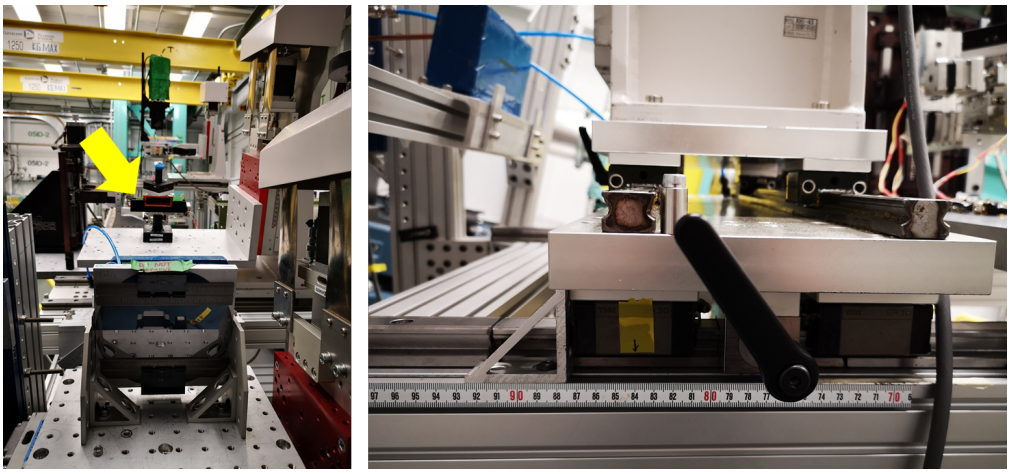

Figure A.2: Contrast agent stage is between the monochromator stage and the sample stage. The position of this stage is shown in the figure on the right (Mar. 11, 2020).

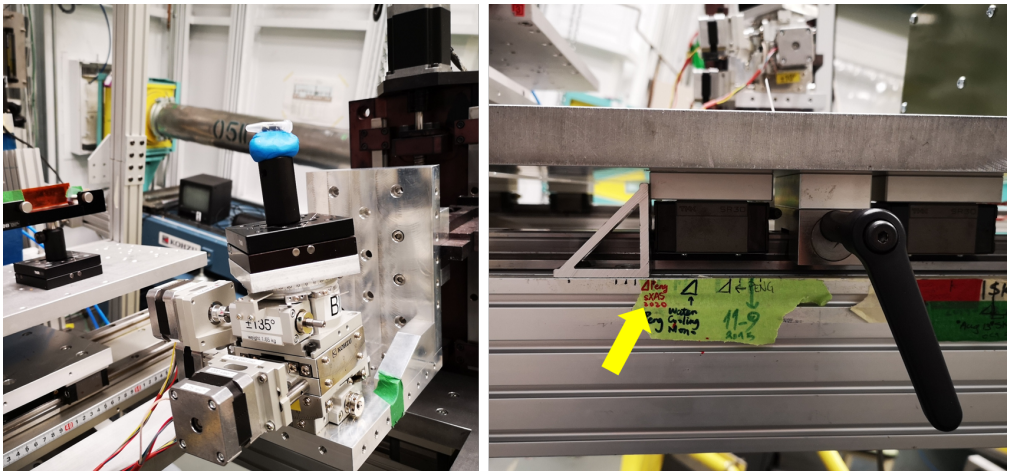

Figure A.3: The position of the sample is the focus of the monochromator (91 cm in the experiment on Mar 11th, 2020). The position on the rail is marked as shown in the figure on the right.

Detector stage is on the rail, after the RMD sample stage (Figure A.4).

- The vertical stage for the detector must be motorized, so you can move it up and down to catch the beam.
- The surface of the detector should be perpendicular to the x-ray beam so that the base of the detector should be tilted to be parallel to the 2θ angle (17.9 deg for the current WF-EDXAS monochromator) by using a pitch rotation stage on the bottom.
- Center the detector horizontally to the beam after the crystal. you can use the lasers in the hutch to do that.

A.3 Monochromator

1. **Find the monochromator** in the cabinet in POE-3. Do not remove the crystal from the frame or change its tilt angle on the frame.
2. **Install the monochromator on to the stage**

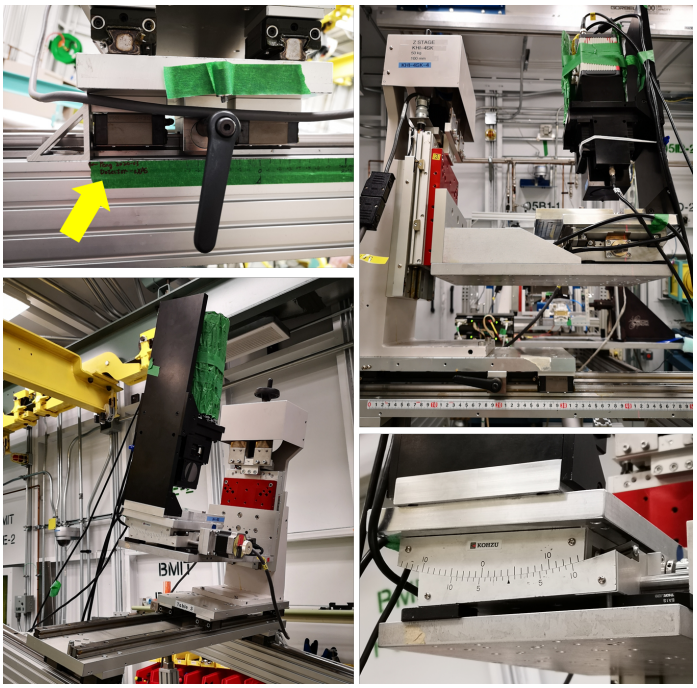

Figure A.4: The detector position is labeled on the rail (Mar. 11, 2020). Pitch stage is used at the bottom to tilt the detector angle. The stage in the figure is on the edge of the horizontal rail. Try to leave some space for the horizontal movement.

- Bolt the crystal on the Bragg-Chi stack with the convex side facing the incoming beam (one bolt is OK, two is better. Figure A.5)
- Tilt the angle of the monochromator by using the stages. Bragg angle for Se K-edge with Si(111) reflection is 8.99°. The 2θ arm will be 17.98°.
- Tilt the Chi axis to make the stage level.

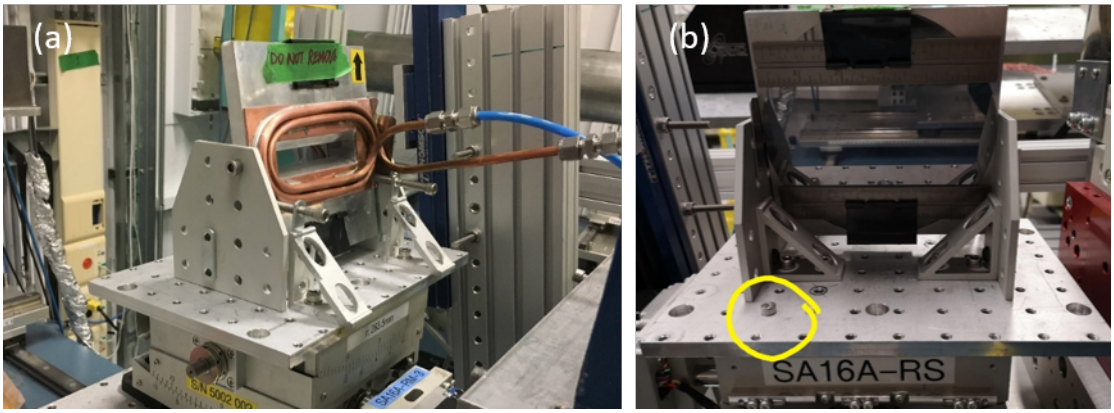

Figure A.5: The WF-EDXAS monochromator. The position for one bolt is marked.

3. **Enable the water cooler**

- Connect the tubes on the monochromator to the water cooling system.
- Turn on the water cooling machine (Figure A.6).

Figure A.6: Water cooling machine.

A.4 Contrast Agent

1. **Se film for Se K-edge.**

   A contrast agent with distinctive absorption edge structure is needed for energy calibration. In this case, elemental selenium film is used, which is kept with the monochromator.

2. **Mount it on the contrast agent stage** (Figure A.7). Again, vertical motorization is needed for moving the agent in and out of the beam.

Figure A.7: Se film on the contrast agent stage.

A.5 Find the K-edge

In brief, tune the Bragg angle to find the energy.

1. Make sure the crystal is vertically and horizontally centered to the white beam. Use fluorescence screen around the slit on the upstream side of the frame to see if there is beam outside of the slit.

2. Tune the motorized Bragg stage until the desired beam going through the K-edge.

   - Use a fluorescence screen on the contrast agent stage to locate the beam.
   - When the diffracted beam is on the screen, put the contrast agent in the beam to confirm the K-edge. Now a dramatic change in absorption will be observed when the edge energy is passed.

3. Move the detector vertically and park the beam in the center of the detector. Using a big sheet of fluorescence screen in front of the detector is handy to find the beam at the detector position before tuning the detector vertical position.

4. Tune the Bragg axis again and park the edge where one-third of the beam have lower energies than the K-edge. (Lower energy on top of the image if the detector is not flipped. Figure A.8.)

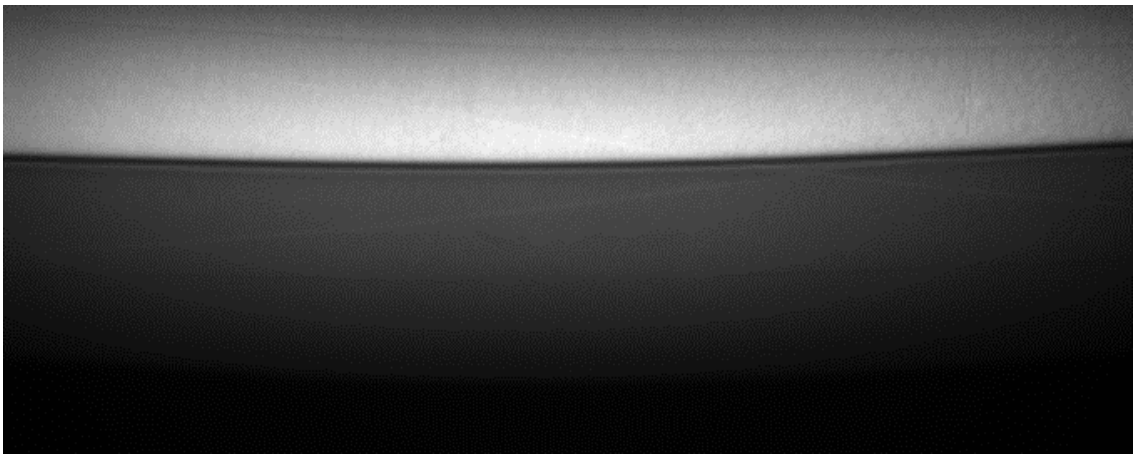

Figure A.8: Image of the beam at Se K-edge going through a Se film. The top bight part of the beam is x-rays with energies below the K-edge and the bottom dark part of the beam is x-rays with energies above the K-edge.

5. Put the contrast agent back to its stage for Edge imaging collection later.

A.6 Sample

1. There is no horizontal motion freedom for the sample stage. If the sample is not at the center of the beam, adjust the beam position of the beamline.

2. Find the focus position of the monochromator by using a pinpoint (Figure A.9).

   The focal distance is about 91 cm for this monochromator (about half of the bending radius). The focus position of the beam is marked on the rail, adjust sample horizontal based on that.

3. CT Alignment. Use the following LabVIEW VI's for sample stages (Figure A.10):

   - Sample vertical: 'Vertical Stage (RMD)'
   - Sample rotation: 'Small Rotation Motor'
   - Sample Bragg: 'Small Pitch Stage'
   - Sample Chi: 'Small Roll Stage'

4. Use sample holders as thin as possible to reduce unnecessary absorption.

Figure A.9: Use a pin on the sample stage to locate the focus of the beam.

A.7 Data Collection

10 Flats, 10 Darks, 10 Edges, n Tomos.

1. Prepare the folders. Name them in the following way. Replace 'AnInformative&BriefName' with an informative and brief name.

   - AnInformative&BriefName
   - AnInformative&BriefName/FlatBefore
   - AnInformative&BriefName/DarkBefore
   - AnInformative&BriefName/EdgeABefore
   - AnInformative&BriefName/Tomo

2. Collect Flat images and Dark images for data normalization. Save them in the 'FlatBefore' and 'DarkBefore' folders, respectively.

3. Besides, 10 Edge images are required for energy calibration. Move the contrast agent into the beam and take 10 Edge images (Figure A.8) and save them the 'EdgeABefore' folder. Make sure that the contrast agent covers the entire field of view.

4. Scan the sample. Use 'CT-multiview' for the scanning control. Refer to the numbers in Figure A.11, A.12 for the settings.

   Set the data saving directory to be the 'Tomo' folder.

5. Measure and record some numbers in the 'arrangement.dat' file. **Do not** rename the file.

   - Crystal to sample distance (focal distance).
   - Sample to detector distance (f2d distance).
   - The effective pixel size of the detector.

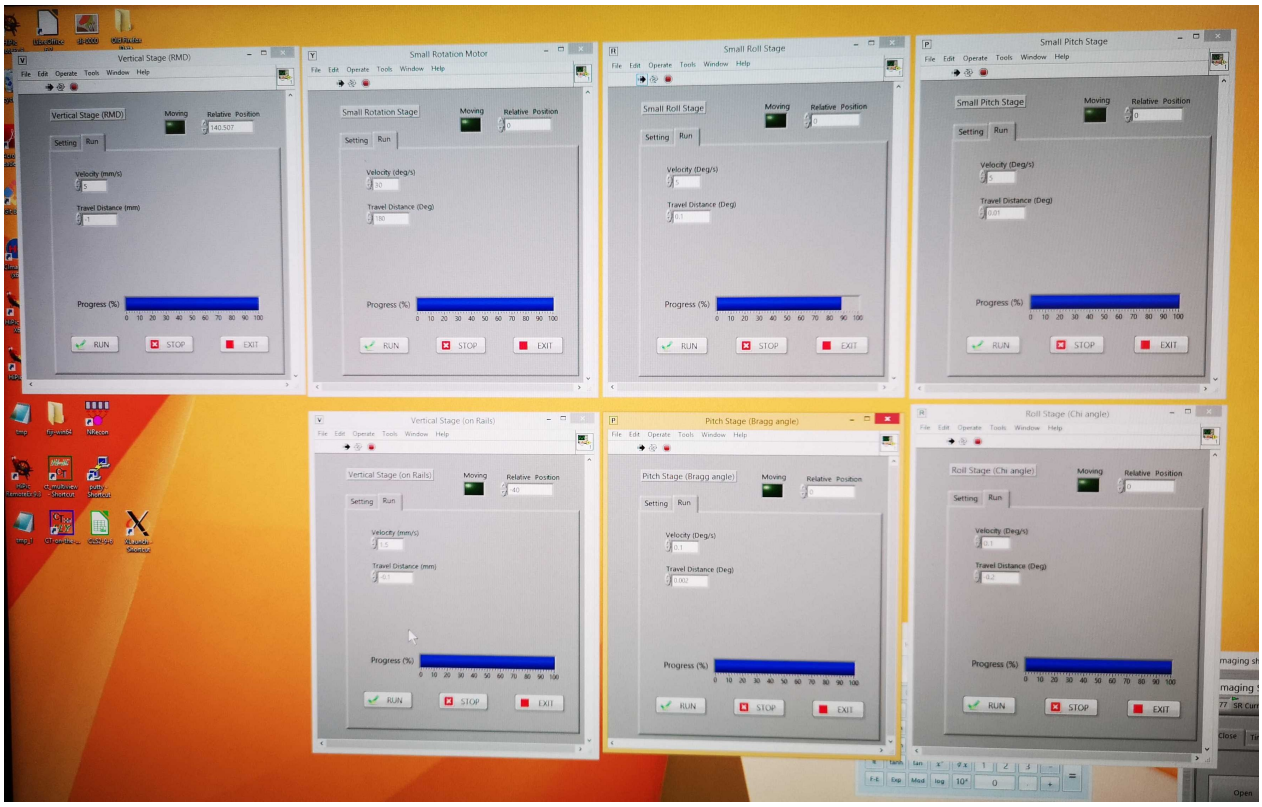

Figure A.10: Sample stage control programs.

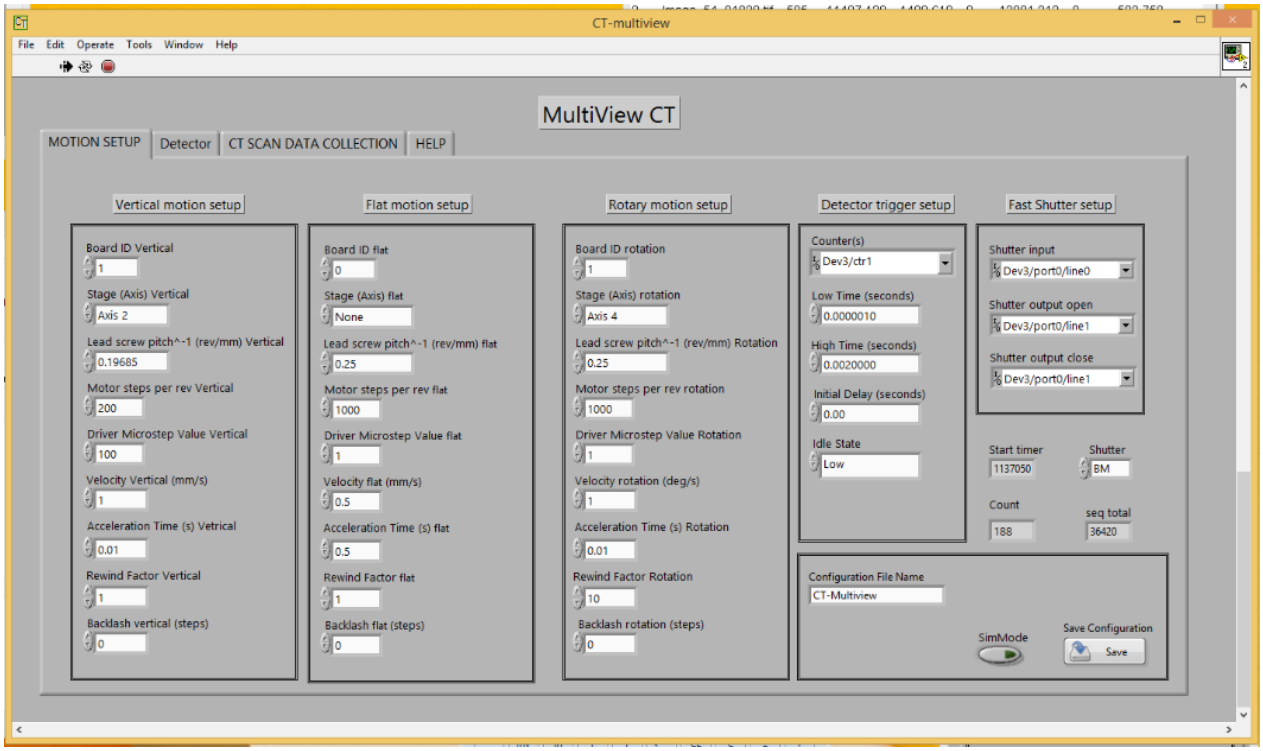

Figure A.11: CT scanning control setup.

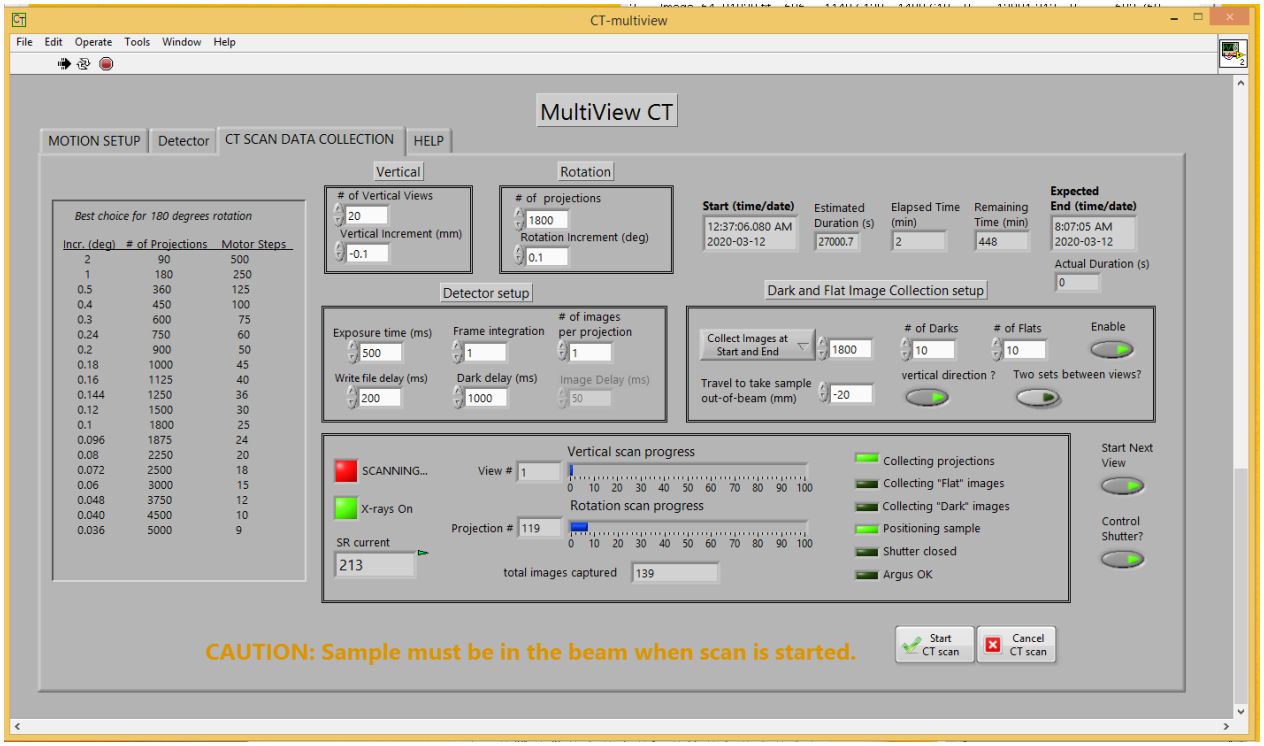

Figure A.12: CT scanning control setup.

Appendix B

Magic Condition Related Calculations

B.1 $\Delta\chi$ and $\Delta\phi$

Due to the bending force, the crystal is compressed on the concave side and expanded on the convex side in the direction of axis Y as shown in Figure B.1. The compression or expansion causes an opposite deformation in the direction of axis X and Z. Axis Z (not shown in the figure) is orthogonal to the plane of XY, and not considered in the discussion here. The thickness of the crystal (along axis X) is changed by bending considering the elastic property of the crystal through Poisson's ratio, which is defined by

$$\nu = -(\Delta X/X)/(\Delta Y/Y). \tag{B.1}$$

The negative sign implies that the compression (expansion) ΔY results in a transverse expansion (compression) ΔX. Thus, a crystal when bent will experience a growth in thickness on the compressed concave side and a reduction in thickness on the expanded convex side. For a crystal with original thickness T_0, it has a thickness on the compressed side of the neutral plane as τ_+, the expanded side as τ_- and a total bent thickness T for the discussion hereunder.

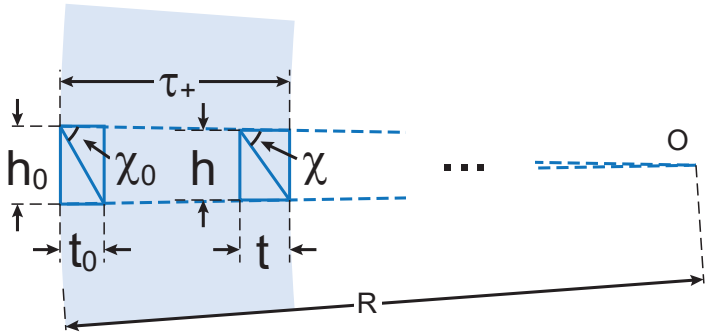

Figure B.1: Schematic view to estimate the change in angle χ

B.1.1 $\Delta\chi$

The change in χ over the crystal thickness is also a result of the deformation of crystal as shown in Figure B.1. Assuming in the first unit cell (the left dark blue shaded box), $\tan\chi_0 = h_0/t_0$, then in the last unit cell (the right blue box),

$$h = h_0(1 - \tau_+/R), \tag{B.2}$$

$$t = t_0(1 + \nu\tau_+/R). \tag{B.3}$$

Therefore,

$$\tan(\chi_0 + \Delta\chi) = \frac{h}{t} = \frac{1 - \tau_+/R}{1 + \nu\tau_+/R}\frac{h_0}{t_0} = \frac{1 - \tau_+/R}{1 + \nu\tau_+/R}\tan\chi_0. \tag{B.4}$$

Then

$$\frac{\tan\chi_0 + \tan\Delta\chi}{1 - \tan\chi_0\tan\Delta\chi} = \frac{1 - \tau_+/R}{1 + \nu\tau_+/R}\tan\chi_0. \tag{B.5}$$

Solving the equation using the small angle approximation for $\Delta\chi$, we get

$$\Delta\chi_+ = \tan\Delta\chi = \frac{-(1+\nu)\tau_+ \tan\chi_0}{(R+\nu\tau_+) + (R-\tau_+)\tan^2\chi_0}. \tag{B.6}$$

It can be generalized to the expansion side of the neutral plane as

$$\Delta\chi_- = \tan\Delta\chi = \frac{(1+\nu)\tau_- \tan\chi_0}{(R-\nu\tau_-) + (R+\tau_-)\tan^2\chi_0}. \tag{B.7}$$

The total change of χ across the bent crystal is then

$$\begin{aligned}\Delta\chi &= \Delta\chi_+ - \Delta\chi_- \\ &\approx -\frac{\tau_+ + \tau_-}{2R}(1+\nu)\sin 2\chi_0 \\ &= -\frac{T(1+\nu)}{2R}\sin 2\chi_0.\end{aligned} \tag{B.8}$$

B.1.2 $\Delta\phi$

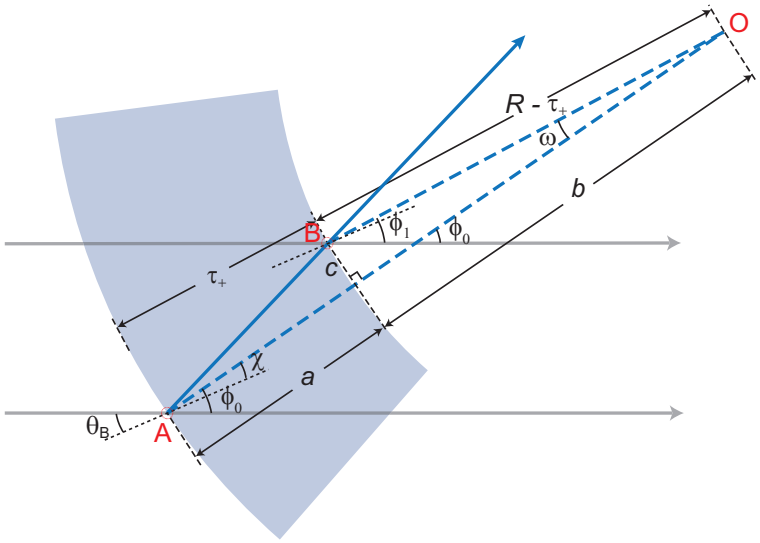

Figure B.2: Schematic view to estimate the change in angle ϕ. Point A and B are the same as in Figure 5.3. The relevant dimensions and angles are discussed in the text.

ϕ is defined as the directional angle from the transmission x-ray to the crystal surface normal (positive for counter-clockwise) and the subscriptions $_0$ and $_1$ correspond to the point A and Bas shown in Figure B.2 which shows again the compressed half of the crystal. O is the center of the crystal bending circle. AO and BO are along the corresponding crystal surface normal directions, and AB is the path of the diffracted x-ray in the crystal.

$\Delta\phi$, the change of ϕ, is defined as $\phi_1 - \phi_0$. It is obvious that $\Delta\phi$ is equal to the negative of angle ω as shown in Figure B.2,

$$\omega = \phi_0 - \phi_1 = -\Delta\phi. \tag{B.9}$$

In the triangle ABO,

$$a + b = R, \tag{B.10}$$

where

$$a = \frac{c}{\tan\angle BAO} = \frac{c}{\tan(\theta_B - \chi)} = \frac{(R-\tau_+)\sin\omega}{\tan(\theta_B - \chi)}, \tag{B.11}$$

$$b = (R - \tau_+)\cos\omega. \tag{B.12}$$

Therefore,

$$\frac{(R - \tau_+)\sin\omega}{\tan(\theta_B - \chi)} + (R - \tau_+)\cos\omega = R. \tag{B.13}$$

Using the small angle approximation, we have

$$\frac{(R - \tau_+)\omega}{\tan(\theta_B - \chi)} + (R - \tau_+)(1 - \frac{\omega^2}{2}) = R. \tag{B.14}$$

Solving the equation above for ω, we get two solutions,

$$\omega_1 = \frac{1}{\tan(\theta_B - \chi)} - \sqrt{\frac{1}{[\tan(\theta_B - \chi)]^2} - \frac{2\tau_+}{R - \tau_+}}, \tag{B.15}$$

and

$$\omega_2 = \frac{1}{\tan(\theta_B - \chi)} + \sqrt{\frac{1}{[\tan(\theta_B - \chi)]^2} - \frac{2\tau_+}{R - \tau_+}}. \tag{B.16}$$

The first solution, ω_1, is the solution we need, while ω_2 exists mathematically but it is not practical for the optical application here. Thus, for the compression side of the crytal,

$$\Delta\phi_+ = \sqrt{\frac{1}{[\tan(\theta_B - \chi)]^2} - \frac{2\tau_+}{R - \tau_+}} - \frac{1}{\tan(\theta_B - \chi)}, \tag{B.17}$$

and for the expansion side of the crystal,

$$\Delta\phi_- = \sqrt{\frac{1}{[\tan(\theta_B - \chi)]^2} + \frac{2\tau_-}{R + \tau_-}} - \frac{1}{\tan(\theta_B - \chi)}. \tag{B.18}$$

The total change of ϕ across the entire bent crystal is then

$$\begin{aligned}
\Delta\phi &= \Delta\phi_+ - \Delta\phi_- \\
&= \sqrt{\frac{1}{[\tan(\theta_B - \chi)]^2} - \frac{2\tau_+}{R - \tau_+}} - \sqrt{\frac{1}{[\tan(\theta_B - \chi)]^2} - \frac{2\tau_-}{R - \tau_-}} \\
&\approx -\frac{\tau_+ + \tau_-}{R}\tan(\theta_B - \chi) \\
&= -\frac{T}{R}\tan(\theta_B - \chi).
\end{aligned} \tag{B.19}$$

Note that the derivation for $\Delta\phi$ is based on the assumption that the source distance is infinitely far. A subscript, $_\infty$, will be used for clarity

$$\Delta\phi_\infty = -\frac{T}{R}\tan(\theta_B - \chi), \tag{B.20}$$

where $_\infty$ stands for the infinite source distance scenario. The general solution for $\Delta\phi$ will be given in Appendix B.2.3.

B.2 Feature Angles in General Bent Laue Diffraction with Finite Source Distance

With a finite source distance, the relations of the feature angles in bent Laue diffraction is shown in Figure B.3. (θ_{B0} is equivalent to θ_B where applicable.)

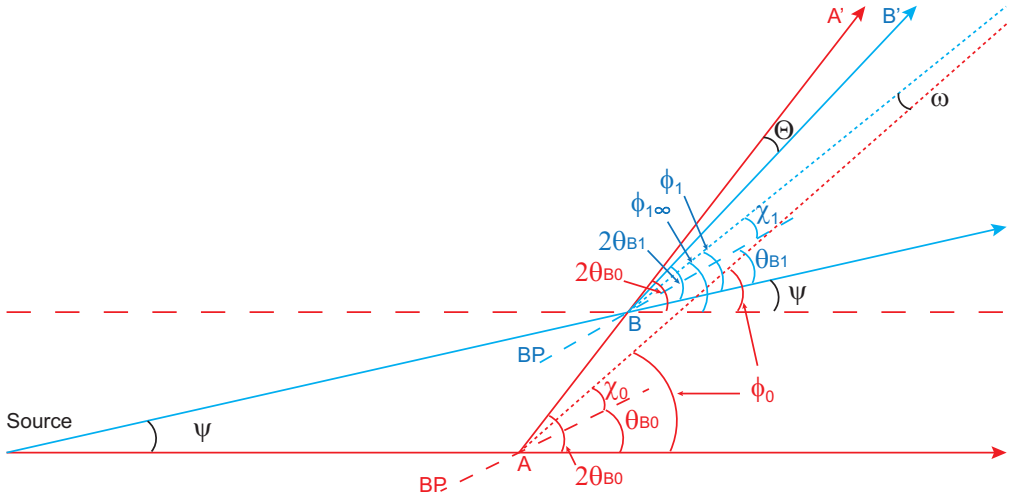

Figure B.3: Feature angles in general bent Laue diffraction with finite source distance. Point A is the location that the reference x-ray enters the crystal and get diffracted, and point B is where the diffracted reference x-ray ($\overrightarrow{AA'}$) exits the crystal. 'BP' stands for Bragg Plane.

B.2.1 ψ

From the geometry shown in Figure 5.4, we can easily get

$$\overline{AB}\cos(\theta_{B0}-\chi_0)=T, \tag{B.21}$$

$$\overline{AB}\sin 2\theta_{B0}=h, \tag{B.22}$$

which gives

$$h=\frac{T\sin 2\theta_{B0}}{\cos(\chi-\theta_{B0})}. \tag{B.23}$$

The x-rays incident angles divergence between point A and B is given by

$$\psi=\frac{h}{p}=\frac{T}{p}\frac{\sin 2\theta_{B0}}{\cos(\chi-\theta_{B0})}. \tag{B.24}$$

B.2.2 Θ

An important relationship between the x-rays diffracted from point A and B is that

$$2\theta_{B0}=\Theta+2\theta_{B1}+\psi, \tag{B.25}$$

or

$$\begin{aligned}\Theta&=2\theta_{B0}-2\theta_{B1}-\psi\\&=T\left[\frac{1+\nu}{R}\sin 2\chi-\frac{2}{R}\tan(\theta_B-\chi)-\frac{1}{p}\frac{\sin 2\theta_B}{\cos(\chi-\theta_B)}\right],\end{aligned} \tag{B.26}$$

which can be easily observed in Figure B.3.

Θ represents the angular distance between $\overrightarrow{AA'}$ and $\overrightarrow{BB'}$. When the magic condition is met, $\overrightarrow{AA'}$ and $\overrightarrow{BB'}$ overlaps and $\Theta=0$, which indicates that the magic condition with finite source distance is given by

$$2\theta_{B0}-2\theta_{B1}-\psi=0, \tag{B.27}$$

or

$$\Delta\phi-\Delta\chi=-\frac{1}{2}\psi. \tag{B.28}$$

B.2.3 $\Delta\phi$

As shown in Figure B.3,

$$\phi_1 = \phi_{1\infty} - \psi. \tag{B.29}$$

Therefore, the change of ϕ angle for finite source distance is given by

$$\begin{aligned} \Delta\phi &= \Delta\phi_\infty - \psi \\ &= -\frac{T}{R}\tan(\theta_B - \chi) - \frac{T}{p}\frac{\sin 2\theta_B}{\cos(\chi - \theta_B)}. \end{aligned} \tag{B.30}$$

Combine with Equation (B.28), the magic condition with finite source distance can be described with

$$\Delta\phi_\infty - \Delta\chi - \frac{\psi}{2} = 0, \tag{B.31}$$

or

$$\frac{1+\nu}{2}\frac{T}{R}\sin 2\chi - \frac{T}{R}\tan(\theta_B - \chi) - \frac{1}{2}\frac{T}{p}\frac{\sin 2\theta_B}{\cos(\chi - \theta_B)} = 0. \tag{B.32}$$

B.2.4 $\Delta\theta_{B_{01}}$

The difference between the Bragg angles at point A and B for general bent Laue diffraction is

$$\begin{aligned} \Delta\theta_{B_{01}} &= \theta_{B1} - \theta_{B0} \\ &= \Delta\phi - \Delta\chi \\ &= \frac{1+\nu}{2}\frac{T}{R}\sin 2\chi - \frac{T}{R}\tan(\theta_B - \chi) - \frac{T}{p}\frac{\sin 2\theta_B}{\cos(\chi - \theta_B)}. \end{aligned} \tag{B.33}$$

When the magic condition is met,

$$\Delta\theta_{B_{01}} = -\frac{\psi}{2} = -\frac{1}{2}\frac{T}{p}\frac{\sin 2\theta_B}{\cos(\chi - \theta_B)}. \tag{B.34}$$

B.3 Integration of Energy Resolution Contributions from $\frac{\Delta E}{E}_1$ and $\frac{\Delta E}{E}_2$

While the contribution from Darwin width, source size or detector spatial resolution is independent from other contributions, the d-spacing and source distance originated contributions can either supplement or counteract each other and their values should be dealt with signs. The integration of these two contributions in different scenarios are explained below.

- With a finite source distance and ignoring the lattice spacing variation in the crystal, the Bragg angle at point B is smaller than that at point A ($\theta_{B1} < \theta_{B0}$) and the energy of the Bragg diffracted x-rays at point B is higher than that at point A ($E_1 > E_0$) because of the Bragg's law.

  When the lattice spacing variation is considered, in a focusing (defocusing) geometry, it supplements (counteracts) the energy deviation caused by the source distance, because the lattice spacing is compressed (expanded) on the downstream side of the crystal, which corresponds to higher (lower) energy of the Bragg diffracted x-rays.

- With a beyond-infinite source distance (virtual source or converging incident beam or negative source distance), the Btagg angle at point B is larger than that at point A ($\theta_{B1} > \theta_{B0}$)and the energy of the Bragg diffracted x-rays at point B is lower than that at point A ($E_1 < E_0$) because of the Bragg's law.

  When the lattice spacing variation is considered, in a focusing (defocusing) geometry, it counteracts (supplements) the energy deviation caused by the source distance, because the lattice spacing is compressed (expanded) on the downstream side of the crystal, which corresponds to higher (lower) energy of the Bragg diffracted x-rays.

B.4 Focal Size Calculation with Two Types of Foci

The focal size of a bent Laue crystal for a point source can be calculated using the geometry of single-ray focus and geometric focus. As shown in Figure B.4, the focal size is given by

$$S_f = \frac{q_S - q_G}{q_S} L_f, \tag{B.35}$$

where L_f is the length of the crystal illuminated by a single-ray focused fan beam and is given by

$$\begin{aligned} L_f &= T_{\text{hor}} \sin 2\theta \\ &= \frac{\sin 2\theta_B}{\cos(\chi + \theta_B)} T. \end{aligned} \tag{B.36}$$

q_S and q_G are the single-ray focal distance and the geometric focus and are given by Equations (5.13) and (5.12), respectively.

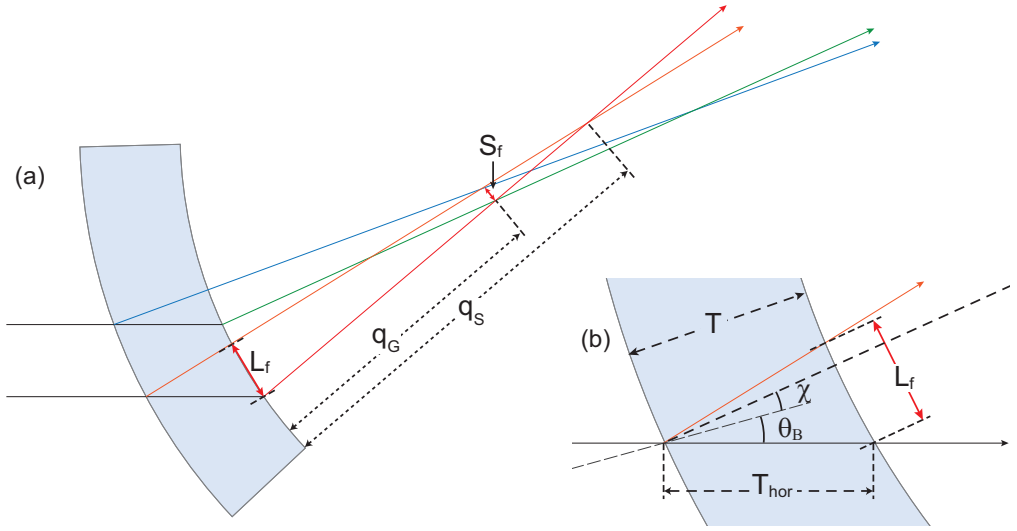

Figure B.4: Focal size in relation to the single-ray focus and the geometric focus geometry

B.5 Directional Energy Spread in the Quasi-Monochromatic Beam

The energy spreads caused by the lattice spacing variation and the source distance are directional. The combination of the latter two makes the energy of the quasi-mono beam lower on one side and higher on the other side.

B.5.1 $\Delta\theta_{Q1}$

The angular spread between $\overrightarrow{AA'}$ and $\overrightarrow{CC''}$ (Figure 5.6) caused by lattice spacing variation between point A and C can be calculated with

$$\Delta\theta_{Q1} = \frac{\Delta d}{d} \tan\theta_B = -\frac{T}{R}(\cos^2\chi_0 - \nu \sin^2\chi_0) \tan\theta_B. \tag{B.37}$$

B.5.2 $\Delta\theta_{Q2}$

The influence of source distance being finite can be calculated through the pitch angle ψ_{AC}, which is the x-ray incident angle divergence between point A and C shown in Figure 5.8 and is given by

$$\psi_{AC} = \psi_{AB} - \psi_{BC},$$

where ψ_{AB} is given by Equation (B.24), and ψ_{BC} is the angle from EB to EC, which is given by

$$\begin{aligned}\psi_{BC} &= \frac{L}{p}\cos(\chi_2+\theta_{B2}) \\ &\approx \frac{L}{p}\cos(\chi_0+\theta_{B0}).\end{aligned} \tag{B.38}$$

Because the x-rays diffracted at point A and C travel on the same direction, the divergence of the Bragg angle is half of the angle divergence between the incident x-rays. Thus, the Bragg angle divergence in the quasi-mono beam caused by finite source distance is given by

$$\begin{aligned}\Delta\theta_{Q2} &= -\frac{1}{2}\psi_{AC} \\ &= -\frac{1}{2}\left[\frac{T\sin 2\theta_{B0}}{p\cos(\chi_0-\theta_{B0})} - \frac{L\cos(\chi_2+\theta_{B2})}{p}\right] \\ &\approx -\frac{1}{2}\left[\frac{T\sin 2\theta_{B0}}{p\cos(\chi_0-\theta_{B0})} - \frac{L\cos(\chi_0+\theta_{B0})}{p}\right].\end{aligned} \tag{B.39}$$

B.6 Calculation for the Optimal Detector Distance

In Figure 5.8, The angular energy dispersion in the area, $\overline{A'C'}$, illuminated by a quasi-mono beam on the detector consists two contributions. The first contribution, $\Delta\theta_Q$, is the energy spread of the quasi-mono beam, and it is a constant value during the propagation of the diffracted beam. It can be also viewed as the diffraction angle variation from point A to C. The second contribution, $\Delta\theta_G$, is the energy spread brought by the Surface Diffracted X-rays that arrive at the detector in the quasi-mono beam area. It can be also viewed as the diffraction angle variation from point A to D. The relation between point C and D is that the diffracted x-rays from these two points arrive at the same location, C', on the detector.

Now it is obvious that, when the two contributions equal to each other, x-rays arrive at point C' have the same energy. This condition can be simply described by

$$\Delta\theta_Q = \Delta\theta_G, \tag{B.40}$$

where $\Delta\theta_Q$ is known from Equations (5.33), and $\Delta\theta_G$ consists of the following two parts.

The first part, $\delta\theta_{G1}$, is from the rotation of the Bragg planes caused by the bending of the crystal, which is given by

$$\delta\theta_{G1} = -\frac{W}{d}\frac{q_G}{\cos(\chi_0-\theta_{B0})}\frac{1}{R}, \tag{B.41}$$

where d is the distance from the geometric focal to the detector and hereinafter.

The second part, $\delta\theta_{G2}$, is from the incident angle divergence caused by the finite source distance, which is given by

$$\delta\theta_{G2} = -\frac{W}{d}\frac{q_G}{\cos(\chi_0-\theta_{B0})}\frac{\cos(\chi_0+\theta_{B0})}{p}. \tag{B.42}$$

Thus, $\Delta\theta_G$ is given by the combination of the two parts,

$$\Delta\theta_G = \delta\theta_{G1} + \delta\theta_{G2} \tag{B.43}$$

$$= -\frac{W\cdot q_G}{d\cdot\cos(\chi_0-\theta_{B0})}\left[\frac{1}{R} + \frac{\cos(\chi_0+\theta_{B0})}{p}\right] \tag{B.44}$$

$$= -\frac{q_G}{d}\left[\frac{L}{R} + \frac{L\cos(\chi+\theta_B)}{p}\right]. \tag{B.45}$$

Therefore, the focus-to-detector distance, d, that fulfils Equation (B.40) can then be solved by using Equations (5.33), (B.40) and (B.45) as

$$d = -\frac{W\cdot q_G}{\Delta\theta_Q\cdot\cos(\chi_0-\theta_{B0})}\left[\frac{1}{R} + \frac{\cos(\chi_0+\theta_{B0})}{p}\right], \tag{B.46}$$

or

$$d = -\frac{q_G}{\Delta\theta_Q}\left[\frac{L}{R} + \frac{L\cos(\chi_0 + \theta_{B0})}{p}\right]. \tag{B.47}$$

Equation (B.45) also implies that $\Delta\theta_G$ can be calculated from the length of the footprint of the quasi-mono beam on the crystal. The terms in the square bracket are the radians of the footprint relative to the crystal bending radius and the source distance. Let

$$\Delta\theta_L = \frac{L}{R} + \frac{L\cos(\chi_0 + \theta_{B0})}{p}, \tag{B.48}$$

then

$$\frac{\Delta\theta_G}{\Delta\theta_L} = -\frac{q_G}{d}. \tag{B.49}$$

B.7 Precise Calculations for Feature Angles at Feature Locations on the Crystal

B.7.1 χ_1 and χ_2

χ_1 and χ_2 are the asymmetry angles of the Bragg planes at point B and C, respectively. The change of asymmetry angle is caused only by the bending deformation of the crystal, thus for the locations at the same depth of the crystal, the asymmetry angles are the same. The change of χ over the crystal is given by Equation (5.3). χ_1 and χ_2 is then given by

$$\chi_2 \equiv \chi_1 = \chi_0 + \Delta\chi. \tag{B.50}$$

B.7.2 θ_{B1}

As shown in Figure 5.8, θ_{B1} is the Bragg diffraction angle at point B where the reference diffraction ray, $\overrightarrow{AA'}$, exits the crystal. From Equations (5.2), (5.3) and (5.4), θ_{B1} can be calculated with

$$\begin{aligned}\theta_{B1} &= \theta_{B0} + \Delta\phi_\infty - \Delta\chi - \psi \\ &= \theta_{B0} + \frac{1+\nu}{2}\frac{T}{R}\sin 2\chi_0 - \frac{T}{R}\tan(\theta_{B0} - \chi_0) - \frac{T\sin 2\theta_{B0}}{p\cos(\chi_0 - \theta_{B0})}.\end{aligned} \tag{B.51}$$

The ψ angle here is a necessary correction because Equation (5.2) is derived for the infinite source distance geometry.

B.7.3 θ_{B2}

θ_{B2} is the Bragg diffraction angle at point C where the edge ray of the quasi-mono beam is diffracted on the downstream surface of the crystal. The diffraction angle deviation from point B to C can be described by the quasi-mono beam footprint on the downstream side of the crystal, i.e., the rotation of the Bragg planes between point B and C and the rotation of the incident rays at point B and C relative to the source, as shown in the equation below

$$\theta_{B2} = \theta_{B1} + \frac{L}{R} + \frac{L\cos(\chi_2 + \theta_{B0})}{p}. \tag{B.52}$$

Using Equations. (5.3), (5.12), (5.24), (5.27), (B.50), (B.51) and (B.52), θ_{B2} can be solved numerically.

B.8 Summary of Variables in Chapter 5

Variables are defined when it is used the first time in the text, and all variable definitions are summarized in this appendix section for convenience.

B.8.1 Source distance, p

p is positive when there is a real source or the incident beam to the crystal is diverging.

B.8.2 Crystal bending radius, R

R is positive when the x-ray beam incidents on the convex side of the crystal. The surface curvature of a crystal bent with a positive R focuses the incident beam.

B.8.3 Crystal thickness, T_0 and T

T_0 is the thickness of a crystal in absence of bending. T is the thickness of the bent crystal. T_0 and T can be positive or negative. When they are negative, T_0 and T are directing to the upstream side of the reference surface.

B.8.4 Bragg angle, θ_B

The center incident ray Bragg angle on the crystal reference surface. It is directed from x-ray incident direction to the diffraction plane.

When the direction is counter clockwise, θ_B is positive and the x-ray is up bounced; when the direction is clockwise, θ_B is negative and the x-ray is down bounced.

B.8.5 Asymmetry angle, χ

The directed angle from the diffraction plane to the crystal surface normal. When the direction is counter clockwise, χ is positive; when the direction is clockwise, χ is negative.

χ influences the consistency of the focusing properties of the diffraction planes and the crystal surface geometry. As an example, in the case of an up bounce ($\theta > 0$) and focusing crystal geometry ($R > 0$), positive χ angle corresponds to diffraction plane focusing and negative χ angle corresponds to diffraction plane defocusing. The influences of all R, θ_B and χ is listed in the table below (Positive sign for the diffraction planes represents real focus and vice versa). An intuitive way to understand this is that the sign of the product of the three variables corresponds to focusing or defocusing by the diffraction planes.

Table B.1: Real focus or virtual focus.

R	θ_B	χ	Real focus (+) or virtual focus (−) by Bragg planes
+	+	+	+
+	+	−	−
+	−	+	−
+	−	−	+
−	+	+	−
−	+	−	+
−	−	+	+
−	−	−	−

B.8.6 Poisson ratio, ν

The Poisson ratio is considered as homogeneous with given crystal material and diffraction indices.

B.8.7 $\Delta\chi$

$$\Delta\chi = \chi_1 - \chi_0$$

where χ_1 is the asymmetry angle of the diffraction planes at point B and equal the asymmetry angle at any point on the same crystal surface; χ_0 is the asymmetry angle of the diffraction planes at point A and equals the asymmetry angle at any point on the same crystal surface.

B.8.8 $\Delta\phi$ and $\Delta\phi_\infty$

$$\Delta\phi = \phi_1 - \phi_0$$

where ϕ stands for the directed angle from the crystal surface normal to the diffracted x-ray, and the subscriptions $_1$ and $_0$ correspond to point B and A. The angle ϕ is equivalent to $\theta_B - \chi$, and is used for the convenience of concept illustration.

$\Delta\phi_\infty$ is the $\Delta\phi$ given the source distance is infinite. The relationship between the general $\Delta\phi$ and $\Delta\phi_\infty$ is given by

$$\Delta\phi = \Delta\phi_\infty - \psi,$$

where ψ is the opening angle between x-rays incident at point A and B (Figure B.3).

B.8.9 Quasi-Monochromatic Beam Width (QMBW), W

The width of diffracted beam parallel to the diffracted reference x-ray. The sign of the width value corresponds to the relative direction of the quasi-mono beam to the diffracted reference x-ray.

B.8.10 Quasi-monochromatic beam footprint length, L

Quasi-monochromatic beam footprint arc length on the downstream surface of the crystal.